

Louisiana Tech University

Louisiana Tech Digital Commons

Doctoral Dissertations

Graduate School

Fall 2019

Electrolytic Metallization of Halloysite Nanotubes and Antimicrobial Applications

Ahmed Humayun

Louisiana Tech University

Follow this and additional works at: <https://digitalcommons.latech.edu/dissertations>



Part of the [Biomedical Engineering and Bioengineering Commons](#)

Recommended Citation

Humayun, Ahmed, "" (2019). *Dissertation*. 825.

<https://digitalcommons.latech.edu/dissertations/825>

This Dissertation is brought to you for free and open access by the Graduate School at Louisiana Tech Digital Commons. It has been accepted for inclusion in Doctoral Dissertations by an authorized administrator of Louisiana Tech Digital Commons. For more information, please contact digitalcommons@latech.edu.

**ELECTROLYTIC METALLIZATION OF HALLOYSITE
NANOTUBES AND ANTIMICROBIAL APPLICATIONS**

by

Ahmed Humayun, B.Tech., M.S.

A Dissertation Presented in Partial Fulfillment
of the Requirements of the Degree
Doctor of Philosophy

COLLEGE OF ENGINEERING AND SCIENCE
LOUISIANA TECH UNIVERSITY

November 2019

LOUISIANA TECH UNIVERSITY
THE GRADUATE SCHOOL

SEPTEMBER 17, 2019

Date

We hereby recommend that the dissertation prepared under our supervision by
Ahmed Humayun, B.Tech., M.S.

entitled **Electrolytic Metallization of Halloysite Nanotubes and Antimicrobial Applications**

be accepted in partial fulfillment of the requirements for the Degree of
Doctor of Philosophy in Molecular Sciences and Nanotechnology

Supervisor of Dissertation Research

Head of Department

Department

Recommendation concurred in:

Advisory Committee

Approved:

Director of Graduate Studies

Dean of the College

Approved:

Dean of the Graduate School

ABSTRACT

Due to increased reports of infections and biofouling arising from the use of invasive medical devices, novel antimicrobial agents with suitable anti-biofouling properties are critically needed. Transition metals exhibit substantial antimicrobial activity; however, their use is limited because of their inherent toxicity to eukaryotic cells. In this regard, naturally occurring halloysite clay nanotubes (HNTs) show significant promise. HNTs possess a high surface area for adsorption while its hollow lumen can be used for loading different materials.

Herein, we demonstrate an electrolytic method for generating and depositing metal nanoparticles (NPs) on the HNTs outer surface and we propose an optimized method for fabricating metal-halloysite clay nanotubes (mHNTs) with varying silver (Ag), copper (Cu), and zinc (Zn) deposition displaying contrasting microbiological and cytotoxic properties which were validated using various characterization methods.

Bacterial biofouling of medical devices through biofilm formation is a significant problem leading to failure, to address this problem mHNTs were incorporated into 3D printing, spray coating of antibacterial chitosan film, electrodeposition of titanium implants.

APPROVAL FOR SCHOLARLY DISSEMINATION

The author grants to the Prescott Memorial Library of Louisiana Tech University the right to reproduce, by appropriate methods, upon request, any or all portions of this Dissertation. It is understood that “proper request” consists of the agreement, on the part of the requesting party, that said reproduction is for his personal use and that subsequent reproduction will not occur without the written approval of the author of this Dissertation. Further, any portions of the Dissertation used in books, papers, and other works must be appropriately referenced to this Dissertation.

Finally, the author of this Dissertation reserves the right to publish freely, in the literature, at any time, any or all portions of this Dissertation.

Author _____

Date _____

DEDICATION

Dedicated to my family.

TABLE OF CONTENTS

ABSTRACT.....	iii
APPROVAL FOR SCHOLARLY DISSEMINATION	iv
DEDICATION	v
LIST OF FIGURES	x
ACKNOWLEDGMENTS	xvi
CHAPTER 1 INTRODUCTION	1
1.1 Goal.....	1
1.2 Rationale	2
1.3 Objectives	3
1.3.1 Optimization of an Electrolytic Method for Metallizing HNTs	4
1.3.2 Effect of Quantity of Metal Deposit on HNTs External Surface on its Antimicrobial Properties and Cytotoxicity	5
1.3.3 Electrodeposition of Gentamicin Loaded mHNTs/Chitosan on Titanium Implants.....	5
1.3.4 Surface Functionalization of 3D Printed Polylactic Acid Constructs.....	5
1.3.5 Gentamicin Loaded ZnHNTs-Chitosan Antimicrobial Coating for Medical Devices.....	6
1.3.6 Electrolytic Synthesis of Double Metal-Coated mHNTs.....	6
1.4 Organization of the Dissertation	7
CHAPTER 2 BACKGROUND	8
2.1 Halloysite Nanotubes	8
2.2 Antimicrobial Metals and Metal Halloysite Nanotubes	9

2.3	Methods for Metallizing Halloysite Nanotubes.....	10
2.4	Biofouling and Biofilms	11
2.5	Titanium Implants.....	13
2.6	Antimicrobial Polymer Coatings	14
2.7	Three-Dimensional Printing	15
CHAPTER 3 METHODS		16
3.1	Experimental Design and Objectives.....	16
3.2	Materials and Methods.....	16
3.2.1	Cell Culture.....	17
3.2.2	Live/Dead Cytotoxicity Assay	18
3.2.3	Bacterial Cultures and Testing.....	19
3.2.4	Statistical Analysis.....	20
3.3	Instrumentation	20
CHAPTER 4 ELECTROLYTIC METALLIZATION OF HALLOYSITES		22
4.1	Introduction.....	22
4.2	Materials and Methods.....	23
4.2.1	Materials	23
4.2.2	Methods.....	23
4.2.3	Characterization	25
4.3	Results and Discussion	25
4.4	Conclusion	35
CHAPTER 5 DIFFERENTIAL ANTIMICROBIAL AND CELLULAR RESPONSE OF ELECTROLYTICALLY SYNTHESIZED HALLOYSITES HAVING DIFFERENT AMOUNTS OF SURFACE METALLIZATION.....		36
5.1	Introduction.....	36
5.2	Materials and Methods.....	38

5.2.1	Materials	38
5.2.2	Methods.....	38
5.2.3	Characterization	40
5.3	Results and Discussion	40
5.4	Conclusion	51
CHAPTER 6 ELECTROPHORETIC DEPOSITION OF GENTAMICIN LOADED ZNHNTS-CHITOSAN ON TITANIUM.....		52
6.1	Introduction.....	52
6.2	Materials and Methods.....	53
6.2.1	Materials	53
6.2.2	Methods.....	54
6.2.3	Characterization	57
6.3	Results and Discussion	57
6.4	Conclusion	68
CHAPTER 7 GENTAMICIN LOADED ZNHNTS-CHITOSAN ANTIMICROBIAL COATINGS FOR MEDICAL DEVICES		69
7.1	Introduction.....	69
7.2	Materials and Methods.....	71
7.2.1	Materials	71
7.2.2	Methods.....	71
7.2.3	Characterization	72
7.3	Results and Discussion	73
7.4	Conclusion	79
CHAPTER 8 3D PRINTED PLA CONSTRUCTS FUNCTIONALIZED WITH CHITOSAN OLIGOSACCHARIDE LACTATE- ZNHNTS-AG HAVING ANTIMICROBIAL ACTIVITY.....		80
8.1	Introduction.....	80

8.2	Materials and Methods.....	82
8.2.1	Materials	82
8.2.2	Experimental	82
8.2.3	Characterization	83
8.3	Results and Discussion	84
8.4	Conclusion	89
CHAPTER 9 TWO-STAGE ELECTROLYTIC SYNTHESIS OF DOUBLE METAL COATED MHNTS		91
9.1	Introduction.....	91
9.2	Materials and Methods.....	92
9.2.1	Materials	92
9.2.2	Methods.....	92
9.2.3	Characterization	93
9.3	Results and Discussion	93
9.4	Conclusion	99
CHAPTER 10 CONCLUSIONS AND FUTURE WORK.....		100
10.1	Conclusions.....	100
10.2	Future Work.....	101
APPENDIX A IMAGEJ ANALYSIS OF LIVE/DEAD ASSAYS		102
Bibliography		103

LIST OF FIGURES

- Figure 1-1:** Graphical overview of the projects - metal HNTs and their incorporation into a few biomedical applications was the central theme..... 1
- Figure 4-1:** Electrolytic setup for halloysite metallization consisting of two platinum-coated mesh electrodes held 2-inch apart in aqueous 2.5 mM AgNO₃ and 50 mg HNTs at 80° C magnetically stirred suspension. Under applied electric field the three processes occur (a) cathodic migration of silver cations (b) cathodic reduction and release of neutral silver nanoparticles in the solution (c) adsorption of silver nanoparticles on the outer surface of HNTs. Polarity reversal helps in the release of reduced silver nanoparticles into the solution, magnetic stirring helps in uniform distribution and mixing with dispersed halloysites..... 24
- Figure 4-2:** UV-Vis spectra of AgHNTs showing the highest intensity of absorption at 400 nm for AgHNTs 20V 20 min indicating a significant quantity of reduced Ag NPs in the solution, absorbance diminished with decreasing voltage and time, while application of constant polarity and heat alone led to lowest absorbances. (Inset – AgHNT 0, 5, 10, and 20 V respectively). 26
- Figure 4-3:** mHNTs produced at 5, 10, 20 V respectively, increasing applied voltage led to darker colored mHNTs, which can be attributed to the quantity of metal oxide adsorbed on HNTs. 26
- Figure 4-4:** SEM, EDS-map, and EDS quantification of (a, b, c) HNTs and (d, e, f) AgHNTs. The deposition of Ag NPs in the form of granules is clearly visible on the HNTs surface and verified using EDS-map..... 27
- Figure 4-5:** XRD pattern of AgHNTs at 5, 10, and 20V, respectively. AgHNTs 20, 10, and 5 V displaying sharp silver peaks (denoted by ▲, 111) and diminishing HNTs peaks (denoted by *, 001, 110, 002) showing HNTs reflections that became weaker with an increasing extent of metallization. 28
- Figure 4-6:** FTIR pattern of as received HNTs displaying the characteristic FTIR pattern. The characteristic peaks around 3690, 3620, 1000, and 903 cm⁻¹ respectively corresponding to O-H stretching of the inner surface hydroxyl groups, O-H stretching of inner hydroxyl groups, Si-O stretching vibrations, and Al-OH vibrations respectively. 29

- Figure 4-7:** XRF spectra for 20V, 20 V(no polarity reversal), 20 V 10 min, 20 V 5 min, 10 V, and 5 V. 20 V in the aqueous medium along with polarity reversal every 5 min lead to the highest concentration of Ag NPs indicated by greater XRF intensity. (all experiments in aqueous media, with regular polarity reversal and 20 min duration unless indicated)..... 30
- Figure 4-8:** XRF spectra for 20 V 20 min in aqueous, isopropanol, methanol, and ethanol solvents with polarity reversal. Aqueous media having higher dielectric constant led to higher conductivity leading to increased electrolysis and a higher concentration of Ag NPs. 30
- Figure 4-9:** XRF analysis of Ag wt.% deposition on HNTs. Application of only heating or stirring or both in combination led to a small amount of metal deposition on HNTs, which increased with the application of voltage, time and polarity reversal, (all samples – 20 min in aqueous medium unless stated otherwise). Inset – calibration curve for XRF standards. 32
- Figure 4-10:** Current (mA) Vs. time (s) for AgHNTs electrolysis in different solvents. Compared to methanol and ethanol, water has the highest dielectric constant and exhibited the highest current as a function of the applied voltage. Application of constant polarity resulted in sharper current drop over time, which can be due to a buildup of reduced species on the cathode which was countered by reversing polarity. . 33
- Figure 4-11:** Schematic representation of the cathodic reduction of Ag in electrodeposition. 34
- Figure 5-1:** Graphical abstract- (a). HNTs chemical structure, morphology, and SEM-EDS graph, (b). Electrolytic process for metallizing HNTs at 5 and 20 V respectively and SEM-EDS graph. 39
- Figure 5-2:** The natural white color of the HNTs was altered to darker colors depending on the type of metal used and quantity adsorbed. 40
- Figure 5-3:** SEM of (a) HNTs, (b, c) AgHNTs 5 and 20V, (d, e) CuHNTs 5 and 20 V, and (f, g) Zn HNTs 5 and 20 V respectively. Metal content on HNTs outer surface increased with the applied voltage (5-20 V). 41
- Figure 5-4:** XRF quantitative analysis of Ag, Cu, and ZnHNTs, respectively. Adsorbed metal content in mHNTs increased with applied voltage (5 and 20 V). 42
- Figure 5-5:** XRD spectra of AgHNTs, CuHNTs, and ZnHNTs. Increased applied voltage led to higher metal adsorption, hence more intense corresponding metal peaks and attenuated HNTs characteristic peaks. (* represents HNTs peak, ▲ represents metallic peak)..... 43

Figure 5-6: FTIR pattern of as received HNTs displaying the characteristic FTIR pattern. The characteristic peaks around 3690, 3622, 1031, and 903 cm^{-1} respectively corresponding to O-H stretching of the inner surface hydroxyl groups, O-H stretching of inner hydroxyl groups, Si-O stretching vibrations and Al-OH vibrations were recorded.....	44
Figure 5-7: Current (mA) Vs. time (min) for mHNTs samples in aqueous electrolytic setup, the amount of current flow recorded as a function of the conductivity of the individual metal salts, solvents, and applied voltage.....	45
Figure 5-8: UV-Vis spectra of mHNTs (m=Ag, Zn, or Cu, respectively).....	46
Figure 5-9: Determination of MIC for mHNTs against <i>S. aureus</i> using resazurin assay. Purple well corresponds to dead, whereas partially purple/pink, and pink wells correspond to live bacteria, (n=4).	47
Figure 5-10: Disc diffusion assay of (a) HNTs, (b) AgHNTs, (c) CuHNTs, (d) ZnHNTs, (5 V -top, 20 V- bottom). HNTs exhibited no antimicrobial activity, for each set of metal coating the mHNTs antibacterial activity was found to be corresponding to the amount of metal deposit on HNTs.	47
Figure 5-11: Inhibition zones from the disc diffusion assay.	48
Figure 5-12: Live/Dead assay, preosteoblast cells were cultured in the presence of metal salts. Live cells (green), dead cells (red).....	48
Figure 5-13: Live/Dead assay, preosteoblast cells were cultured in the presence of mHNTs. Live cells (green) and dead cells (red).	49
Figure 5-14: Cell viability assay for mHNTs. AgNO_3 was found to be most toxic to cellular viability, and the toxicity reduced when adsorbed to HNTs. CuHNTs and ZnHNTs displayed slightly increased cellular viability with increased concentration adsorbed on HNTs.	50
Figure 5-15: Cell proliferation assay for mHNTs, a similar trend as cell viability was observed.	50
Figure 6-1: Graphical overview of the electrophoretic deposition process.	55
Figure 6-2: (a, c) Laser confocal image of CS-ZnHNTs-GS coating, (b) 3D topography of the implant.....	58
Figure 6-3: SEM micrograph of (a) Chitosan (b) CS-ZnHNTs-GS deposits, respectively. Smooth morphology of chitosan is disturbed on the addition of mHNTs which appear almost uniformly distributed on chitosan.....	58

- Figure 6-4:** EDS Mapping of (a, b) CS-HNTs and (c, d) CS-ZnHNTs, a more uniform surface with less titanium base metal visibility is obtained which could be due to increased conductance of the electrophoretic deposition on the addition of ZnHNTs. 59
- Figure 6-5:** FTIR spectra of the coatings. Arrow depicts the new peaks observed on the addition of ZnHNTs-GS at 1028 (in-plane Si-O stretching of HNTs), 1278 and 1401 cm^{-1} corresponding to C-N stretching of gentamicin respectively. 60
- Figure 6-6:** Current density during EPD at 40 V. The addition of ZnHNTs in the chitosan leads to increased current density, explainable based on increased conductivity due to ionic species leaching from ZnHNTs..... 61
- Figure 6-7:** Antimicrobial broth testing, GS-ZnHNTs-CS exhibited the highest bacteriostatic effect. (Inset shows agar diffusion assay of (a) Uncoated titanium, (b) CS, (c) CS-ZnHNTs, and (d) CS-ZnHNTs-GS. 61
- Figure 6-8:** Planktonic growth of *S. aureus* on the surface of the samples. 62
- Figure 6-9:** Biofilm assay using crystal violet, similar but diminished trend as compared to broth testing was obtained. Inset depicts the crystal violet stained biofilm in CS, CS-ZnHNTs, CS-ZnHNTs-GS wells (top-bottom respectively). 62
- Figure 6-10:** Crystal violet dye stained samples. Least biofilm formation was visually observed on CS-ZnHNTs-GS samples. 63
- Figure 6-11:** Zinc ion release from the CS-ZnHNTs-GS coatings, highest ion release concentration was observed at 24 hr, (n=5), (Inset – zinc ion standard XRF curve)..... 63
- Figure 6-12:** Gentamicin release from CS-ZnHNTs-GS coatings (ppm). A continuous burst of drug release was observed, which could be due to drug adsorbed on mHNTs outer surface and chitosan coating. (Inset – gentamicin standard XRF curve), (n=5). 64
- Figure 6-13:** Cell viability assay for electrodeposited Ti. 64
- Figure 6-14:** Live/Dead assay, preosteoblast cells were cultured in the presence of Ti implants (1a, 1b) CS, (2a, 2b) HNTs-CS, (3a, 3b) ZnHNTs-CS, and (4a, 4b) GS-ZnHNTs-CS. Live cells (green) and dead cells (red). 65
- Figure 6-15:** Proliferation assay for the Ti implants, CS-ZnHNTs-GS were found to be the most viable for cell proliferation. 66
- Figure 6-16:** SEM-EDS map of the samples soaked in SBF. 67
- Figure 7-1:** SEM, EDS map, and EDS of (a1, a2, a3) CS-1% ZnHNTs-GS, (b1, b2, b3) CS-2.5% ZnHNTs-GS, and (c1, c2, c3) CS-5% ZnHNTs-GS respectively..... 74
- Figure 7-2:** FTIR spectra of CS, CS-1, 2.5, and 5% ZnHNTs-GS films. 75

Figure 7-3: Average inhibition zones using the disk diffusion assay, increasing antibacterial activity was observed with a corresponding increase in ZnHNTs-GS wt.% in the coatings. Inset – a. CS, b. CS-1% ZnHNTs-GS, c. CS-2.5% ZnHNTs-GS, and d. CS-5% ZnHNTs-GS, respectively).....	76
Figure 7-4: Microtiter broth assay - effect of antimicrobial coatings on the absorbance of <i>S. aureus</i>	76
Figure 7-5: Crystal violet biofilm assay. Inset – biofilm formed on treatment with CS-1, 2.5, and 5% ZnHNTs-GS - top to bottom, respectively.	77
Figure 7-6: Gentamicin release from the coatings, an initial outburst of drug release is observed which could be due to the adsorbed drug on the ZnHNTs surface and in the chitosan coatings, (n=5).	78
Figure 7-7: Ion release from the coatings, an outburst of ion release is observed, which diminished over time, (p>0.05).	78
Figure 8-1: Schematic diagram for functionalization of 3D printed PLA scaffolds.	83
Figure 8-2: 3D printed a. PLA, functionalized with b. COS-ZnHNTs-5% Ag, c. COS-ZnHNTs-10% Ag, and d. COS-ZnHNTs-20% Ag.	84
Figure 8-3: Hydrolysis of the ester bond in the PLA backbone results in carboxyl and hydroxyl end groups (Tham <i>et al.</i> , 2014).	85
Figure 8-4: SEM-EDS map of COS-ZnHNTs-Ag in PLA at 5 (1a, 1b, 1c), 10 (2a, 2b, 2c), 20 (3a, 3b, 3c) wt.% respectively.....	85
Figure 8-5: EDS analysis of Ag content in the coatings, increasing Ag wt.% in functionalized PLA was observed with a corresponding increase in Ag content in the COS-ZnHNTs-Ag suspension, (n=5).	86
Figure 8-6: FTIR spectra of COS and COS-ZnHNTs-Ag.	87
Figure 8-7: Average inhibition diameter against <i>S. aureus</i> , a. COS-ZnHNTs-5% Ag (none), b. COS-ZnHNTs-10% Ag (0.76 mm±.004), and c. COS-ZnHNTs-20% Ag (0.80 mm±0.01).	88
Figure 8-8: Crystal violet biofilm assay, increasing Ag content in the coatings had an inhibitory effect on the <i>S. aureus</i> biofilm formation. Inset – a. control (b, c, d) COS-ZnHNTs- 5, 10, and 20% Ag respectively.....	89
Figure 9-1: SEM-EDS map of AgZnHNTs. Ag can be observed almost evenly distributed throughout the HNTs surface with interspersed patches of Zn.	94

Figure 9-2: XRF quantitative elemental analysis of AgZnHNTs showing the presence of silver and zinc on mHNTs. Inset XRF calibration curve for Ag and Zn, respectively, n=5.	95
Figure 9-3: FTIR pattern of as received HNTs displaying the characteristic FTIR pattern. The characteristic peaks around 3690, 3620, 1000, and 903 cm^{-1} respectively corresponding to O-H stretching of the inner surface hydroxyl groups, O-H stretching of inner hydroxyl groups, Si-O stretching vibrations, and Al-OH vibrations were recorded.	96
Figure 9-4: XRD of AgZnHNTs, HNTs, AgNO_3 , and ZnSO_4	97
Figure 9-5: Current flow in the first and second steps.	98
Figure A-1: JavaScript macro for automated cell counting.	102

ACKNOWLEDGMENTS

I express gratitude towards my research adviser Dr. David K. Mills, and I thank him for his encouragement, valuable guidance, and scientific freedom.

None of this would be possible without the love and support of my mother, father, and sisters. My father's advice never to accept defeat is my inspiration.

I want to thank the advisory committee Drs. Bryant Hollins, Collin Wick, Rebecca Giorno, and William Wolf for their time and consideration, I would also like to thank Dr. Sven Eklund, Mr. Davis Bailey, and Dr. William Clower.

I also want to thank Miss Yangyang Luo, Dr. Chris Boyer, Miss Anusha Elumalai, Mr. Antwine McFarland, and all my lab mates.

CHAPTER 1

INTRODUCTION

1.1 Goal

The objective of this study was twofold, first, optimization of the electrolytic metallization of the HNTs external surface, evaluation of the correlation between metallization extent and subsequent antimicrobial and cytotoxic response and second, integration of the metal-HNTs (mHNTs) into biomedical applications including electrodeposited titanium, antimicrobial coatings, and 3D printed constructs (**Figure 1-1**).

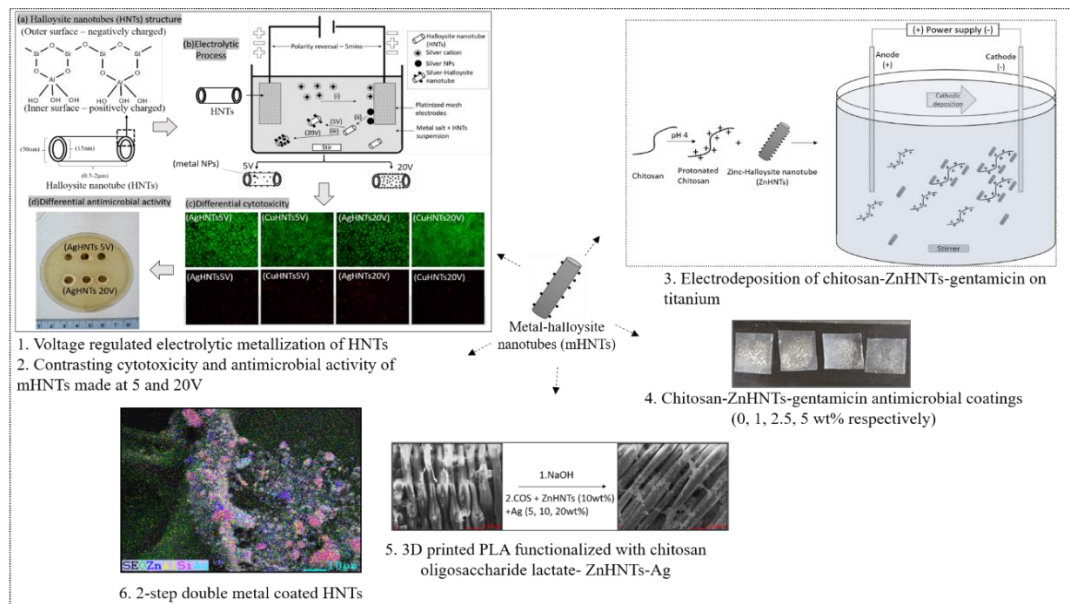


Figure 1-1: Graphical overview of the projects - metal HNTs and their incorporation into a few biomedical applications was the central theme.

Using different surface characterization methods, the presence of metal on the mHNTs surface was confirmed, and cell and microbiological assays were used to assess the cellular and antimicrobial potential of the mHNTs in different biomedical applications including electrophoretic deposition, air spray, and 3D printing.

1.2 Rationale

Nanotechnology is an active area of research worldwide and is finding increasing utility in industry, medicine, and consumer applications; however, the present applications are limited by toxicity, loss of efficacy due to agglomeration or short-lived action (Schummer and Baird, 2006; Ray, Yu and Fu, 2009). These issues can be potentially countered by providing a suitable micro/nanostructure that has the capability of not only functioning as an adsorbent surface to the nanoparticles but permit their sustained release over time (Lvov *et al.*, 2008). In this regard HNTs because of their unique cylindrical geometry with opposite surface and lumen charges have proven to be of significant interest; additionally, their cytocompatibility (Vergaro *et al.*, 2010), high surface area (Zhao and Liu, 2008), demonstrated integration with various polymers (Liu *et al.*, 2014), chemicals, drugs, biomolecules (Du, Guo, and Jia, 2010) make them an ideal choice as a nanoparticle support system. Potentially, the metallization of HNTs' external surface helps in functionalization with specific properties, e.g., catalytic, antimicrobial, magnetic, structural (M. Massaro *et al.*, 2017).

Metals and metal oxides have been used over the past several centuries as antimicrobial agents and with the advent of nanotechnology more advanced metal nanoparticle composites are gaining popularity and show promise as next-generation antimicrobial agents having an enhanced antimicrobial efficacy (Alexander, 2009). There

are several methods for depositing metal on HNTs including reduction with metal salts (Shu *et al.*, 2017), thermal degradation of metal acetates (Nicholson *et al.*, 2016), and covalent linkage (M. Massaro *et al.*, 2017), etc., however, as of now, no method has attempted to regulate the amount of metal deposited on HNTs or study the effects of differential quantitative metal deposition on HNTs outer surface and its subsequent effects on biomedical applications including antimicrobial and cytotoxic potential.

The proposed study attempts to produce a varying degree of metallization on the HNTs external surface, to characterize these coatings, and incorporate them into a few biomedical applications.

1.3 Objectives

The present study is aimed at several objectives with a unified goal of improving antimicrobial/anti-biofouling capabilities in different biomedical applications by integrating mHNTs. The following objectives were the core focus of the project:

Objective 1: Optimization of an electrolytic method for depositing metal nanoparticles on HNTs external surface.

Objective 2: Effect of the quantity of metal deposition on HNTs and its antimicrobial properties.

Objective 3: Electrodeposition of gentamicin loaded mHNTs/chitosan on titanium implants.

Objective 4: Surface functionalization of 3D-printed polylactic acid constructs with ZnHNTs-Ag-Chitosan oligosaccharide lactate.

Objective 5: Antimicrobial mHNTs-chitosan films.

Objective 6: Electrolytic synthesis of two metal-coated mHNTs.

These objectives will serve to advance the field of functionalized biomaterials and assess the potential of mHNTs as an antimicrobial agent in different biomedical applications.

1.3.1 Optimization of an Electrolytic Method for Metallizing HNTs

Various methods for depositing metal nanoparticles on HNTs exist, however, the electrolytic method demonstrated by Mills and Boyer et al. (Boyer, 2016; Mills and Boyer, 2018) is of significant interest because it uses no harmful chemicals, it is a single step and eco-friendly process. The first part of the study aims to optimize the electrolytic method for metallizing HNTs and attempt to regulate the degree of metallization by varying the applied voltage, solvent, and time duration.

In an electrolytic system by altering the applied voltage, the amount of current can be varied; thus, the ion flow can be modulated as well.

It was hypothesized that by controlling the applied voltage the number of charged ionic species can be controlled; thus the number of reduced species (cathode) could be modulated hence indirectly the population of reduced species (nanoparticles) in the electrolytic system can also be affected, hence, the external surface of the HNTs has differential amounts of reduced species in the vicinity for interaction.

The following hypothesis will be tested for different voltages, solvents, polarity alternation, and time duration.

1.3.2 Effect of Quantity of Metal Deposit on HNTs External Surface on its Antimicrobial Properties and Cytotoxicity

Numerous studies have focused on the deposition of metal on the HNTs external surface; however, it is crucial to correlate the observed effects with the quantity of metal adsorbed on the HNTs surface as well.

Studies indicate that the antimicrobial action of metals is quantity dependent; hence, it was hypothesized that mHNTs having higher metal content will exhibit increased antimicrobial action when compared to mHNTs having less metal. Likewise, similar results were hypothesized for the cytotoxicity assays.

1.3.3 Electrodeposition of Gentamicin Loaded mHNTs/Chitosan on Titanium Implants

This project aimed to incorporate mHNTs into chitosan for electrodeposition on titanium metal having potential utility in titanium implants. ZnHNTs will be loaded with an antibiotic (gentamicin) and added to chitosan, which will be subsequently electrodeposited on a titanium cathode using an ethanolic solvent. ZnHNTs ability to function as a controlled release drug container and thus prevent biofouling in conjunction with chitosan (acting as the coating vehicle) will be tested. It was hypothesized that ZnHNTs loaded with the antibiotic will lead to heightened antimicrobial effect and result in increased cell viability.

1.3.4 Surface Functionalization of 3D Printed Polylactic Acid Constructs

The objective was to 3D print constructs which are chemically modified the surface with sodium hydroxide (NaOH) and then functionalized with ZnHNTs-Ag-

chitosan oligosaccharide coating. Conventional methods of 3D printing and post-printing surface modification/functionalization will be utilized.

It is hypothesized that 3D printed constructs with varying concentrations of Ag (5, 10, and 20%) could lead to contrasting antimicrobial effects.

1.3.5 Gentamicin Loaded ZnHNTs-Chitosan Antimicrobial Coating for Medical Devices

Using commercial airbrush techniques gentamicin loaded ZnHNTs-chitosan will be sprayed to form antimicrobial films. It was hypothesized that by varying the amount of GS-ZnHNTs in chitosan (1, 5, and 10 wt.%), contrasting antimicrobial effects can be observed.

1.3.6 Electrolytic Synthesis of Double Metal-Coated mHNTs

Using a similar electrolytic technique as described above, a double metal-coated mHNTs was synthesized. It was hypothesized that at a reduced voltage mHNTs with lower metal content can be constructed which can be employed in subsequent electrolysis for coating a second metal.

Morphological analysis was conducted using a scanning electron microscope (SEM), confocal microscopy, chemical analysis by Fourier-transform infrared spectroscopy (FTIR), elemental analysis by Energy Dispersive X-ray spectroscopy (EDS) and X-ray fluorescence (XRF), crystallinity by X-ray diffraction (XRD), absorbance using ultraviolet-visible spectroscopy and current using laptop connected ammeter. Antibiotics loaded in HNTs using vacuum pump techniques, cytocompatibility using live/dead assay and proliferation kit, antimicrobial using Kirby–Bauer disc diffusion, microdilution method, resazurin dye, and crystal violet biofilm assay.

1.4 Organization of the Dissertation

The dissertation is comprised of 10 Chapters. Chapter 1 is a brief overview of the rationale and need for the research undertaken and the specific objectives. Chapter 2 provides a detailed literature review and the state of research in the metallization of HNTs. In addition, integration of mHNTs in the electrophoretic deposition in titanium implants, 3D printing, and antimicrobial coatings is also be discussed.

Chapter 3 is focused on detailed instrumentation and methods, Chapter 4 details on optimization of an electrolytic metallization procedure for HNTs, Chapter 5 studies mHNTs contrasting antibacterial and cytotoxic effects as a function of quantity of metallization, Chapter 6 studies electrodeposition of gentamicin loaded ZnHNTs-chitosan on titanium metal having enhanced biofouling activity, Chapter 7 describes a surface modification strategy for a 3D printed PLA constructs with chitosan-Ag-ZnHNTs, Chapter 8 describes the development of ZnHNTs/chitosan antimicrobial films, Chapter 9 expands on the method previously described, for electrolytic deposition of two metal coatings on HNTs and lastly Chapter 10 draws the conclusion and discusses future work.

CHAPTER 2

BACKGROUND

2.1 Halloysite Nanotubes

HNTs are an aluminosilicate clay composed of rolled aluminosilicate tubes that possess superior physical properties than either of its constituent oxides due to its tubular structure with contrasting charges on the lumen and the outer surface due to rolling defects. It possesses dimensions 15-50 nm diameter and 100-2000 nm length (Lvov *et al.*, 2008). Owing to their high surface area and charge HNTs have immense potential for adsorbing materials of opposing charges and hence can function as surface immobilization agents for various nanoparticles. These features have seen HNTs used in various applications including catalyst supports (Liu and Zhao, 2009), controlled release containers (Wei *et al.*, 2014), polymer reinforcement agents (Liu *et al.*, 2014), adsorbents (Zhao and Liu, 2008) and various biomedical applications including antimicrobial agents (Wei *et al.*, 2013), drug delivery systems (Grimes *et al.*, 2018), anti-biofouling surfaces (Boyer *et al.*, 2018), bone cement reinforcement (Wei *et al.*, 2012; Jammalamadaka, Tappa and Mills, 2018), 3D printing (Weisman *et al.*, 2015), etc. which are potentially enhanced by HNTs surface/lumen modification with polymers, metals, antibiotics and bioactive active agents. Extensive research shows the cytocompatibility of HNTs with a

variety of cell types including osteoblasts, stem cells, chondrocytes thus positioning them as ideal candidates for drug delivery, nanotechnology templates, and polymer additives.

2.2 Antimicrobial Metals and Metal Halloysite Nanotubes

Metals are crucial for the regulation of cellular processes; however, in excess, they can become harmful. Metal and metal oxides prevent bacterial growth by producing reactive oxygen species and inducing oxidative stress, membrane damage, enzyme disruption, or damage to genetic material (Lemire, Harrison and Turner, 2013).

Their antimicrobial properties have been known and utilized since ancient times, historically metal salts have been used against microbes, Greek and Roman civilization used silver vessels to preserve liquids, colloidal silver was used extensively in medical treatment (Alexander, 2009), copper-based medicines were used in treating eczema, lupus, anemia, chorea, syphilis (Grass, Rensing and Solioz, 2011), likewise zinc salts were used in wound treatment (Wani *et al.*, 2017).

Currently, antimicrobial metals are used in diverse fields ranging from biomedical applications to industry, and all this was made possible by the discovery that metals can disrupt antibiotic-resistant bacterial biofilms (Harrison *et al.*, 2004), have synergism with other classes of biocides (Harrison *et al.*, 2008), and have potential inhibitory effects on multidrug-resistant bacterial strains (Kaneko *et al.*, 2007; Lemire, Harrison and Turner, 2013).

The introduction of antibiotics in the early 20th century provided short-lived relief from almost all forms of bacterial infections, however with time bacteria have evolved, and cases of antibiotic-resistant strains are on the rise, as of now measures to overcome resistant strains remain a priority (Levy, 1998).

Metals nanoparticles exhibit magnified antimicrobial action; however, their use is limited due to inherent toxicity to the host, physical instability, aggregation, and dispersion leading to a gradual loss of antimicrobial potency (Hajipour *et al.*, 2012). A more synergistic approach combining the existing materials in relatively lower nontoxic concentrations might be the answer (Shu *et al.*, 2017), in this regard, HNTs can be of significant utility as their outer surface can be used for adsorption of metal nanoparticles, preventing their aggregation, reduce host toxicity and achieve a more sustained antimicrobial action even at minute concentrations (De Silva *et al.*, 2015). Recently, several studies have pointed out the improved antimicrobial action of metal nanoparticles when adsorbed on HNTs, recently it was found that an antimicrobial synergism between Ag and ZnO nanoparticles existed when adsorbed on HNTs, likewise, enhanced antimicrobial activity was reported for graphene supported AgHNTs (Yu *et al.*, 2014), AgHNTs in ultrafiltration polyethersulfone membranes (Zhang *et al.*, 2012), and antimicrobial coatings (Abdullayev *et al.*, 2011).

2.3 Methods for Metallizing Halloysite Nanotubes

Adsorbing metals nanoparticles is a comparatively straightforward method for metallizing HNTs, copper and cobalt nanoparticles were adsorbed on HNTs using wet impregnation method (Carrillo and Carriazo, 2015), iron oxide was deposited on HNTs for dye removal (Xie *et al.*, 2011), magnesium, lead, iron ions were removed from wastewater using surface adsorption (Hermawan *et al.*, 2018). Metal NPs were adsorbed using dry sintering of the metal acetates at high temperatures using a single pot method (Nicholson *et al.*, 2016), cobalt acetate was adsorbed using incipient wetness impregnation method and converted to cobalt oxide NPs by heating (Zhang and Yang,

2012), a study found HNTs to be most optimal sorption agents for silver ions and the adsorption was found to be affected by pH, concentration, temperature, contact time (Kiani, 2014), palladium NPs were deposited using methanolic reduction and nickel NPs were electroless plated using the surface as a template (Fu and Zhang, 2005), silver and zinc nanoparticles were reduced using sodium borohydride and a synergistic antimicrobial effect was observed (Shu *et al.*, 2017).

Alternatively, the outer surface of HNTs can also be covalently modified, and metal nanoparticles can be attached to the functional groups after modifications. Zinc oxide and titanium oxide nanoparticles with enhanced photocatalytic performance were attached using carbon modification (Zhang, Ouyang and Yang, 2014); silver, gold, palladium nanoparticles were attached using silanization (Yi Zhang *et al.*, 2013; Das and Jana, 2015; Jana *et al.*, 2017). Covalent modification techniques help to increase the degree of metallization; furthermore, it helps in retaining the deposited metal on the HNTs surface as the covalent bond is harder to disrupt as compared to adsorption with van der Waals forces.

2.4 Biofouling and Biofilms

A biofilm is a microbial community composed of one or more types of bacterial cell populations bound to a surface embedded in secreted extracellular matrix polysaccharides (Donlan, 2001), it is one of the significant causes of transplant failures and is caused by bacteria belonging to the *Staphylococcus* genus, specifically *S. aureus*, and *S. epidermis* bacteria (Tonetti and Schmid, 1994). Biofilm formation consist of distinctive steps comprising of (a) bacterial cell adhesion which can be affected by surface charge, hydrophobicity, topography and exposure time (Rochford, Richards and

Moriarty, 2012), (b) bacterial cell aggregation comprising of cellular proliferation and cell-cell adhesion leading to formation of extracellular matrix, (c) biofilm cell maturation where the individual bacteria assume a sessile form and achieve structural stability and lastly, (d) biofilm cell detachment where planktonic bacteria are released into the surrounding environment to invade and infect neighboring tissue (Høiby *et al.*, 2011). Biofilm leads to decreased antimicrobial susceptibility of the bacterial populations which could be explained due to hindered antibiotic diffusion through the extracellular matrix that can retard antibiotic diffusion due to reduced material transport arising due to charges or chemically reacting with the antibiotic chemical moieties (Hoyle, Wong and Costerton, 1992).

Over 65% of the total infections are estimated to be biofilm related (McLean, Lam and Graham, 2012) affecting over 12 million patients in America annually (O'toole, 2002). Metal implant material mainly titanium and stainless steel are susceptible to its formation. Biofilm formation on implants leading to infection and biofouling is one of the most significant causes of implant failure and loosening (2-5%) (Darouiche, 2004; Gbejuade, Lovering and Webb, 2015).

Different measures to counter biofilms have been developed including antibiotic releasing polymers coatings, silver bromide with size-tunable characteristics was used for long-lasting antibiofilm properties (Sambhy *et al.*, 2006), nitric oxide-releasing sol-gels (Nablo and Schoenfisch, 2003), ultrasonic controlled release of ciprofloxacin in poly (2-hydroxyethyl methacrylate) hydrogels (Norris *et al.*, 2005), salicylic acid-releasing polyurethane acrylate polymers catheter coatings (Nowatzki *et al.*, 2012), etc. metal NPs have demonstrated antibiofilm effects, including silver nanoparticle coatings on titanium

implants (Secinti *et al.*, 2011), zinc oxide, and hydroxyapatite nanoparticles in dental implants (Abdulkareem *et al.*, 2015), methicillin-resistant *S. aureus* biofilm has been shown to be susceptible to silver NPs on implants (van Hengel *et al.*, 2017), and a mixed metal-polymer composite consisting of silver, copper, and zinc have been shown to be significantly potent (Sowa-Söhle *et al.*, 2013). Tetracycline loaded HNTs has been shown to prevent biofouling of implants (Radda'a *et al.*, 2017). Similarly, gentamicin loaded HNTs polylactic acid films have shown similar activity (Pierchala *et al.*, 2018). Furthermore, vancomycin loaded HNTs on titanium implants have displayed similar potential (Farrokhi-Rad, Fateh and Shahrabi, 2018).

2.5 Titanium Implants

Commercially pure titanium (CP-Ti) and Ti-6Al-4V(Ti-64) are the most commonly used titanium alloys in medical implants. They possess high tensile strength, corrosion resistance, and biocompatibility (Holmberg *et al.*, 2013). Titanium metal develops a passive oxide layer when exposed to air leading to high resistance to corrosion, even in an aqueous medium it has a low tendency to form ions and thus low reactivity to biomolecules .

This property makes Ti the metal of choice for implants, especially when compared to stainless steel which can leach out nickel and chromium ions over time (Sidambe, 2014). Ti is employed for constructing dental and orthopedic implants, screws for fractures, bone plates, hip joints, and cornea backplates (Paschalis *et al.*, 2013). Almost all the dental implants are constructed from commercially pure Ti because of its higher resistance to corrosion (Adell *et al.*, 1981), and Ti-64 is the most widely used implant material in biomedical applications where strength is required (Elias *et al.*, 2008;

Holmberg *et al.*, 2013). Periprosthetic joint infection arising due to bacterial invasion is a severe complication arising in orthopedic surgery, it arises due to the growth of bacteria secreting extracellular polymeric substances which lead to biofilm formation having heightened antibiotic resistance and stable prokaryotic population leading to subsequent implant failure. Various antibacterial measures have been proposed to counter biofilm formation (Inoue *et al.*, 2019) including chitosan-hydroxy apatite coating deposited using dip method (Dikici *et al.*, 2016), titanium dioxide nanotubes grown by anodization and silver ions were deposited (Gunpath *et al.*, 2018), Ti-6Al-4V-copper alloy (Ren *et al.*, 2014), hydroxyapatite as an antibiotic release agent (Cox *et al.*, 2016), mussel inspired poly(dopamine) thin film having chitosan-silver (Wang, Xing and Ojo, 2014), tetracycline loaded HNTs chitosan layer (Radda'a *et al.*, 2017), and HNTs-vancomycin drug in chitosan (Farrokhi-Rad, Fateh and Shahrabi, 2018).

2.6 Antimicrobial Polymer Coatings

Post-operative infections arising due to biofouling of medical implants is a constant issue, and a considerable amount of research has been directed towards finding a solution. Bacteria attach to various surfaces and excrete extracellular matrix proteins and form a biofilm having a higher tolerance to antibiotics and chemicals leading to infection over time (Busscher *et al.*, 2012; Salwiczek *et al.*, 2014). Device related complications can lead to severe health as well as economic issues, it is estimated that infections cost upwards of between \$ 28-45 million each year, and 60% are device related (Scott, 2009). Several strategies exist for combating infections, including long-term usage of antibiotics and surgical revision; however, this comes at a high economic as well as health cost coupled with the risk of developing antibiotic resistance. Several research articles have

described the construction of antimicrobial films using polymer-metal composites, previous studies have constructed a chitosan-copper-aluminum coating that could be cold sprayed (Sanpo *et al.*, 2009), chitosan-silver, zinc antimicrobial films constructed using sol-gel technique (Li *et al.*, 2010), bioactive glass-chitosan-silver coatings for orthopedic devices using electrochemical deposition (Pishbin *et al.*, 2013), chitosan-silver oxide films made using solution casting method (Tripathi, Mehrotra and Dutta, 2011), and antimicrobial wound dressings from chitosan-silver-polyvinyl alcohol (Abdelgawad, Hudson and Rojas, 2014).

2.7 Three-Dimensional Printing

Three-dimensional printing (3D) printing is an emerging area of research with widespread applications in biomedical research. In the near future, 3D printing has a high potential to provide customized products and materials tailored to consumer specific needs. It involves layer by layer deposition of a polymer melt-extruded through a heated nozzle whose movement in different axis is based on coordinates coded into a sliced model file and controlled by software. 3D printing has been used to produce antibiotic eluting filaments (Weisman *et al.*, 2015), patient-specific prosthesis (Zuniga *et al.*, 2015), biliary stents (Boyer *et al.*, 2019), bioactive screws for localized drug delivery (Tappa *et al.*, 2019), etc., HNTs composites 3D printed for sustained drug release (Weisman *et al.*, 2017), 3D printed polymer for patterned human mesenchymal stem cells orientation (Wu *et al.*, 2019).

CHAPTER 3

METHODS

3.1 Experimental Design and Objectives

HNTs were metallized using electrolytic methods, and the resulting mHNTs were integrated into selected biomedical applications.

mHNTs and their biomedical incorporations were analyzed for surface morphology using scanning electron microscopy (SEM) and confocal microscopy, the elemental analysis was performed by energy-dispersive X-ray spectroscopy (EDS) which was supplemented with X-ray fluorescence (XRF) for more quantitative analysis, crystalline structure was determined using X-ray powder diffraction (XRD), and chemical composition by Fourier transform infrared spectroscopy (FTIR). Antibacterial activity against gram-positive was assessed using a microtiter broth absorbance assay, resazurin dye assay, biofilm crystal violet assay using microplate reader, and Kirby–Bauer disc diffusion method. Cytotoxicity was analyzed using a dual fluorochrome Live/Dead cytotoxicity assay kit.

The sections below provide more through description performed.

3.2 Materials and Methods

HNTs, *Staphylococcus aureus* (*S. aureus*) ATCC[®] 6538[™] 50 CFU, chloroform, methanol, ethanol, isopropanol, acetone, crystal violet, chitosan, chitosan oligosaccharide

lactate, gentamicin, agar, nutrient media, silver nitrate, copper sulphate, zinc sulphate heptahydrate, polylactic acid (all chemicals HPLC grade), titanium foil were purchased from Sigma-Aldrich (St. Louis, MO).

DC power source (VWR Accupower 500 electrophoresis power supply), platinum mesh electrodes, plastic Petri dishes, and ammeter (TekPower TP9605BT) were purchased from Amazon.com LLC (Seattle, WA). Resazurin dye from Cayman Chemicals (Ann Arbor, MI), Live/Dead[®] viability/cytotoxicity kit from Thermo Fisher Scientific (Waltham, MA). Fusion 100 Syringe pump was purchased from Chemyx, Inc. (Stafford, TX), ES-30 high voltage source from Gamma high-voltage research (Ormond Beach, FL), MakerBot Replicator Mini 3D printer from MakerBot (Brooklyn, NY) and commercial airbrush kit F2C TC-802K from Amazon (Seattle, WA).

3.2.1 Cell Culture

Cell viability response of the mHNTs was studied using preosteoblast cells, which were obtained from the American Type Culture Collection (ATCC). Briefly, cryovials were thawed and allowed to equilibrate in a water bath with a humidified CO₂ incubator at 37° C. Cells thus obtained, were cultured in T25 flasks in RPMI growth media containing 10% FBS and 1% penicillin through passage four and then frozen down and maintained in a liquid nitrogen Dewar until use. Trypsin-EDTA (0.25% trypsin, 1 mM EDTA) was used to detach cells from the culture flasks.

For each experiment (n=3), preosteoblasts were thawed and prepared as described above and used when they achieved sub-confluency. Cytotoxicity tests were performed by enzymatic detachment, rinse, and centrifugation to separate the cells, for testing the

cells were resuspended in RPMI 1640 medium with mHNTs at 20 $\mu\text{g}/\text{mL}$ for 24 hr duration, cells with no mHNTs were used as the control.

3.2.2 Live/Dead Cytotoxicity Assay

Preosteoblast cells were cultured and tested with mHNTs as described above. Cell viability was assessed using LIVE/DEAD[®] Viability/Cytotoxicity Kit (Thermo Fisher Scientific) containing polyanionic dye calcein, which is retained within living cells and produces an intense uniform green fluorescence (excitation/emission $\sim 495/\sim 515$ nm) and EthD-1, which enters cells with damaged membranes and produces a bright red fluorescence in dead cells (excitation/emission $\sim 495/\sim 635$ nm).

For viability studies, the staining solution was prepared by mixing 5 μL of 4 mM Calcein AM Solution and 20 μL of 2 mM EthD-III Solution to 10 mL of DPBS. Cell culture plates were washed twice with DBSS, and then 100 μL of staining solution was added to each well plate. These substrates were then incubated at room temperature for 30 min. Each cytotoxicity experiment was repeated three times. Images were captured using an Olympus BX51 fluorescence microscope (Olympus Corporation, Tokyo, Japan) equipped with an Olympus DP11 digital camera system.

The captured images were analyzed using ImageJ software (Schneider, Rasband, and Eliceiri, 2012).

Cell proliferation was assessed using MTS colorimetric assay which is based on the reduction of MTS tetrazolium compound to a colored formazan product soluble in culture media. 10 μL of MTS reagent was added to wells and incubated at 37° C for 1 hr and absorbance was recorded at 490 nm, background absorbance was subtracted from the medium wells containing the medium as a control.

3.2.3 Bacterial Cultures and Testing

S. aureus was used in this study; it was maintained in tryptic soy agar. For testing, the bacterial strain was cultured in nutrient broth and plated on Muller-Hinton agar plates at 37° C overnight after which a single colony was picked up using a sterile toothpick and suspended in saline solution and diluted to 0.5 McFarland standard (1.5×10^8 CFU/ml), 20 μ L of which was spread over Muller-Hinton agar plates on which the test materials were placed and incubated for 12-18 hr at 37° C and the obtained zones of inhibition were analyzed using ImageJ software.

The antibacterial potential was also evaluated against *S. aureus* using a microdilution broth assay. Samples were cut and immersed in 24 well plates containing 1-3 mL/well Muller Hinton broth (depending on the sample dimension) inoculated with 20 μ L of 0.5 McFarland standard *S. aureus*, the plates were put on a shaker, after 4 hr the samples were removed, and the absorbance of 100 μ L solution was recorded after 12 hr.

Bacterial adherence assay was performed by immersing samples into 1-3 mL/well Muller Hinton broth (depending on the sample dimension) inoculated with 20 μ L of 0.5 McFarland standard *S. aureus*, the plates were put on a shaker and samples were removed after 1 hr, and the absorbance of 100 μ L solution was recorded after 12 hr (Lima *et al.*, 2008).

Biofilm assay was performed using the crystal violet assay, briefly, samples were incubated in 2 mL nutrient broth in 48 well plates inoculated with 1 optical density (OD) *S. aureus* for 2 days at 37° C, at the end of which the plate was emptied by inverting and gently tapping in order to remove lightly attached planktonic bacteria and the remaining bacterial films were stained with aqueous crystal violet (0.1% w/v) for 10 min, which was

similarly removed by inversion and tapping to ensure optimal removal of unattached bacteria, acetic acid (30%) was added to each well to solubilize the stain and absorbance at 630 nm was recorded (O'Toole, 2011). The OD of the broths were monitored with a visible spectrophotometer at 630 nm.

3.2.4 Statistical Analysis

Statistical analysis was performed using Microsoft Excel Analysis ToolPak plugin and Origin 9.6. Linear regression was used to construct and correlate standard curves.

All experiments were done in triplicate, and one-way analysis of variance (ANOVA) with $p < 0.05$ as the significance level was utilized for statistical analysis.

Statistically significant data was reported ($p < 0.05$), and all the results were reported as mean \pm standard deviation ($p < 0.05$, $n=3$) unless specified.

3.3 Instrumentation

A Hitachi S-4800 field-emission scanning electron microscope (Tokyo, Japan) was used to examine the surface morphology of the HNTs and to visually confirm the presence of the metal coating appearing as clusters on the otherwise smooth outer surface of the HNTs. SEM-EDS was carried out using the EDAX energy dispersive X-ray analyzer linked to the Hitachi S-4800 SEM to evaluate the elemental composition and weight percentage (wt.%) deposition on the mHNTs. EDS was operated at a working distance of 15 mm at an acceleration voltage of 15 kV, and EDS spectra were analyzed using the EDAX Genesis software. The image resolution was 1024x768 with 0.246x189 μm pixel size. The system was configured to collect the backscatter electrons for EDS element mapping. Comparatively, large spot size was used, a dwell time of 256 μs was utilized, and total acquisition time was 5 min for each sample.

X-ray crystal diffraction analysis was recorded on a Bruker D8 Venture diffractometer (Bruker, Karlsruhe, German) with Cu K α 1 radiation ($\lambda = 1.5418 \text{ \AA}$). The scan speed and step size used were 2 s and 0.02° respectively, the diffraction patterns were recorded on a Philips PW 1710 X-ray powder diffractometer over 2θ within 3° to 85° .

For bulk elemental quantification, the samples were analyzed using an ARLTM Quant'X Energy Dispersive X-ray Fluorescence spectrometer (ED-XRF). The X-ray tube was operated at 30 kV for 60 live seconds, using a 0.05 mm (thick) Cu primary beam filter in an air path for silver metal detection. The XRF spectra were studied using Wintrace 7.1TM software (Thermo Fisher Scientific, Waltham, MA).

The infrared spectrum was recorded at a resolution of 4 s^{-1} with 16 scans average using a Thermo Scientific NicoletTM IR100 FTIR spectrometer (Thermo Fisher Scientific, Waltham, MA). Thermo Scientific OMNICTM software was used to study the transmittance of the chemical bonds.

Electrolysis was performed by connecting the electrodes to a DC power supply (VWR Accupower 500). UV spectra of the silver nanoparticles were recorded using the NanoDrop-2000c spectrophotometer (Thermo Fisher Scientific, Waltham, MA) set at a 250-600 nm scan range. Microplate absorbances were analyzed using Biotek 800TS microplate reader (Winooski, VT) set at 630 nm absorbance.

CHAPTER 4

ELECTROLYTIC METALLIZATION OF HALLOYSITES

4.1 Introduction

Functionalization of the HNTs outer surface with different materials, including metals, chemicals, and bioactive constituents is an active area of research. Metal deposition on the outer surface of HNTs is of interest due to its potential utility as reaction catalysts, substantial metal remediation, and antimicrobial agents; HNTs because of their cylindrical structure provide increased surface area for adsorption.

Silver (Ag) is an extensively studied metal due to its unique size-dependent properties, including electric conductivity, antimicrobial action (Prabhu and Poulose, 2012), and catalysis (Egger *et al.*, 2009). Ag nanoparticles composited with HNTs can be a suitable candidate for composite formation having potential applications in antimicrobial nanocomposites (Yatao Zhang *et al.*, 2013).

Several methods including thermal decomposition (Nicholson *et al.*, 2016), chemical reduction (Yu *et al.*, 2014), etc. exist for metallizing HNTs; however, they are limited in application due to the use of toxic reducing agents, expensive chemicals, complicated processing steps, and need for specialized equipment. Electrochemical synthesis methods are of significant interest due to control over particle size and density as a function of current flow (Rodriguez-Sanchez, Blanco and Lopez-Quintela, 2000);

further, it is an eco-friendly process as no toxic reducing agents are involved. Mills et al. have previously reported an electrochemical method for metallizing HNTs (Mills and Boyer, 2018), herein, we propose a modified electrochemical method for metallizing HNTs where the metal content of the metal-HNTs nanocomposite (mHNTs) can be controlled by varying the setup parameters including applied voltage, time, and solvent.

It was found that our method could influence the rate of silver nanoparticle reduction, resulting in free metal nanoparticles that readily adsorb to the HNTs external surface. Our results show that the wt % deposition on the HNTs external surface increased with increasing voltage, time, temperature, magnetic stirring, and voltage polarity reversal. We anticipate that our novel eco-friendly method can be further used in coating different metal, and polymer combinations on the HNTs exterior in the future.

4.2 Materials and Methods

4.2.1 Materials

Silver nitrate (AgNO_3), HNTs, ethanol, acetone, and methanol were purchased from Sigma-Aldrich (St. Louis, MO). Platinized titanium mesh electrodes (2"x3" mesh), VWR Accupower 500 electrophoresis power supply, TekPower TP9605BT USB multimeter, and silicon carbide abrasive sandpaper were purchased from Amazon.com LLC (Seattle, WA).

4.2.2 Methods

A non-sacrificial electrolysis setup was assembled consisting of two platinized titanium mesh electrodes, the electrodes were gently cleaned using silicon carbide abrasive papers and washed in distilled water under ultrasonication for 5 min in order to prepare an even surface and remove surface contamination. The electrodes were held

parallel at a 2-inch distance and connected to a DC power source (VWR Accupower 500 electrophoresis power supply) with an ammeter connected in series (TekPower TP9605BT). Briefly, ultrasonicated colloidal solution of silver nitrate (2.5 mM) and 50 mg HNTs were dispersed in a vessel (borosilicate glass container) and different voltages (5, 10, and 20 V respectively) were maintained at 80° C with polarity reversal at every 5 min (Khaydarov *et al.*, 2009) under constant magnetic stirring to reduce electrophoretic buildup at the working electrode and thus increase Ag NPs density in the solution (Figure 4-1).

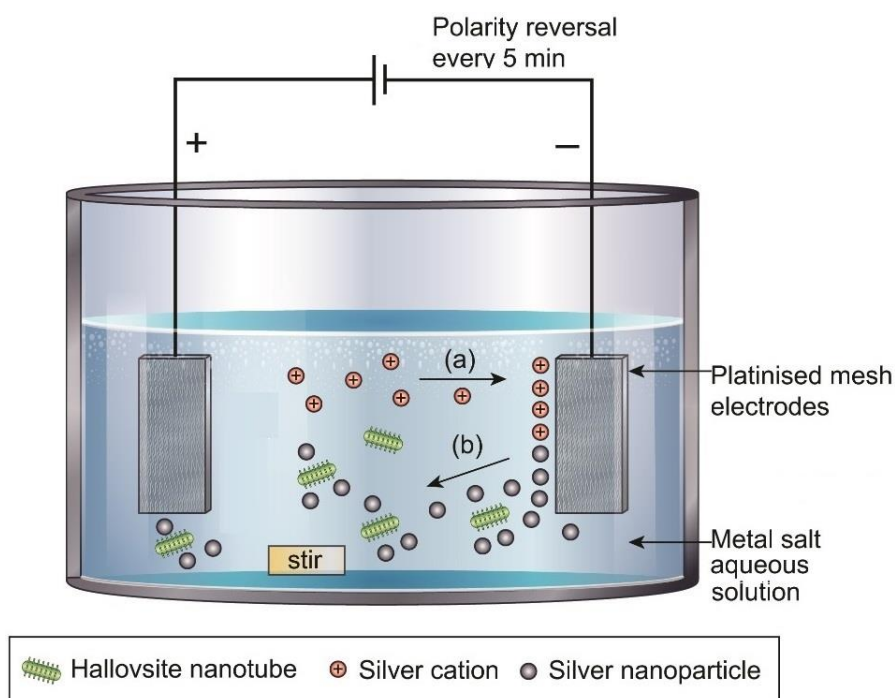


Figure 4-1: Electrolytic setup for halloysite metallization consisting of two platinum-coated mesh electrodes held 2-inch apart in aqueous 2.5 mM AgNO₃ and 50 mg HNTs at 80° C magnetically stirred suspension. Under applied electric field the three processes occur (a) cathodic migration of silver cations (b) cathodic reduction and release of neutral silver nanoparticles in the solution (c) adsorption of silver nanoparticles on the outer surface of HNTs. Polarity reversal helps in the release of reduced silver nanoparticles into the solution, magnetic stirring helps in uniform distribution and mixing with dispersed halloysites.

Each set of experiments was carried out for 20 min, afterward, the supernatant was decanted thrice, and the solution was centrifuged at 5000 rpm with water to separate AgHNTs from unreacted Ag, and dried at 30° C. The process was optimized for time (5, 10, and 20 min respectively), voltage (5, 10, and 20 V respectively) and solvent (methanol, ethanol, and water).

4.2.3 Characterization

AgHNTs were characterized using scanning electron microscope (SEM), energy-dispersive spectroscopy (EDS), X-ray fluorescence (XRF), Fourier-transform infrared spectroscopy (FTIR) and X-ray powder diffraction (XRD), and UV visible spectroscopy (UV-Vis).

4.3 Results and Discussion

Applied voltage drives the Ag^+ cathodic reduction to Ag^0 NPs, higher voltage causes greater electron flow resulting in a higher number of reduced silver nanoparticles in the system, hence increased available metal species for adsorption on HNTs surface. UV-Vis analysis of the electrolytic solution displayed characteristic absorption peaks at 400-410 nm confirming the presence of silver nanoparticles with the highest intensity at 20 V followed by 10, and 5 V respectively. The electrolytic solution was analyzed at 5, 10, and 20 min, respectively intervals and revealed a similar increase in absorption intensity with time (**Figure 4-2**).

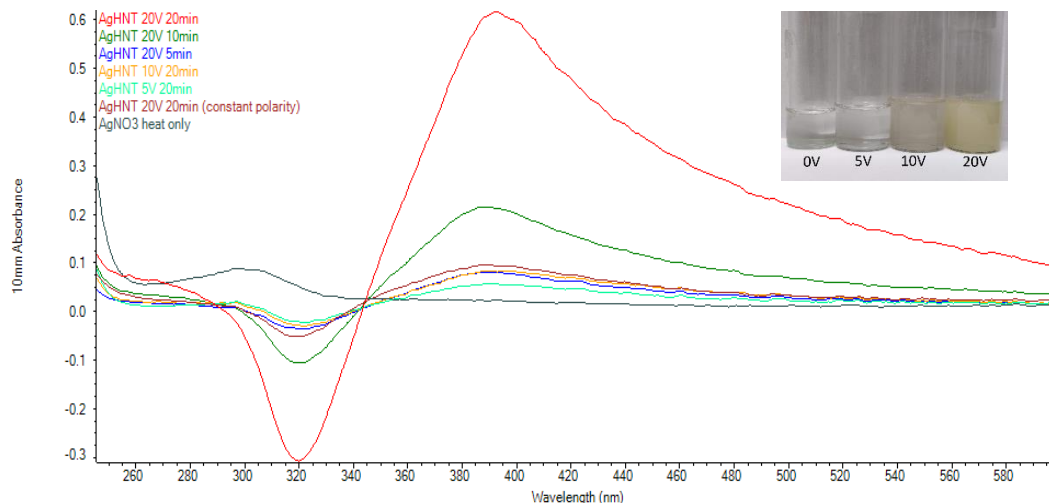


Figure 4-2: UV-Vis spectra of AgHNTs showing the highest intensity of absorption at 400 nm for AgHNTs 20V 20 min indicating a significant quantity of reduced Ag NPs in the solution, absorbance diminished with decreasing voltage and time, while application of constant polarity and heat alone led to lowest absorbances. (Inset – AgHNT 0, 5, 10, and 20 V respectively).

Figure 4-3 shows the mHNTs obtained after drying, the mHNTs obtained possessed darker color due to the presence of metal oxides.



Figure 4-3: mHNTs produced at 5, 10, 20 V respectively, increasing applied voltage led to darker colored mHNTs, which can be attributed to the quantity of metal oxide adsorbed on HNTs.

Figure 4-4 shows the SEM images of the HNTs and AgHNTs respectively, and the typical rod-shaped structure was detected for both HNTs and AgHNTs, however, in the latter, the smooth morphology was disturbed by the appearance of granules and

clusters which using EDS were confirmed to be adsorbed Ag NPs. Evidently, from the SEM it is clear that silver clusters formation occurred, this can be seen.

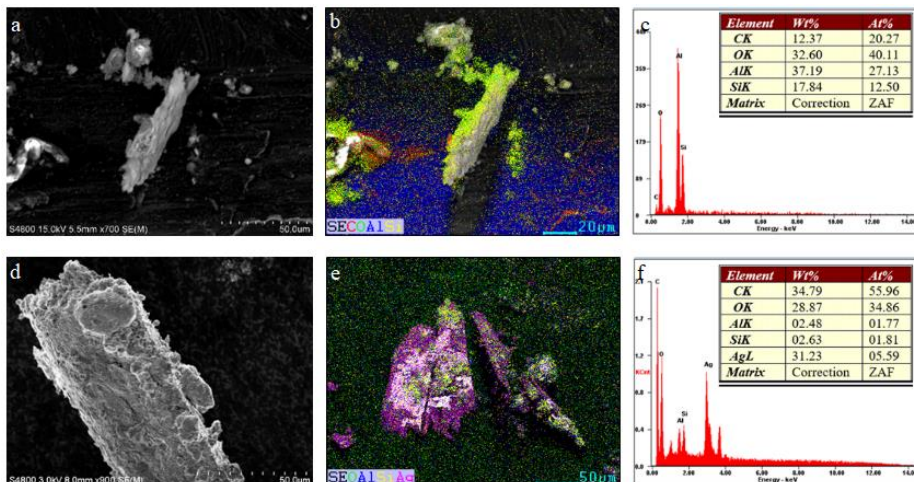


Figure 4-4: SEM, EDS-map, and EDS quantification of (a, b, c) HNTs and (d, e, f) AgHNTs. The deposition of Ag NPs in the form of granules is clearly visible on the HNTs surface and verified using EDS-map.

XRD was used to study the crystal structure of the samples (**Figure 4-5**), XRD of AgHNTs displayed overlapping peaks with HNTs (denoted by * symbol on the XRD graph, $2\theta = 11.5, 20-25, 65,$ and 77° respectively) and silver (denoted as Ag on the XRD graph, $2\theta = 38, 44, 65,$ and 77° respectively). Increased voltage led to higher metal deposition on AgHNTs, leading to stronger diffraction peaks characteristic of Ag and diminishing HNTs peaks. Signal attenuation of HNTs peaks can be explained based on the shielding effect due to increased Ag content on HNTs outer surface – silver having more metallic character than aluminum or silicon resulted in higher counts detected by the XRD.

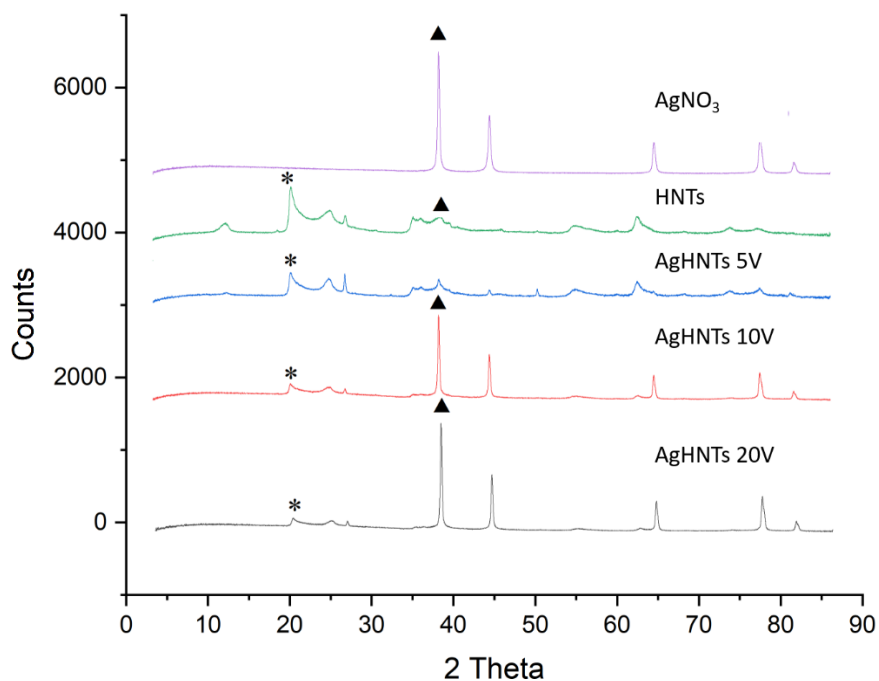


Figure 4-5: XRD pattern of AgHNTs at 5, 10, and 20V, respectively. AgHNTs 20, 10, and 5 V displaying sharp silver peaks (denoted by ▲, 111) and diminishing HNTs peaks (denoted by *, 001, 110, 002) showing HNTs reflections that became weaker with an increasing extent of metallization.

FTIR analysis of HNTs show characteristic absorption bands for at 3690, 3620, 1000, 903, and 748 cm^{-1} respectively corresponding to O-H stretching of inner surface hydroxyl groups, O-H stretching of inner hydroxyl groups, in-plane Si-O stretching, O-H deformation of inner hydroxyl groups, and perpendicular Si-O stretching respectively (Figure 4-6).

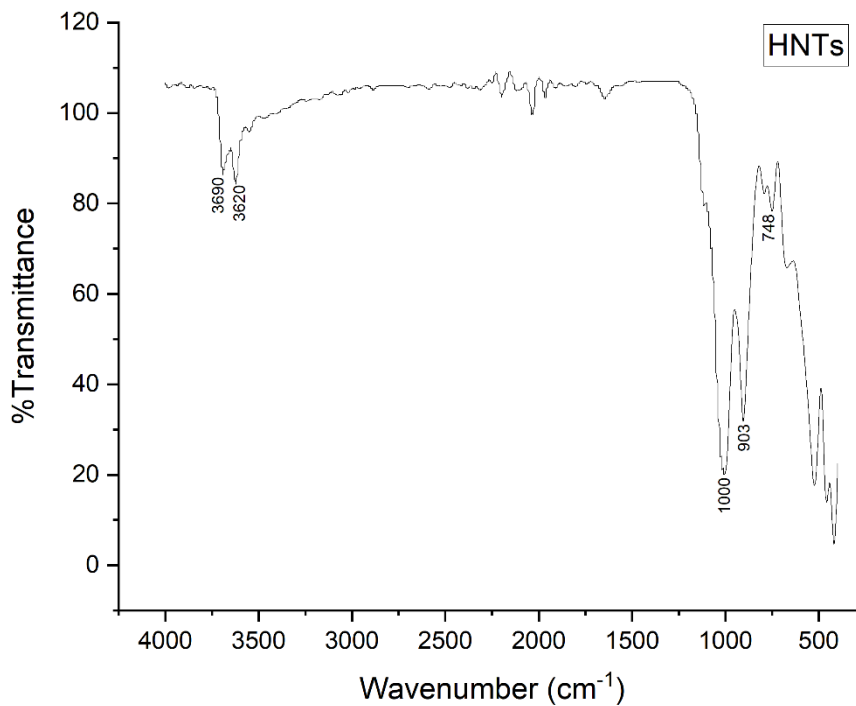


Figure 4-6: FTIR pattern of as received HNTs displaying the characteristic FTIR pattern. The characteristic peaks around 3690, 3620, 1000, and 903 cm^{-1} respectively corresponding to O-H stretching of the inner surface hydroxyl groups, O-H stretching of inner hydroxyl groups, Si-O stretching vibrations, and Al-OH vibrations respectively.

The XRF intensity spectra is shown in **Figure 4-7** The intensity increased with an increase in the voltage, duration of the electrolytic process, and by employing polarity reversal.

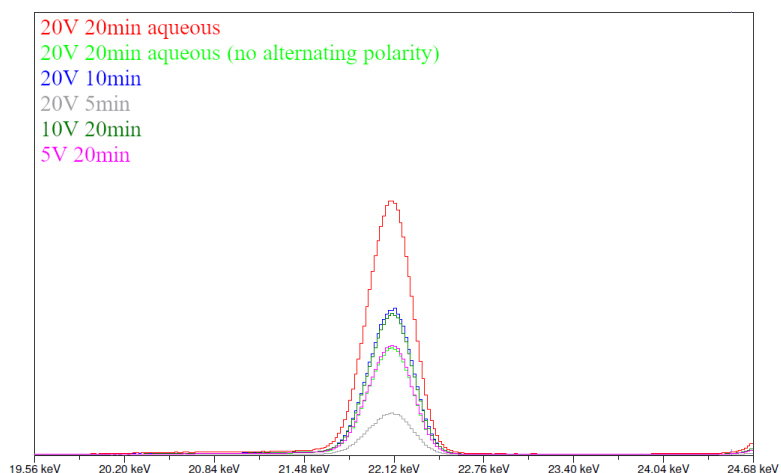


Figure 4-7: XRF spectra for 20V, 20 V(no polarity reversal), 20 V 10 min, 20 V 5 min, 10 V, and 5 V. 20 V in the aqueous medium along with polarity reversal every 5 min lead to the highest concentration of Ag NPs indicated by greater XRF intensity. (all experiments in aqueous media, with regular polarity reversal and 20 min duration unless indicated).

Figure 4-8 displays the XRF intensity spectra recorded when different solvents were employed, and the highest spectra were obtained for an aqueous solvent, followed by methanol and ethanol.

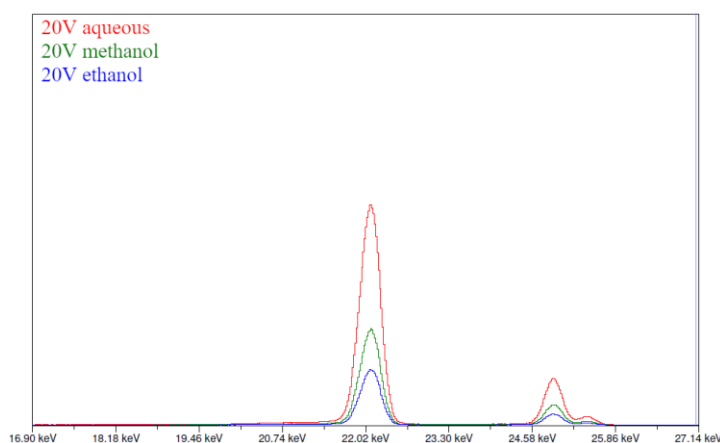


Figure 4-8: XRF spectra for 20 V 20 min in aqueous, isopropanol, methanol, and ethanol solvents with polarity reversal. Aqueous media having higher dielectric constant led to higher conductivity leading to increased electrolysis and a higher concentration of Ag NPs.

EDS analysis revealed an increasing Ag wt.% content in AgHNTs with increasing voltage, which was further analyzed using EDS mapping and validated using EDXRF which confirmed the same results, additionally, using EDS mapping it was confirmed that almost whole HNTs exterior surface was covered with silver metal uniformly, thus silver was successfully deposition on HNTs was confirmed, with increasing voltage (5, 10, and 20 V respectively) the Ag wt.% was found to increase, a similar observation was made with increasing the electrolysis time duration. In order to validate the findings, a control experiment was conducted using heat, stirring and voltage as the control factors and it was found that in the absence of voltage (0 V) stirring and heating by themselves and in combination could result in minor Ag wt.% deposits, while application of voltage led to significantly increased deposits thus validating the hypothesis (**Figure 4-9**). Furthermore, at constant polarity lower deposition was observed due to increased reduced species cathodic adherence leading to a reduction in current density and reduced Ag NPs density, by employing polarity reversal the reduced Ag NPs were released into the system. Similar wt.% have been reported by a previous study on electrochemical metal deposition on HNTs where 26 and 10 wt.% respectively of Ag and Cu were found to be deposited on HNTs respectively (Boyer, 2016).

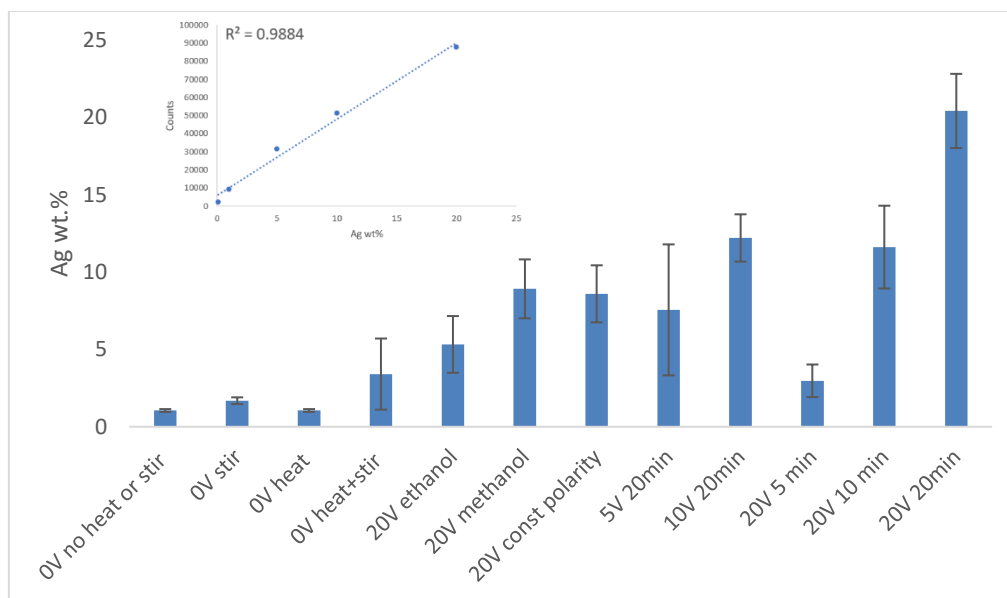


Figure 4-9: XRF analysis of Ag wt.% deposition on HNTs. Application of only heating or stirring or both in combination led to a small amount of metal deposition on HNTs, which increased with the application of voltage, time and polarity reversal, (all samples – 20 min in aqueous medium unless stated otherwise). Inset – calibration curve for XRF standards.

Water was found to be the most optimum medium for electrolysis because of its high dielectric constant leading to higher amperage and increased ionization of the hydroxide groups on the outer surface of HNTs thus increasing the degree of adsorption. 20 min electrolysis process at 20 V with polarity reversal every 5 min in the aqueous medium was found to be the most optimum parameters for metallizing HNTs. Higher voltage results in higher amperage caused an increased amount of electron flow, which resulted in higher rates of reduction (cathode) and oxidation (anode), hence, a higher number of reduced silver species.

The above results can be explained based on the ionic density, which increased with applied voltage as a function of the current flowing through the system (**Figure 4-10**). The findings can be electrochemically explained as a series of the following steps (**Figure 4-11**) -

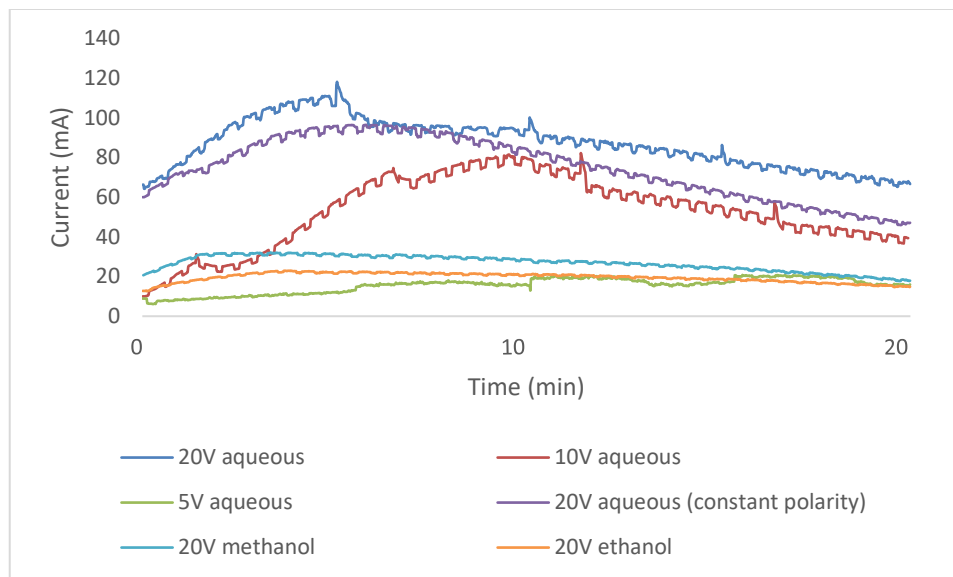
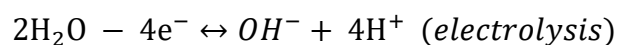


Figure 4-10: Current (mA) Vs. time (s) for AgHNTs electrolysis in different solvents. Compared to methanol and ethanol, water has the highest dielectric constant and exhibited the highest current as a function of the applied voltage. Application of constant polarity resulted in sharper current drop over time, which can be due to a buildup of reduced species on the cathode which was countered by reversing polarity.

Step 1: On dissolution and further application of voltage AgNO_3 splits into Ag^+ and NO_3^- , and water splits into OH^- and H^+ ions, respectively.

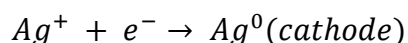


Step 2: Ag^+ forms hydration cation $\text{Ag}^+(\text{H}_2\text{O})_6$ and migrates towards the cathode, simultaneously, NO_3^- moves towards the anode.

Step 3: Water molecules detach, and Ag^+ enters the Helmholtz double layer.

Step 4: Ag^+ adsorbs to the cathode as an adatom (Jayakrishnan, 2012).

Step 5: Ag^+ ions compared to H^+ ions have higher reduction potential; hence, they get reduced more readily.



Ag^+ gets reduced to Ag^0 which diffuses on the cathodic surface, grows via nucleation and van der Waals forces and due to stirring, and polarity reversal gets released into the system.

Step 6: Ag^0 gets adsorbed on the HNTs surface resulting in $AgHNTs$.

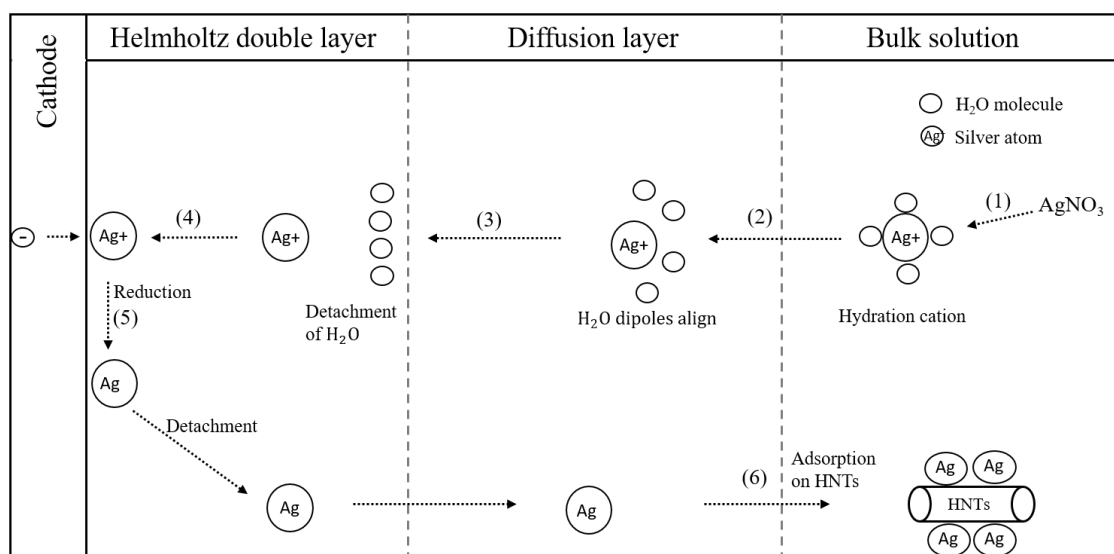
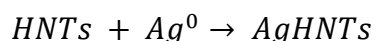


Figure 4-11: Schematic representation of the cathodic reduction of Ag in electrodeposition.

Additionally on increasing the applied voltage, the reversible electrolysis reaction ($AgNO_3 \leftrightarrow Ag^+ + NO_3^-$) is further shifted to the right, and more Ag^+ ions are available in the system that can interact with the HNTs, which can be explained based on Faraday's law of electrolysis (**Eq. 4-1**) -

$$n = \frac{It}{zF} \quad \text{Eq. 4-1}$$

Where n is the number of moles of ions reduced, I is the current in amperes, t is the time in seconds, z is valence number of the ion reduced, and F is Faraday's constant (96.48 c/mol). Hence, increasing current and electrolysis duration leads to a more

significant number of Ag NPs in the system resulting in higher wt.% deposition on AgHNTs. On reversing the voltage, more Ag NPs are released, leading to increased Ag np concentration resulting in more significant deposition on HNTs. Water having a higher dielectric constant (78.5) when compared to methanol (32.6) and ethanol (24.3) leads to higher current flow with time (charge), hence a higher reduction of silver (Reichardt and Welton, 2011).

4.4 Conclusion

Several methods exist for HNTs surface metallization however they are limited by complicated pre-processing, expensive reagents, toxic reducing agents and lack of regulation on the degree of surface metallization on HNTs, which is a crucial element in the application of metallization of HNTs, e.g., high degree of metallization can potentially increase antimicrobial action whereas comparatively lowering the metallization can help in constructing more biofriendly HNT composites.

Here, we describe a novel electrolytic method that can regulate the wt.% metallization of HNTs exterior using metal salt (AgNO_3) and distilled water using electricity to generate metal NPs (Ag) which adsorb on the HNTs outer surface resulting into AgHNTs, further, increased voltage led to an increase in current flow through the system resulting in higher ionic concentration which further contributed to increased metal deposition in HNTs.

CHAPTER 5

DIFFERENTIAL ANTIMICROBIAL AND CELLULAR RESPONSE OF ELECTROLYTICALLY SYNTHESIZED HALLOYSITES HAVING DIFFERENT AMOUNTS OF SURFACE METALLIZATION

5.1 Introduction

Halloysite nanotubes (HNTs) is a dioctahedral 1:1 nanoclay made of rolled-up layers of aluminosilicate sheets, it is a material of interest due to its high adsorption capacity, unique surface, and lumen charge polarity chemistry, non-toxicity, wide distribution, and low cost (Joussein *et al.*, 2005). Over the years it has generated interest as an adsorbent surface for various antimicrobial (Shu *et al.*, 2017), catalytic (Carrillo and Carriazo, 2015), and heavy metal remediation (Hermawan *et al.*, 2018), as a container for various chemicals including drugs (Patel *et al.*, 2016), dyes (Zhao and Liu, 2008), and metals (Vinokurov *et al.*, 2017), as a filler for structural modification in bone cements (Jammalamadaka, Tappa and Mills, 2018), dental fillings (Chen *et al.*, 2012), and polymers (Boyer *et al.*, 2018).

Metals inhibit bacterial growth by inducing oxidative stress and the production of reactive oxygen species (Turner, 2017). Metal nanoparticles (NPs) including silver, zinc, and copper are used commercially due to low cost, abundance and relatively less toxicity, however, owing to extremely high surface energy they agglomerate into larger particles thereby diminishing the desired effects (Seil and Webster, 2012), this can be resolved by

using surfactant materials such as polyvinylpyrrolidone, polyethylene glycol, and sodium citrate, however, this has proven to be a temporary band-aid fix at best due to associated high costs, intricate pre and post-processing steps and possible eco-toxicity (Kvitek *et al.*, 2008). HNTs can be a viable solution to this problem as they can adsorb metal NPs thus reduce their agglomeration (Zhang *et al.*, 2016) and potentiate a more sustained metal NPs release in a system by desorption, and therefore increase the likelihood of achieving more pragmatic utilities and results.

The deposition of metal NPs on HNTs is a straightforward process because of their inherent adsorbent ability, which can be further augmented using chemical modifications. In this study we employ a modified electrolytic method based on a process described previously by Mills *et al.* (Mills and Boyer, 2018) for metallizing HNTs, we utilized electrolytic parameters as a means to regulate the metal nanoparticles population in the electrolytic system, hence affect the metal NPs density surrounding and interacting with the HNTs and thus affect the quantity of adsorption. Different amounts of available metal content in a system can confer contrasting antimicrobial/cellular responses; hence, it is essential to assess the antimicrobial and cellular responses as a function of metal content.

In this study, we demonstrate an electrolytic synthesis of reduced metal species and their adsorption on HNTs and study its contrasting antimicrobial and cellular response in *Staphylococcus aureus* and preosteoblast cells, respectively. Different mHNTs (m=silver, copper, or zinc) were synthesized electrolytically having metal content within 5-30 wt.% range at two different voltages 5 and 20 V respectively.

5.2 Materials and Methods

5.2.1 Materials

AgNO₃, CuSO₄, ZnSO₄ (99.9% pure), HNTs, ethanol, acetone, propanol, methanol, live-dead kit, Mueller Hinton broth, and agar were purchased from Sigma-Aldrich (St. Louis, MO). Resazurin dye from Cayman chemicals (Ann Arbor, MI),

Platinized titanium mesh electrodes (2"x3" mesh), VWR Accupower 500 electrophoresis power supply, TekPower TP9605BT USB multimeter, and silicon carbide abrasive sandpaper were purchased from Amazon.com LLC (Seattle, WA).

5.2.2 Methods

mHNTs were prepared using a modified protocol based on an electrolytic metallization procedure previously described by Mills et al. (Mills and Boyer, 2018). Briefly, an electrolysis setup was assembled consisting of two platinized titanium mesh held parallel at a 2-inch distance and connected to a DC power source (VWR Accupower 500). Ultrasonicated 100mL aqueous solution of metal salts (2.5 mM) and 50 mg HNTs were dispersed in glass beaker and voltages of 5 and 20 V respectively were maintained at 80° C with polarity reversal every 5 min interval (Khaydarov *et al.*, 2009) with constant magnetic stirring to reduce electrophoretic buildup at the working electrode and thus increase reduced species density in the solution, afterward the supernatant was decanted thrice, and the solution was centrifuged at 5000 rpm for 5 min with water to separate out mHNTs from un-adsorbed metal particles and dried at 30° C (**Figure 5-1**).

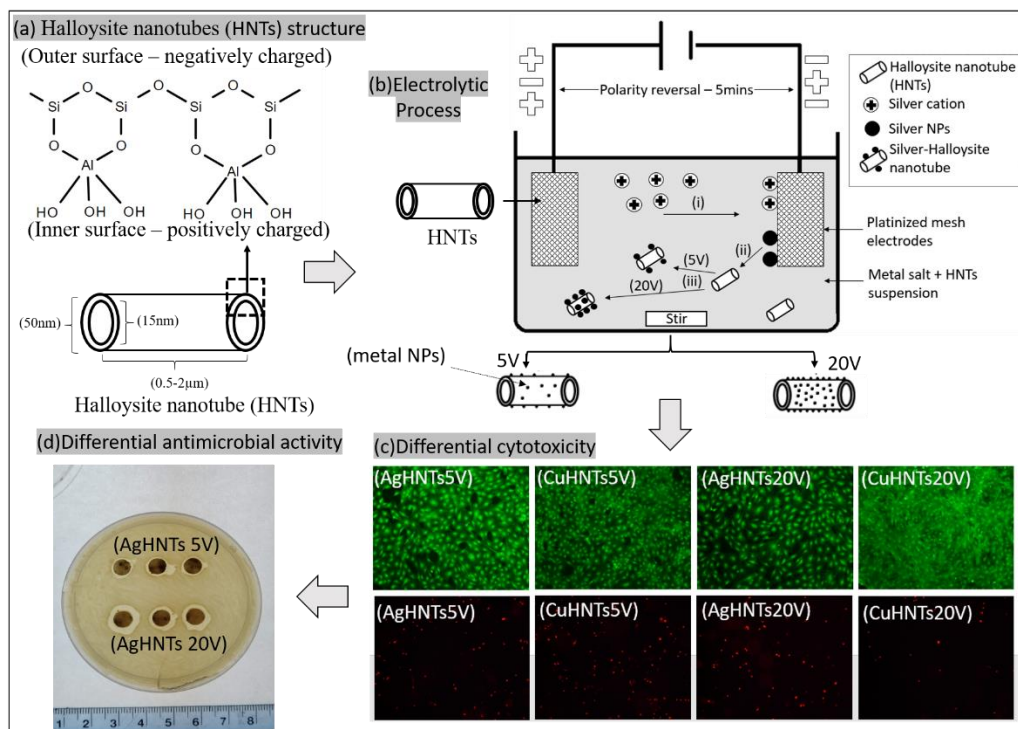


Figure 5-1: Graphical abstract- (a). HNTs chemical structure, morphology, and SEM-EDS graph, (b). Electrolytic process for metallizing HNTs at 5 and 20 V respectively and SEM-EDS graph.

mHNTs discs for antimicrobial assay were prepared using a previously described protocol, 6 mm discs were punched from Whatman no three filter paper, and 1 mg of mHNTs in 2 mL ethanol was gradually infused using an automatic pipette, the discs were dried in an incubator at 37° C (Kramer and Kirshbaum, 1961).

Resazurin assay was used for qualitative minimum inhibitory concentration determination, where, 0.25 mg of mHNTs were serially diluted in 100 μ L of Mueller Hinton broth and inoculated with 10 μ L of 0.5 McFarland standard (1.5×10^5 CFU/ml) of *S. aureus* gram-positive bacteria and incubated in wells of a 96 well plate at 30° C for 6 hr after which 20 μ L of 0.0015 w/v% resazurin aqueous solution was added to each well.

Live bacteria cells reduce the blue non-fluorescent resazurin to pink fluorescent resorufin, thus providing a direct analysis of the bacterial metabolic activity (Elshikh *et al.*, 2016).

Preosteoblasts cells were cultured, live/dead, and proliferation tests were performed as described in chapter 3.

ImageJ (Schneider, Rasband, and Eliceiri, 2012) was used for counting fluorescent cells from thresholded 8-bit images at 50-200 pixel² cell size limit.

5.2.3 Characterization

mHNTs were characterized using scanning electron microscope (SEM), energy-dispersive spectroscopy (EDS), X-ray fluorescence (XRF), Fourier-transform infrared spectroscopy (FTIR), UV Visible spectroscopy (UV-Vis) and X-ray powder diffraction (XRD). The mHNT could be easily differentiated using the characterization methods more ever contrasting bacterial and cellular responses were obtained based on the extent of metallization.

5.3 Results and Discussion

mHNTs with contrasting metal content were synthesized by application of 5 and 20 V respectively which could easily be distinguished by visual analysis of the obtained samples which turned darker with an increasing metal content as shown in **Figure 5-2**.



Figure 5-2: The natural white color of the HNTs was altered to darker colors depending on the type of metal used and quantity adsorbed.

SEM-EDS analysis revealed a positive correlation between applied voltage and metal content (wt.%) adsorption on mHNTs, which is evident in terms of increased surface deposition on otherwise smooth HNTs, at 5 V HNTs surface was visible in SEM with dispersed patches of metal whereas at higher voltage 20 V almost complete outer surface was covered (**Figure 5-3**).

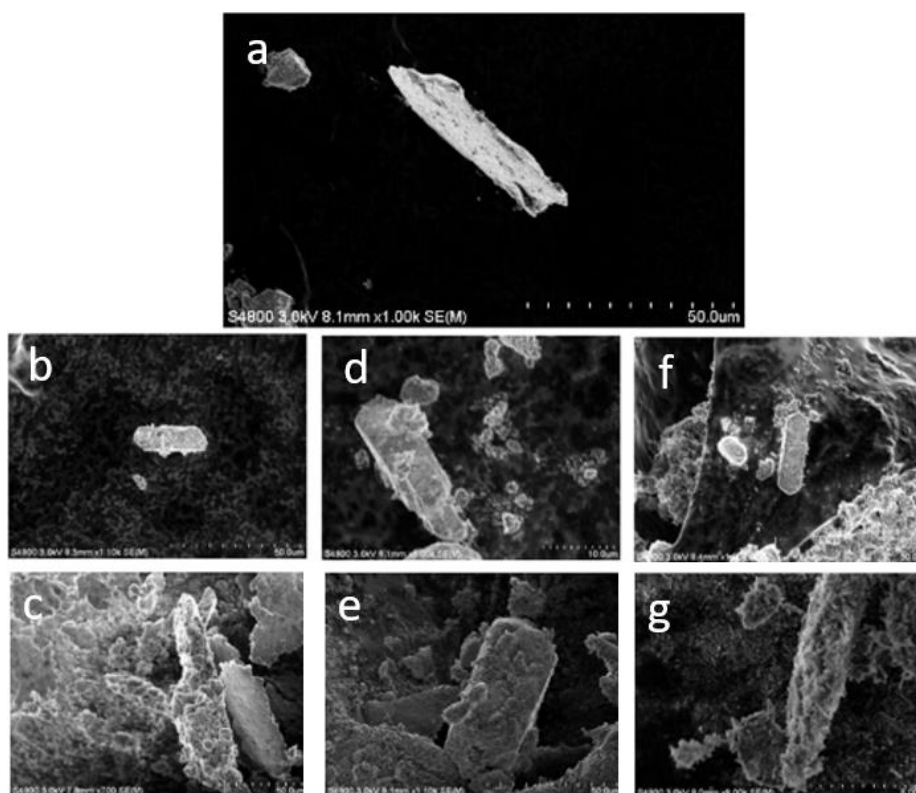


Figure 5-3: SEM of (a) HNTs, (b, c) AgHNTs 5 and 20V, (d, e) CuHNTs 5 and 20 V, and (f, g) Zn HNTs 5 and 20 V respectively. Metal content on HNTs outer surface increased with the applied voltage (5-20 V).

The findings were confirmed using XRF, where an increasing amount of metal content was observed as a function of voltage increment (**Figure 5-4**).

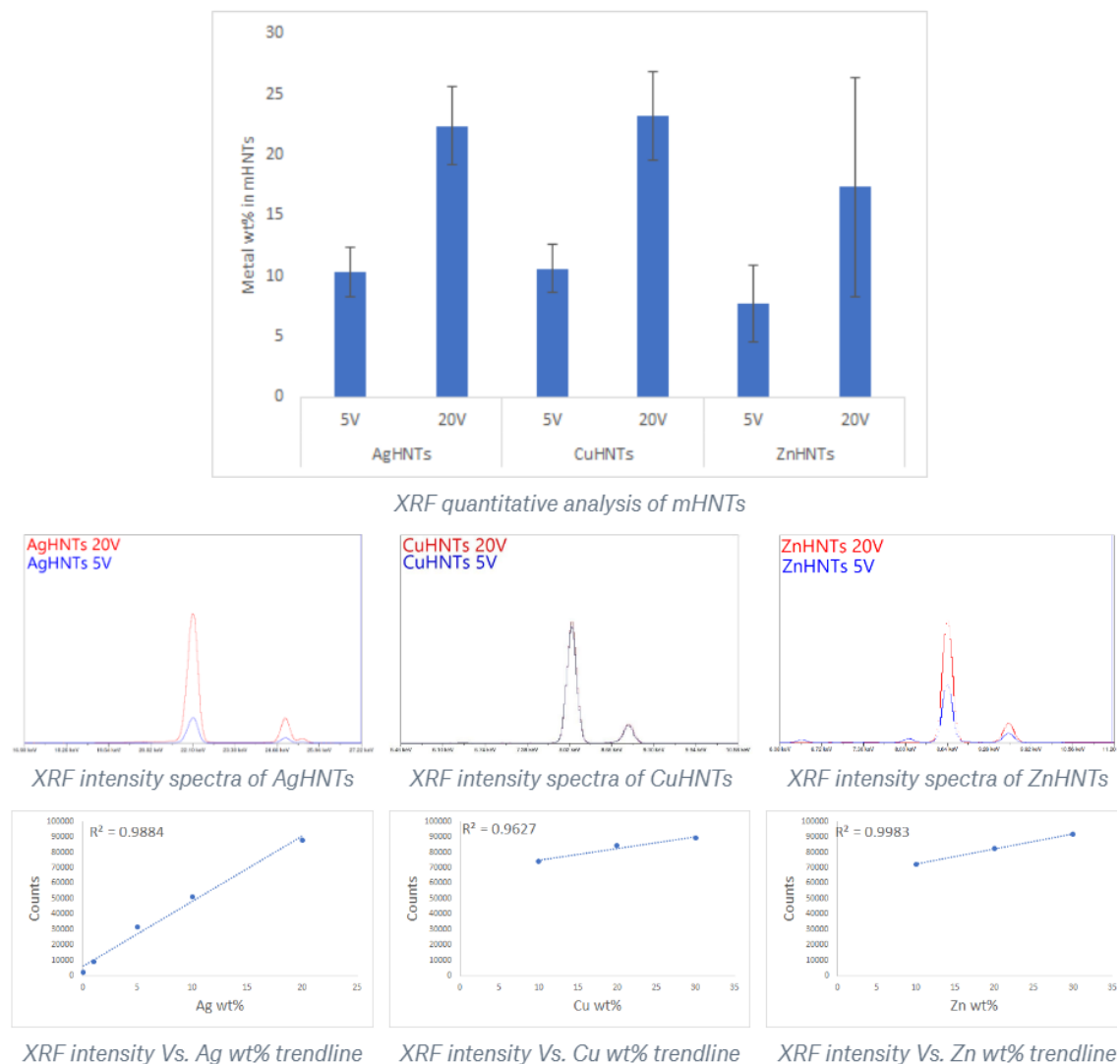


Figure 5-4: XRF quantitative analysis of Ag, Cu, and ZnHNTs, respectively. Adsorbed metal content in mHNTs increased with applied voltage (5 and 20 V).

A similar trend was observed in the XRD spectra, where increasing respective metal peak intensities were observed with increased metal content. In general, higher applied voltage samples displayed stronger corresponding metal and subdued halloysite peaks, respectively, whereas low voltage samples exhibited the contrary, i.e., stronger halloysite and weaker metal peaks respectively (**Figure 5-5**).

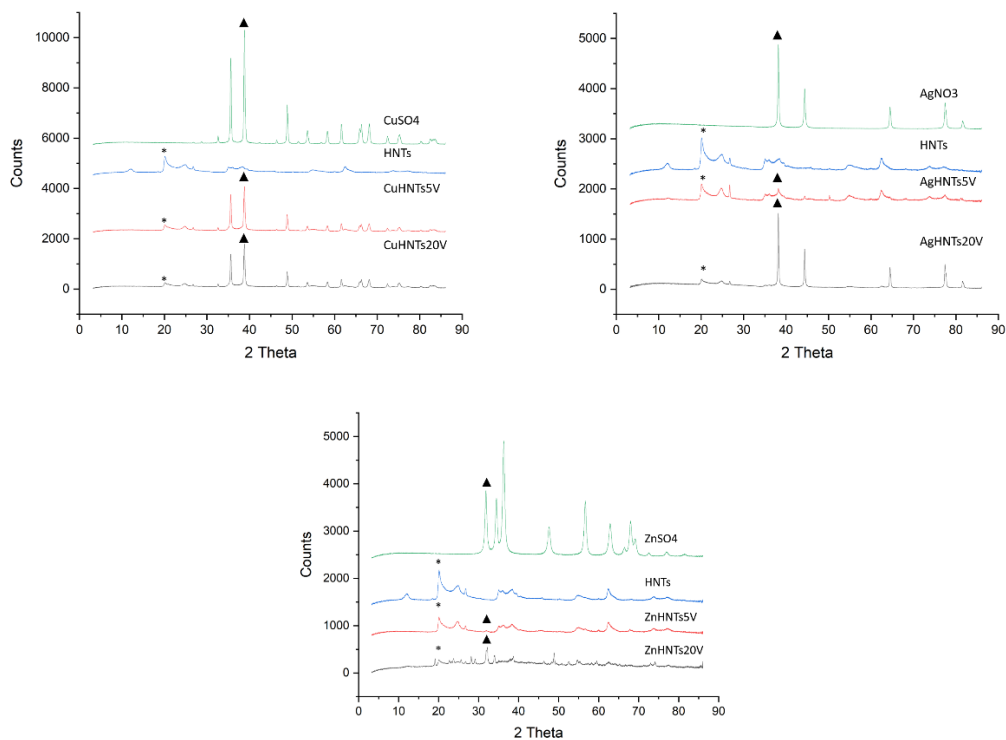


Figure 5-5: XRD spectra of AgHNTs, CuHNTs, and ZnHNTs. Increased applied voltage led to higher metal adsorption, hence more intense corresponding metal peaks and attenuated HNTs characteristic peaks. (* represents HNTs peak, ▲ represents metallic peak).

FT-IR analysis of HNTs showed the inner and outer layer Al-OH stretching at 3690 and 3620 cm^{-1} , in-plane Si-O-Si stretching at 1000 cm^{-1} and 1091 cm^{-1} , and symmetric Si-O-Si stretching at 748 cm^{-1} (**Figure 5-6**).

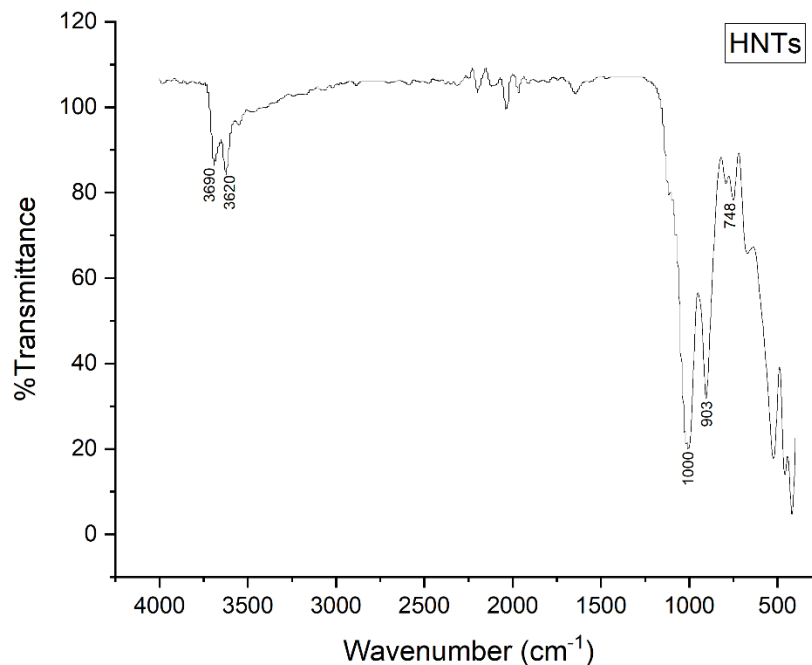


Figure 5-6: FTIR pattern of as received HNTs displaying the characteristic FTIR pattern. The characteristic peaks around 3690, 3622, 1031, and 903 cm^{-1} respectively corresponding to O-H stretching of the inner surface hydroxyl groups, O-H stretching of inner hydroxyl groups, Si-O stretching vibrations and Al-OH vibrations were recorded.

Amperage was recorded, and higher currents were detected for higher voltages (Figure 5-7), which was due to higher ionization of metal salt electrolytes leading to increased ionic density in the solution resulting in increased population of metal nanoparticles interacting with HNTs surface leading to corresponding increased metal wt.% in mHNTs with increased applied voltage.

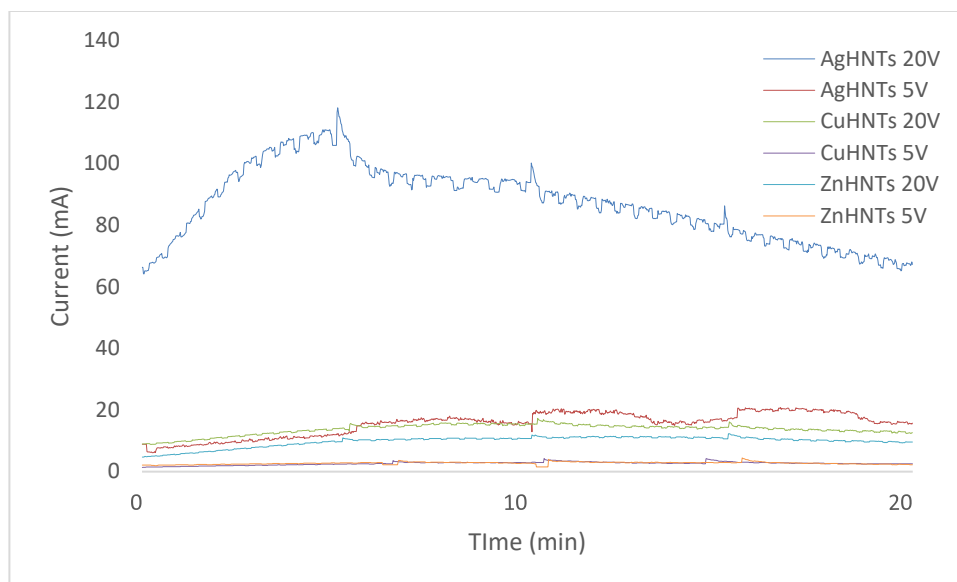


Figure 5-7: Current (mA) Vs. time (min) for mHNTs samples in aqueous electrolytic setup, the amount of current flow recorded as a function of the conductivity of the individual metal salts, solvents, and applied voltage.

A similar trend was observed in UV-Vis analysis revealed increased ion concentration for silver, copper, and zinc salts, respectively, with an increasing voltage at 420, 228, and 360 nm respectively (**Figure 5-8**).

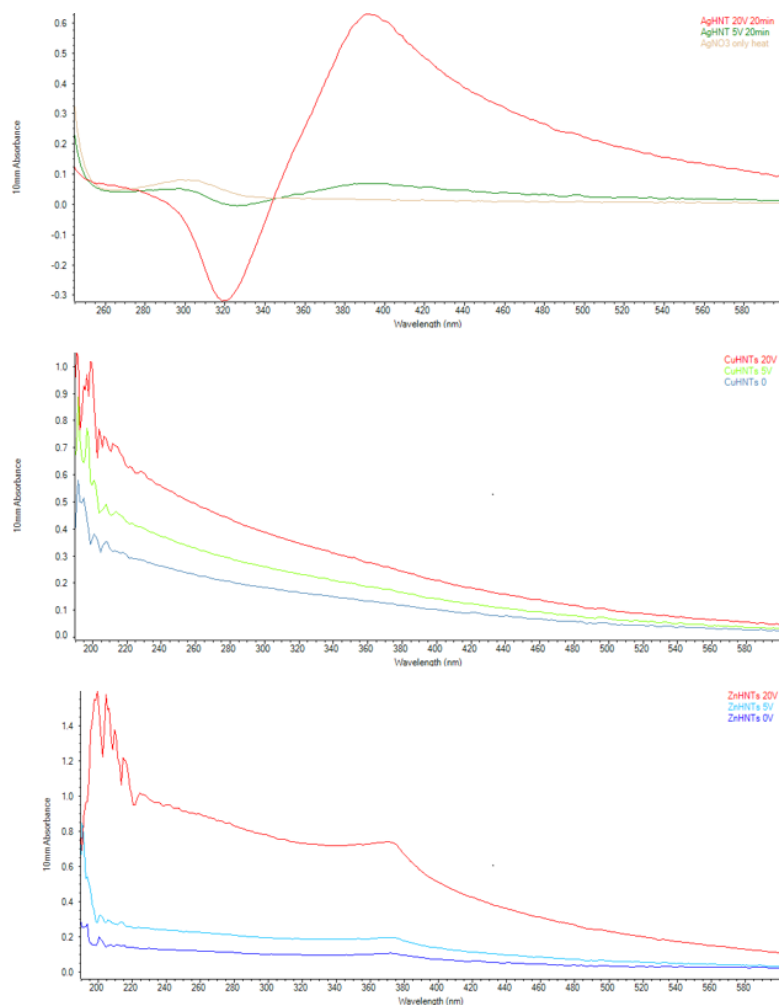


Figure 5-8: UV-Vis spectra of mHNTs (m=Ag, Zn, or Cu, respectively).

mHNTs were evaluated for antimicrobial effect on *S. aureus* using resazurin dye assay, a positive correlation was observed between observed minimum inhibitory concentration (MIC, at least 3 out of a total of 4 wells are dark blue in appearance, n=4) and metal content of mHNTs. MICs for AgHNTs (0.25 and 0.125 mg/mL respectively), CuHNTs (none and 0.25 mg/mL respectively), and ZnHNTs (0.125 and 0.25 mg/mL respectively) at 5 and 20 V respectively were observed (**Figure 5-9**).

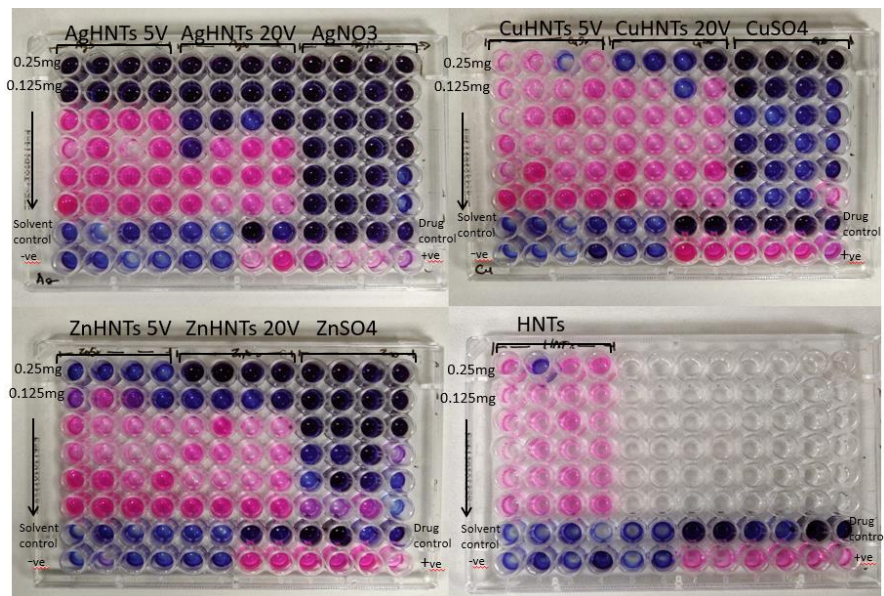


Figure 5-9: Determination of MIC for mHNTs against *S. aureus* using resazurin assay. Purple well corresponds to dead, whereas partially purple/pink, and pink wells correspond to live bacteria, (n=4).

Disc diffusion assay was performed using agar (**Figure 5-10**), and a similar pattern was obtained, it was found that mHNTs at 20 V had higher average zones of inhibitions than mHNTs produced at 5 V (**Figure 5-11**).

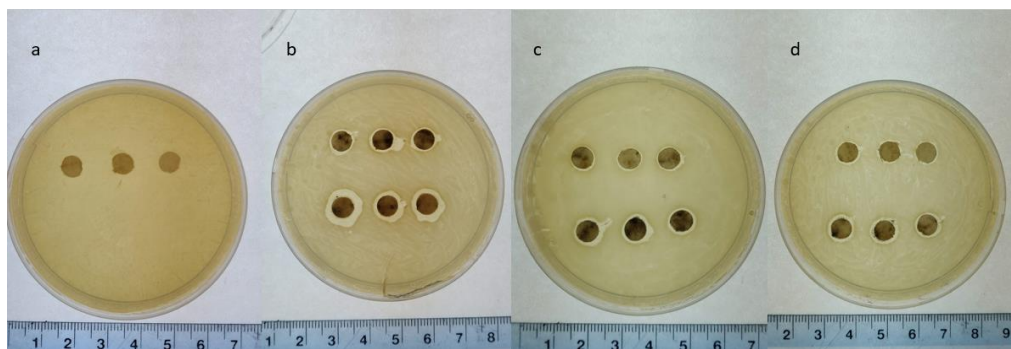


Figure 5-10: Disc diffusion assay of (a) HNTs, (b) AgHNTs, (c) CuHNTs, (d) ZnHNTs, (5 V -top, 20 V- bottom). HNTs exhibited no antimicrobial activity, for each set of metal coating the mHNTs antibacterial activity was found to be corresponding to the amount of metal deposit on HNTs.

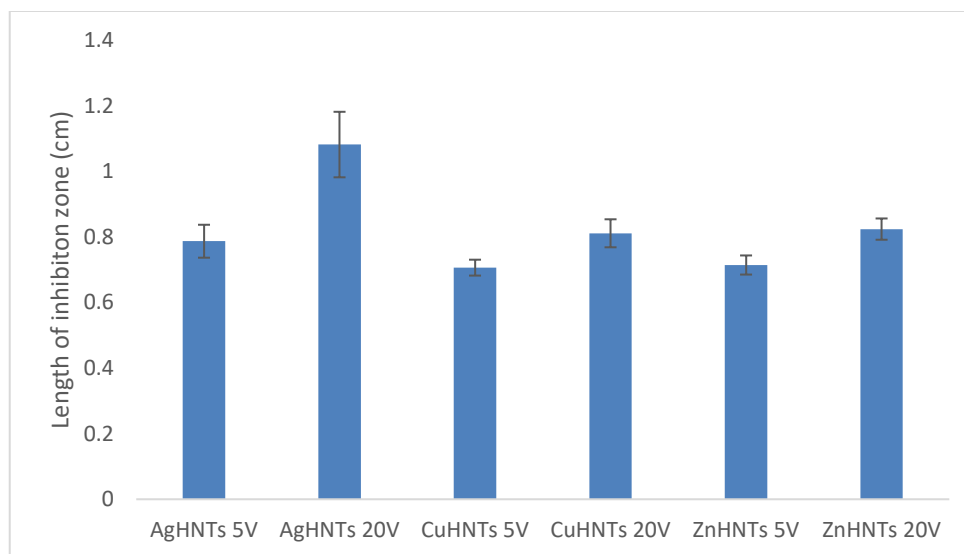


Figure 5-11: Inhibition zones from the disc diffusion assay.

Cell viability of preosteoblasts was assessed for metal salts and AgNO_3 was found to be most cytotoxic (**Figure 5-12**).

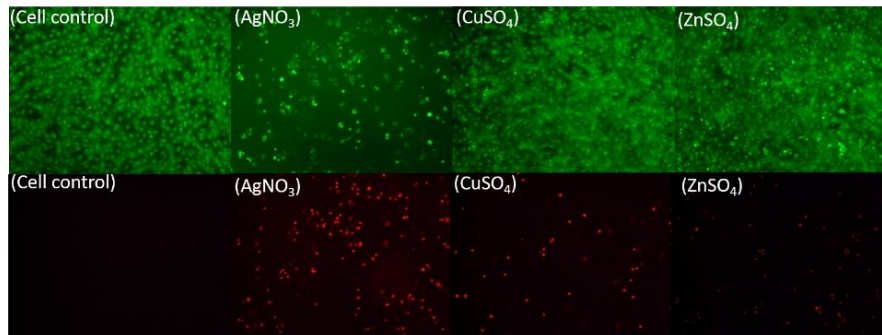


Figure 5-12: Live/Dead assay, preosteoblast cells were cultured in the presence of metal salts. Live cells (green), dead cells (red).

Similar trends in cell viability studies for preosteoblasts were obtained for mHNTs (**Figure 5-13**). A decreased cell viability and proliferation with increased silver metal wt.% content in AgHNTs was observed whereas CuHNTs and ZnHNTs exhibited a reverse trend, i.e. increased amounts of Cu/Zn metal in mHNTs led to higher cellular proliferation.

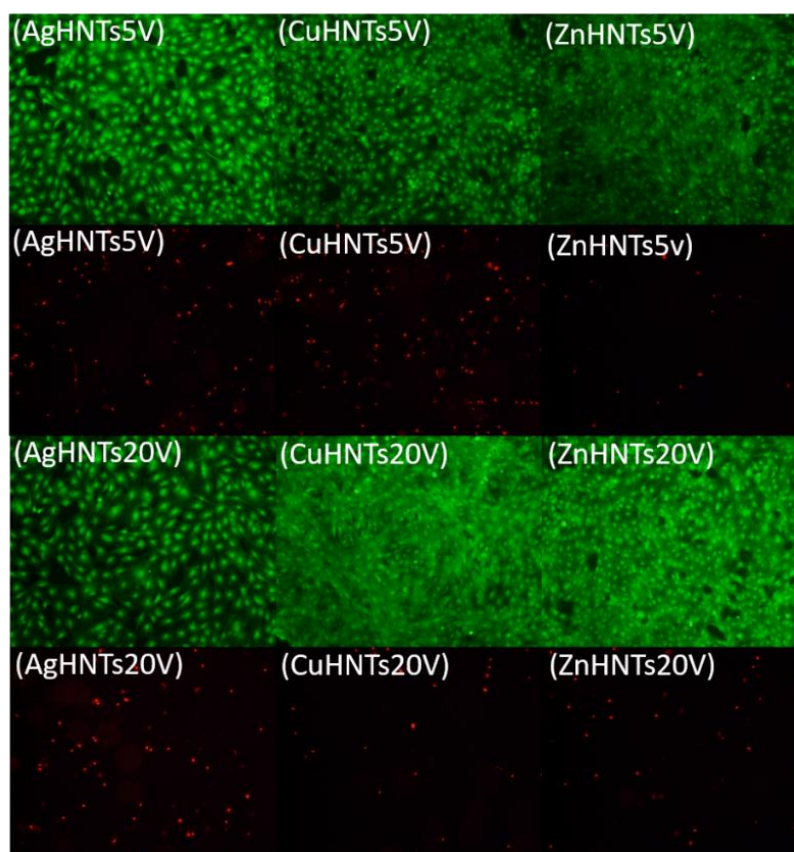


Figure 5-13: Live/Dead assay, preosteoblast cells were cultured in the presence of mHNTs. Live cells (green) and dead cells (red).

Comparable observations were found on cell count analysis using ImageJ (**Figure 5-14**).

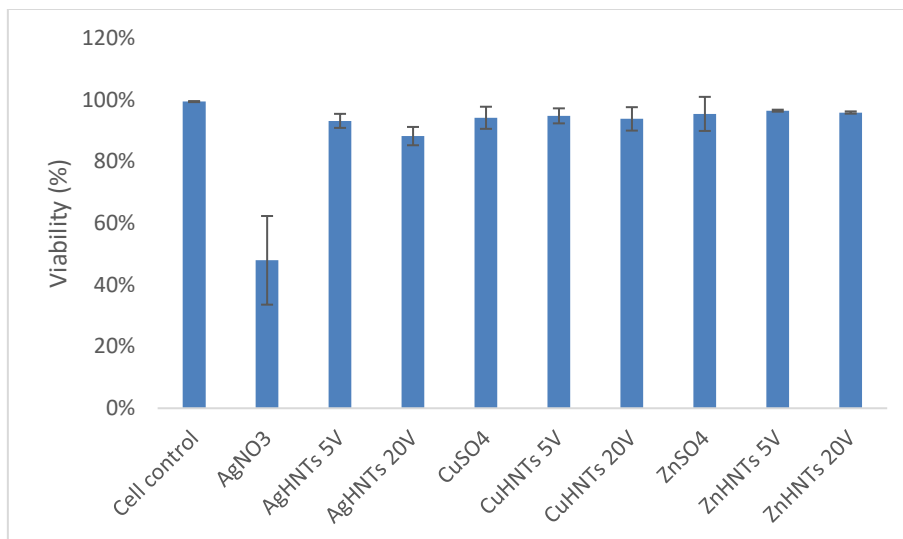


Figure 5-14: Cell viability assay for mHNTs. AgNO₃ was found to be most toxic to cellular viability, and the toxicity reduced when adsorbed to HNTs. CuHNTs and ZnHNTs displayed slightly increased cellular viability with increased concentration adsorbed on HNTs.

An almost comparable trend was observed in cell proliferation studies (**Figure 5-15**). The data suggested ZnSO₄ and ZnHNTs 20 V the most conducive to preosteoblast growth.

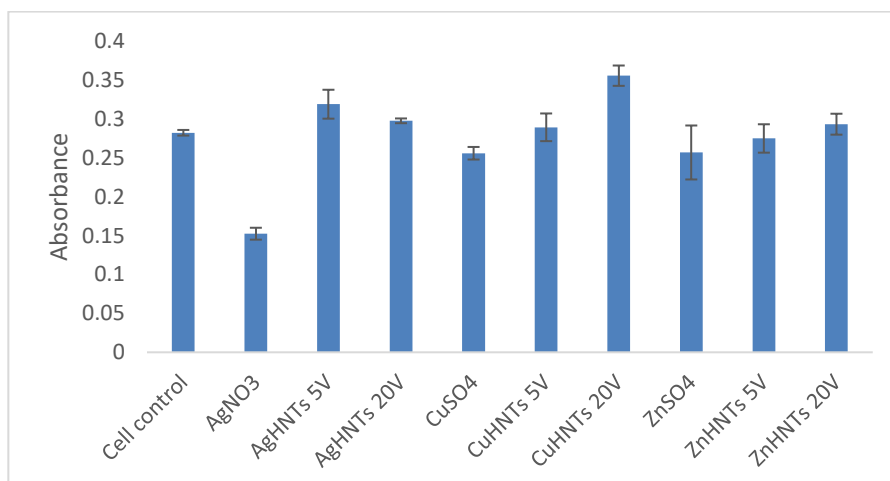


Figure 5-15: Cell proliferation assay for mHNTs, a similar trend as cell viability was observed.

Silver being a toxic, non-essential element lead to increased cytotoxicity hence resulted in a lower number of live and higher number of dead cells (depicted by green and red respectively) whereas copper and zinc being essential elements that participate as cofactors in cellular metabolism and processes led to increased cell viability.

5.4 Conclusion

Several methods exist for metallizing HNTs; however, they may be limited in scope because the extent of HNTs metallization is not regulated or considered, which, as demonstrated above is a vital parameter to be considered. Here, we demonstrate a method for metallizing HNTs exterior surface and attempt to modulate the quantity of metal decoration on HNTs as a function of applied voltage and demonstrate their contrasting effects on gram-positive bacteria and preosteoblast cell lines. In the future, we anticipate developing more methods to obtain differential metal depositions on HNTs and scale up to the deposition of more than two metals.

CHAPTER 6

ELECTROPHORETIC DEPOSITION OF GENTAMICIN LOADED ZNHNTS-CHITOSAN ON TITANIUM

6.1 Introduction

Electrophoretic deposition (EPD), a surface coating method is essentially a two-step process comprising of movement of charged materials under applied electric field and accumulation and deposition of charged material on an oppositely charged electrode (Augello and Liu, 2015).

Stainless steel was previously the material of choice for orthopedic implants, lately, it has been replaced with titanium due to its superior strength, durability, and corrosion resistance, however, titanium also faces several drawbacks including low osseointegration, biofouling leading to post-surgical infections leading to a variety of complications which based on the patient's clinical condition can be potentially remedied by coating anti-biofouling materials on implant surfaces (Prasad *et al.*, 2017).

Chitosan, a naturally occurring biopolymer is extracted by diacylation of the chitin (major insect exoskeleton component), it is biocompatible, biodegradable, non-toxic and antibacterial thus making it considerably significant in various biomedical applications (Anitha *et al.*, no date), it is a material of interest in electrodeposition because of its high charge density enabling it to adsorb a variety of other charged materials and facilitate their electrophoretic deposition (Sarkar and Nicholson, 1996).

Halloysites (HNTs) is an aluminosilicate composite comprised of rolled-up sheets of silica and alumina leading to opposite charges between the outer and the inner core; it has significant potential as a drug carrier as its hollow core can be loaded with materials of choice that can be released sustainably over time (M. Massaro *et al.*, 2017). Thus, biocompatible composites with sustained drug release capability can be created by blending chitosan with drug loaded HNTs.

Previous studies have shown electrodeposition of drug loaded HNTs-chitosan coatings on titanium surface under different alcohol solutions (Farrokhi-Rad and Ghorbani, 2011), different pH (Radda'a *et al.*, 2017), using bioglass (Radda'a *et al.*, 2017), and zinc halloysite substituted hydroxyapatite (Chozhanathmisra *et al.*, 2016). This study is novel as it explores the effect of using chitosan blended with zinc halloysite loaded with gentamicin drug (CS-ZnHNTs-GS) in EPD of titanium and synergistic activity of drug and metal ions in preventing the formation of a biofilm and correlated it with ion release profile.

6.2 Materials and Methods

6.2.1 Materials

Chitosan (CS, MW = 200,000) with a deacetylation degree of 85%, HNTs, ethanol, acetic acid, acetone, phosphate-buffered saline (PBS), silicon carbide sandpaper, ninhydrin, gentamicin sulfate (GS), zinc sulphate heptahydrate ($ZnSO_4 \cdot 7H_2O$), titanium foil (Ti, 99.7% trace metals basis), o-phthalaldehyde, β -mercaptopyethanol, isopropyl alcohol, ethanol, sodium borate were purchased from Sigma-Aldrich (St. Louis, MO). Platinum mesh electrodes and VWR Accupower 500 electrophoresis power supply and ammeter (TekPower TP9605BT) from was purchased from Amazon LLC (Seattle, WA).

6.2.2 Methods

mHNTs were prepared using a modified protocol based on an electrolytic method previously described by Mills et al. (Mills and Boyer, 2018). Briefly, an electrolysis setup was assembled consisting of two platinized titanium mesh held parallel at a 2-inch distance and connected to a DC power source (VWR Accupower 500 electrophoresis power supply). Ultrasonicated 100 mL aqueous solution of metal salts (2.5 mM) and 50 mg HNTs were dispersed in glass beaker, and 20 V was maintained at 80° C with polarity reversal at every 5 min (Khaydarov *et al.*, 2009) under constant stirring to reduce electrophoretic buildup at the working electrode and thus increase ion density in the solution, afterward the supernatant was decanted thrice, and the solution was centrifuged at 5000 rpm for 5 min with water to separate mHNTs from un-adsorbed metal particles and dried at 30° C.

Vacuum loading techniques were employed to load gentamicin sulfate (GS) drug into the ZnHNTs lumen, briefly 25 mg of GS was dispersed in 5 mL PBS, mixed with 100 mg ZnHNTs and placed under vacuum (28 pounds/inch²) overnight, the resulting product was decanted and washed, this process was repeated thrice to ensure the removal of non-lumen gentamicin.

Titanium foil was cut into 1x3 cm dimensions, grounded with silicon carbide paper, washed with acetone and distilled water successively in order to remove surface oil and treated with 4 N NaOH for 10 min to increase the hydrophilicity of the surface, excess NaOH was wiped off and the foil was rinsed in distilled water and dried at 30° C.

0.1 g solution of chitosan in 100 mL 3:1 distilled water: ethanol (Radda'a *et al.*, 2017) was prepared, and 1 mL of acetic acid was added in order to reduce the pH of the

liquid necessary for the protonation of chitosan and 10 wt.% (0.01 g) ZnHNTs-GS were added and the solution was covered to prevent evaporation and magnetically stirred for 30 min to ensure ZnHNTs adsorption to chitosan.

Electrophoretic deposition was performed by using a platinum mesh electrode (5x7.5 cm) and titanium foil (1x3 cm) held 1 inch apart connected to a 40 V DC power supply (VWR Accupower 500) functioning as anode and cathode respectively with a desktop ammeter (TekPower TP9605BT) connected in series, immersed into the solution and the electrophoresis was carried out for 10 min under room temperature (**Figure 6-1**). Samples were air-dried and before and after weights were recorded.

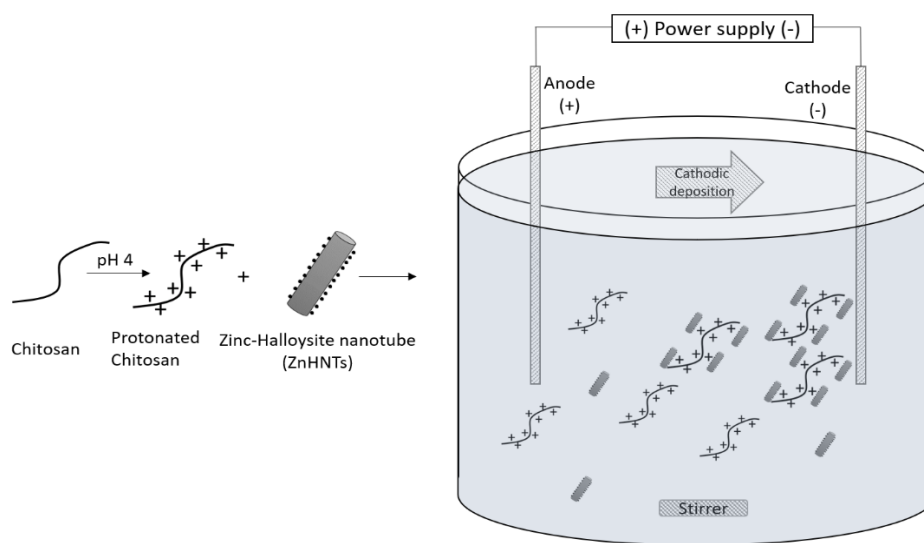


Figure 6-1: Graphical overview of the electrophoretic deposition process.

Drug release quantity over time was estimated by a method described previously (Ismail *et al.*, 2016). Briefly, Ti samples were placed in 1 mL PBS, placed in shaker and 1 mL of sample was collected at regular time intervals and 1 mL PBS was replenished each time, 1 mL of collected PBS was mixed with OPTA reagent (1 mL) and isopropyl alcohol (1 mL) and allowed to react for 30 min at room temperature and absorbance was

measured at 335 nm. OPTA reagent was prepared by mixing 2.5 g o-phthalaldehyde, 3 mL β -mercaptoethanol, 62.5 mL isopropanol, and 560 mL of 0.04 g sodium borate. PBS was used as the blank, and measured quantities of drugs were used to draw standard graphs (Weisman *et al.*, 2017).

The antibacterial potential was evaluated against *S. aureus* using a microdilution broth assay. Briefly, 1x1cm samples were cut and immersed in 24 well plates containing 3 mL/well Muller Hinton broth inoculated with 20 μ L of 0.5 McFarland standard *S. aureus*, the plates were put on a shaker, after 4 hr the samples were removed, and the absorbance of 100 μ L solution was recorded after 12 hr.

Biofilm assay was performed using the crystal violet assay, briefly, samples were incubated in 2 mL nutrient broth in 48 well plates inoculated with 1 McFarland *S. aureus* for 2 days at 37° C, at the end of which the plate was emptied by inverting and gently tapping in order to remove lightly attached planktonic bacteria and the remaining bacterial films were stained with aqueous crystal violet (0.1 w/v%) for 10 min, which was similarly removed by inversion and tapping to ensure optimal removal of unattached bacteria, acetic acid (30%) was added to each well to solubilize the stain and absorbance at 630 nm was recorded (O'Toole, 2011). Crystal violet is a basic dye that binds non-specifically to negatively charged surface molecules including polysaccharide in the extracellular matrix (Silva *et al.*, 2009).

The additional antibiotic potential was measured by studying the inhibition zones on Mueller-Hinton agar plates.

Preosteoblasts cells were cultured, live/dead, and proliferation tests were performed on 1x1 cm samples as described in the former Chapter.

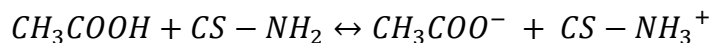
In vitro bioactivity was assessed out using 5x simulated body fluid (SBF) prepared using a modified protocol (Barrere *et al.*, 2002) based on Kokubo *et. al* (Kokubo and Takadama, 2006). The samples were immersed in 3 mL of 5x SBF at 37° C for 1, 3, 6 days, after immersion, the samples were taken out and dried at room temperature. SEM-EDS was performed on the samples for analyzing the formation of hydroxyapatite (HA).

6.2.3 Characterization

The resulting CS-ZnHNTs-GS coatings were characterized using scanning electron microscope and elemental analysis by energy-dispersive X-ray spectroscopy (SEM-EDS, HITACHI S-4800), ion release by X-ray fluorescence (XRF, ARL Quant'X, Thermo Scientific), chemical analysis by Fourier-transform infrared spectroscopy (FTIR, Nicolet 6700, Thermo Scientific), UV-Vis absorbance (NanoDrop 2000c spectrophotometer, Thermo Scientific), and 3-dimensional morphology by confocal microscopy (VK-X200, Keyence).

6.3 Results and Discussion

GS adsorbs to the outer surface of the ZnHNTs consisting of Si-O-Si negatively charged bonds, whereas application of vacuum creates a negative pressure inside the ZnHNTs lumen and leads to loading of the drug. Chitosan is necessary for the EPD of ZnHNTs-GS as it not only stabilizes the suspension but also provides the required net positive charge for deposition on the negatively charged cathode. Chitosan dissolves by a protonation by acetic acid resulting in pH reduction, increased conductivity, and adsorbs ZnHNTs.



At the cathode electrolysis of water occurs generating hydroxyl ion (OH^-) which deprotonates the CS-NH_3^+ resulting in CS-NH_2 (Zhitomirsky, 1997; Pang and Zhitomirsky, 2007; Farrokhi-Rad, Fateh and Shahrabi, 2018).

Samples were examined using laser confocal microscopy, and a layer of the coatings was observed on the Ti implants (**Figure 6-2**).

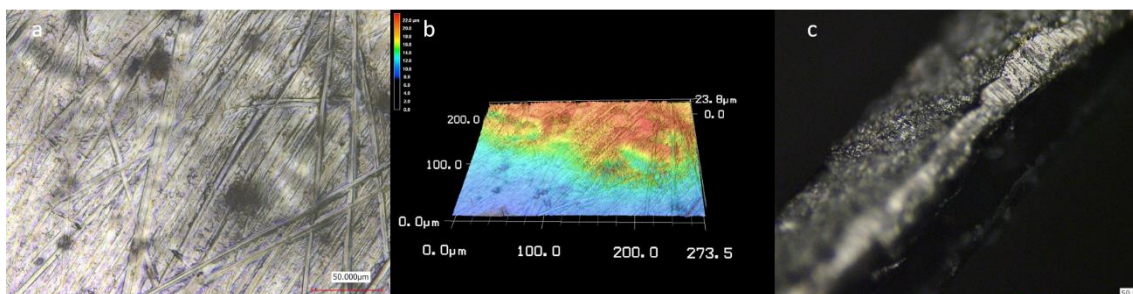


Figure 6-2: (a, c) Laser confocal image of CS-ZnHNTs-GS coating, (b) 3D topography of the implant.

SEM micrograph is shown in **Figure 6-3**, a uniform layer of chitosan is observed on all the samples, titanium samples with ZnHNTs exhibit cylindrical structures on the surface indicative of the presence of the nanotubes.

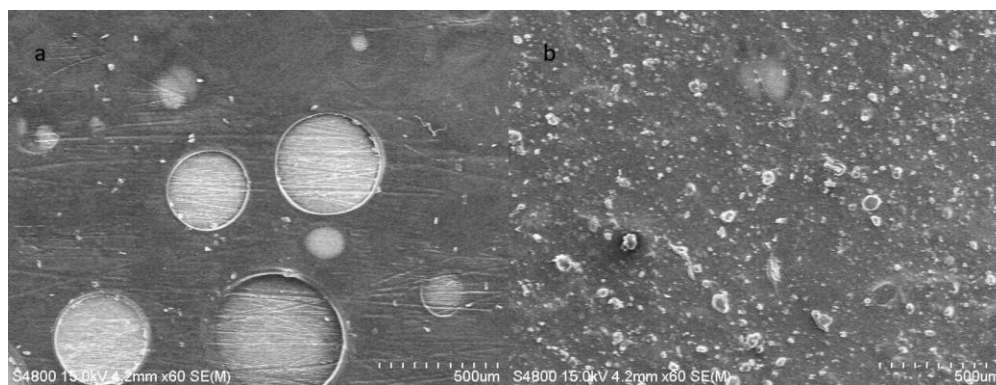


Figure 6-3: SEM micrograph of (a) Chitosan (b) CS-ZnHNTs-GS deposits, respectively. Smooth morphology of chitosan is disturbed on the addition of mHNTs which appear almost uniformly distributed on chitosan.

Figure 6-4 elemental mapping results confirm the presence of uniformly interspersed ZnHNTs interspersed throughout the coatings.

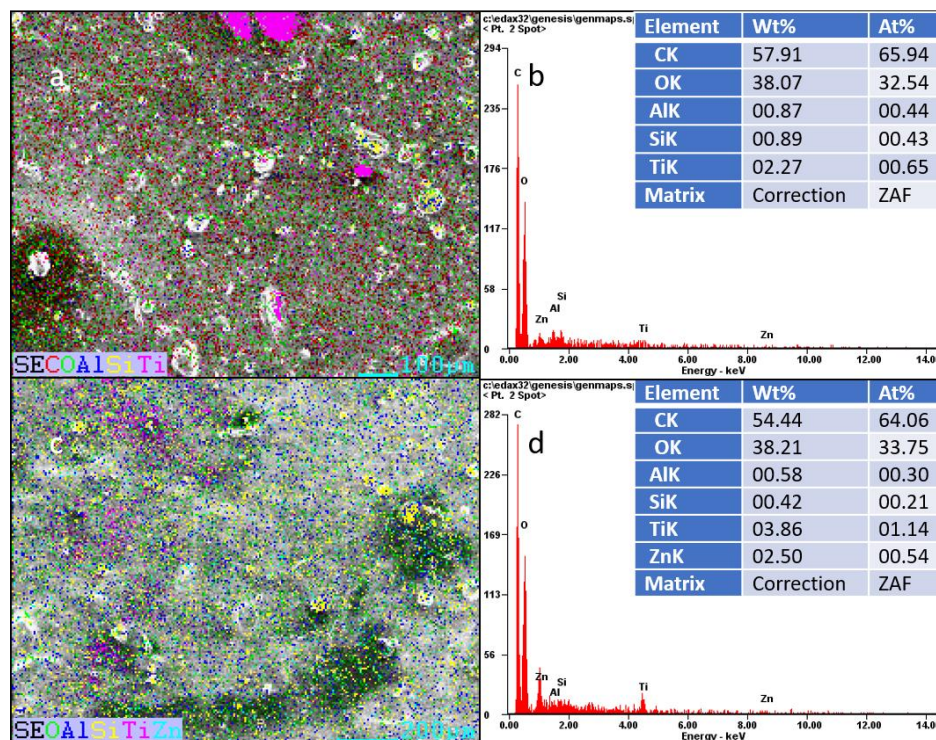


Figure 6-4: EDS Mapping of (a, b) CS-HNTs and (c, d) CS-ZnHNTs, a more uniform surface with less titanium base metal visibility is obtained which could be due to increased conductance of the electrophoretic deposition on the addition of ZnHNTs.

FTIR was used for chemical analysis and characteristic bands for chitosan at 3400 (O-H stretch) and 2940 cm^{-1} (C-H stretch) respectively, and peaks for the secondary amide group bending were observed at 1644 cm^{-1} . On the addition of ZnHNTs, new peaks were observed at 1031 and 1090 cm^{-1} respectively which correspond to in-plane Si-O stretching of HNTs, new peaks at 1278 and 1401 cm^{-1} respectively can be ascribed to C-N stretching of gentamicin (Rapacz-Kmita *et al.*, 2015) (**Figure 6-5**).

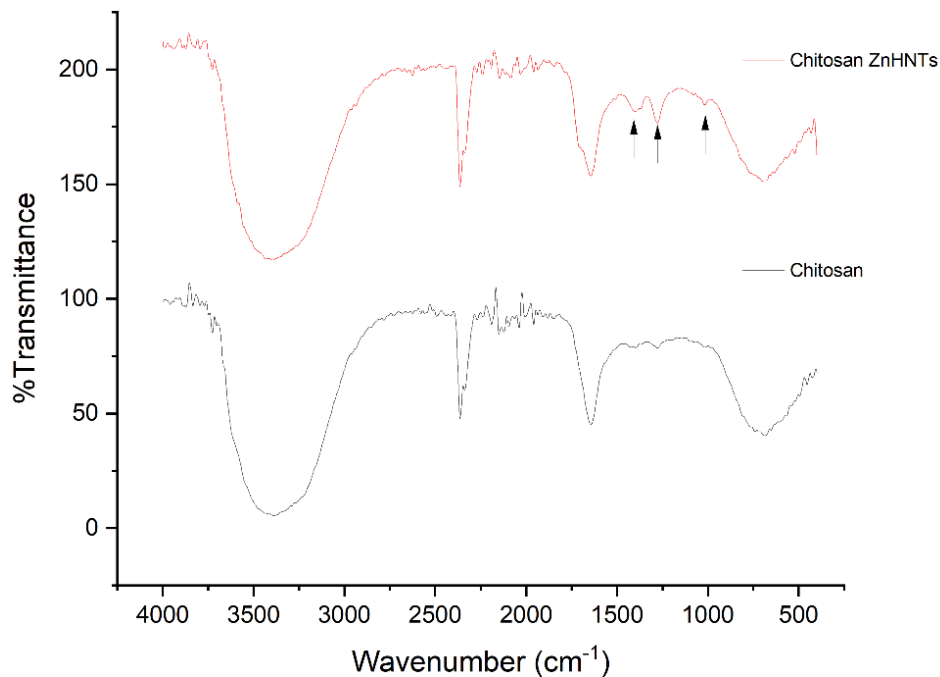


Figure 6-5: FTIR spectra of the coatings. Arrow depicts the new peaks observed on the addition of ZnHNTs-GS at 1028 (in-plane Si-O stretching of HNTs), 1278 and 1401 cm^{-1} corresponding to C-N stretching of gentamicin respectively.

Figure 6-6 shows the current density for the EPD at 40 V; it remained almost constant during the process. Further, the addition of acetic acid helped in chitosan protonation and increased the current density of the EPD system, the addition of ZnHNTs resulted in slightly elevated amperage.

Biofouling of implants is the leading cause of implant failure, and the present study was aimed at developing a biomaterial possessing an anti-biofouling capability. Antibacterial potential of the samples was evaluated against gram-positive *S. aureus* bacteria (most common culprit in clinical biofouling) using agar diffusion method and CS-ZnHNTs-GS exhibited significant inhibition zones of $3.11 \pm 0.79 \text{ cm}^2/\text{unit area}$ of the sample (**Figure 6-7**), and also exhibited less planktonic bacteria (**Figure 6-8**), and reduced biofilm formation (**Figure 6-9**).

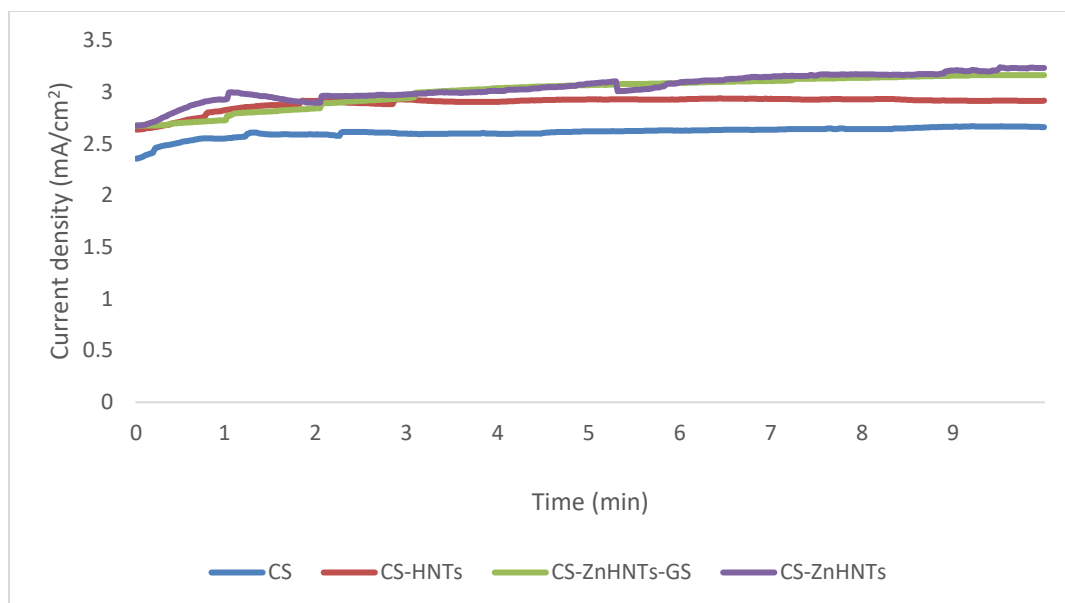


Figure 6-6: Current density during EPD at 40 V. The addition of ZnHNTs in the chitosan leads to increased current density, explainable based on increased conductivity due to ionic species leaching from ZnHNTs.

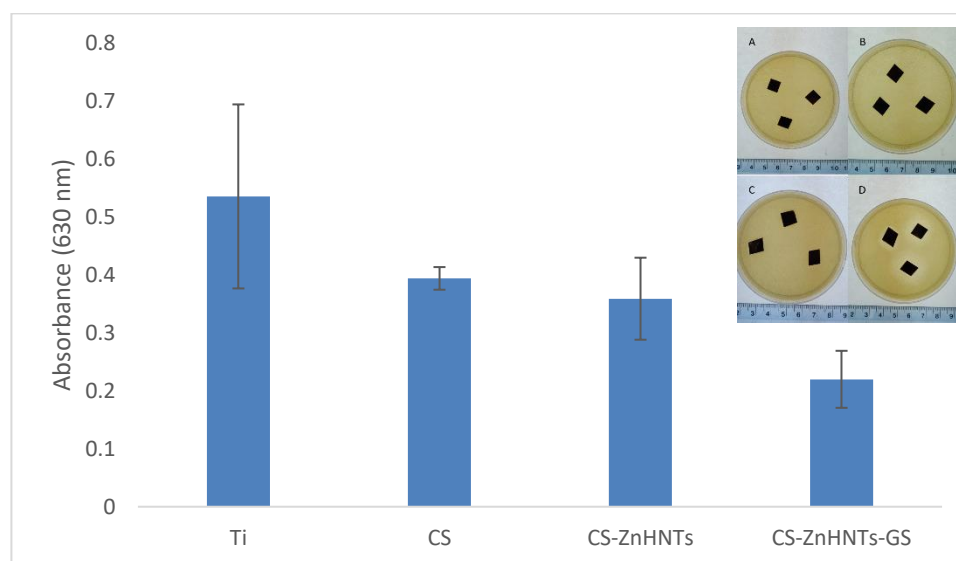


Figure 6-7: Antimicrobial broth testing, GS-ZnHNTs-CS exhibited the highest bacteriostatic effect. (Inset shows agar diffusion assay of (a) Uncoated titanium, (b) CS, (c) CS-ZnHNTs, and (d) CS-ZnHNTs-GS.

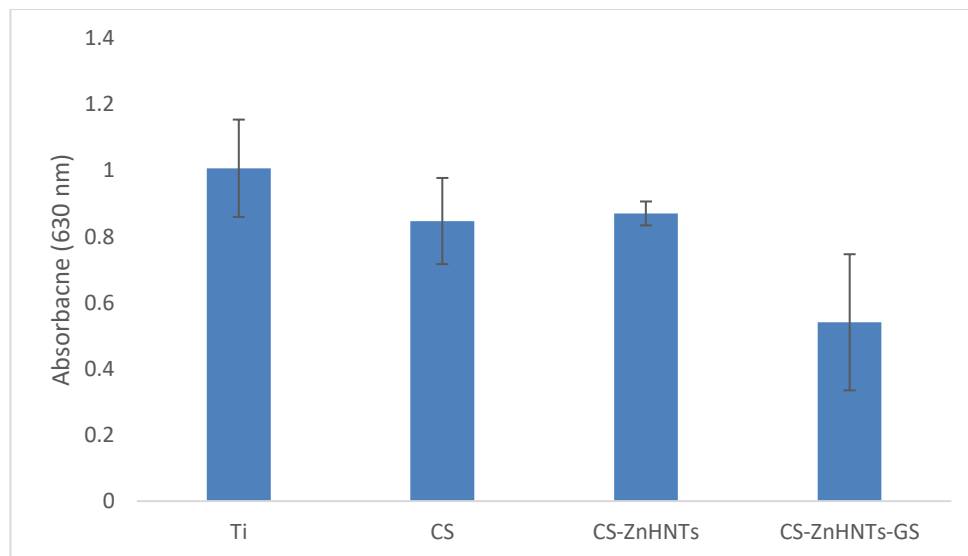


Figure 6-8: Planktonic growth of *S. aureus* on the surface of the samples.

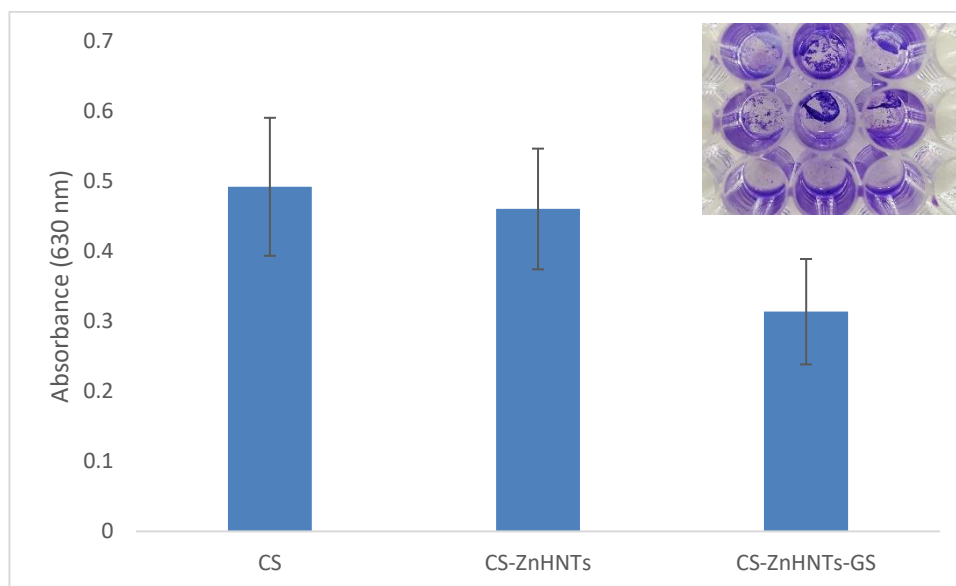


Figure 6-9: Biofilm assay using crystal violet, similar but diminished trend as compared to broth testing was obtained. Inset depicts the crystal violet stained biofilm in CS, CS-ZnHNTs, CS-ZnHNTs-GS wells (top-bottom respectively).

Furthermore, the samples on staining with crystal violet displayed less biofilm formation on the implant surface on the incorporation of ZnHNTs-GS (**Figure 6-10**), which can be attributed to zinc ions leaching from the coatings (**Figure 6-11**) and

gentamicin release from HNTs lumen (**Figure 6-12**).

Additionally, the total GS content on the surface of the implant coatings was estimated by dipping the samples into ninhydrin reagent (2.12 ± 0.81 mg/mL was obtained, $n=5$).

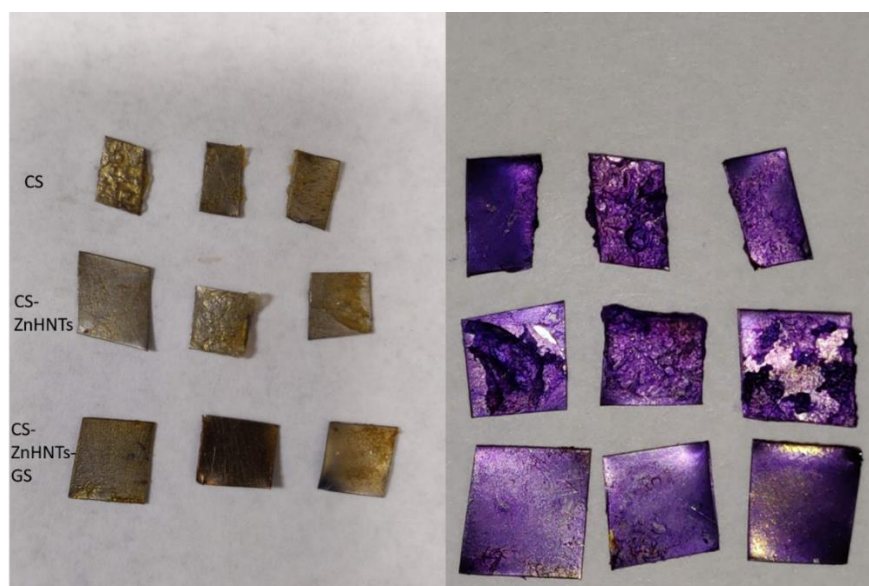


Figure 6-10: Crystal violet dye stained samples. Least biofilm formation was visually observed on CS-ZnHNTs-GS samples.

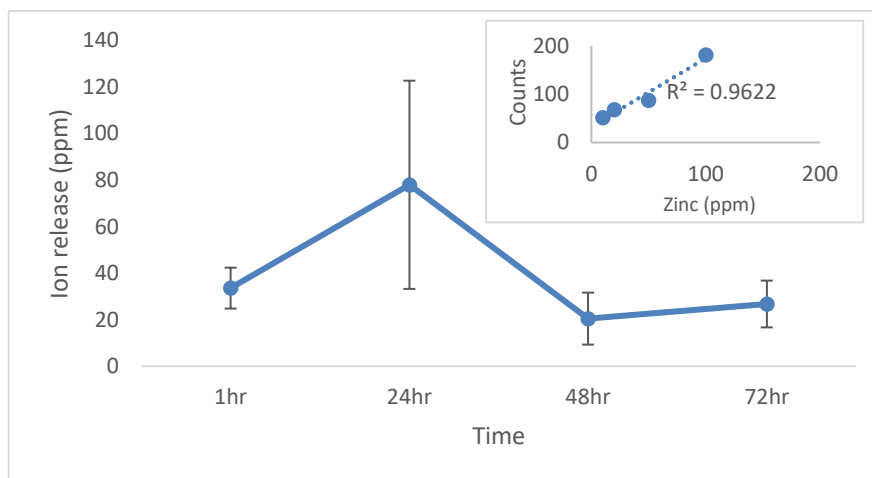


Figure 6-11: Zinc ion release from the CS-ZnHNTs-GS coatings, highest ion release concentration was observed at 24 hr, ($n=5$), (Inset – zinc ion standard XRF curve).

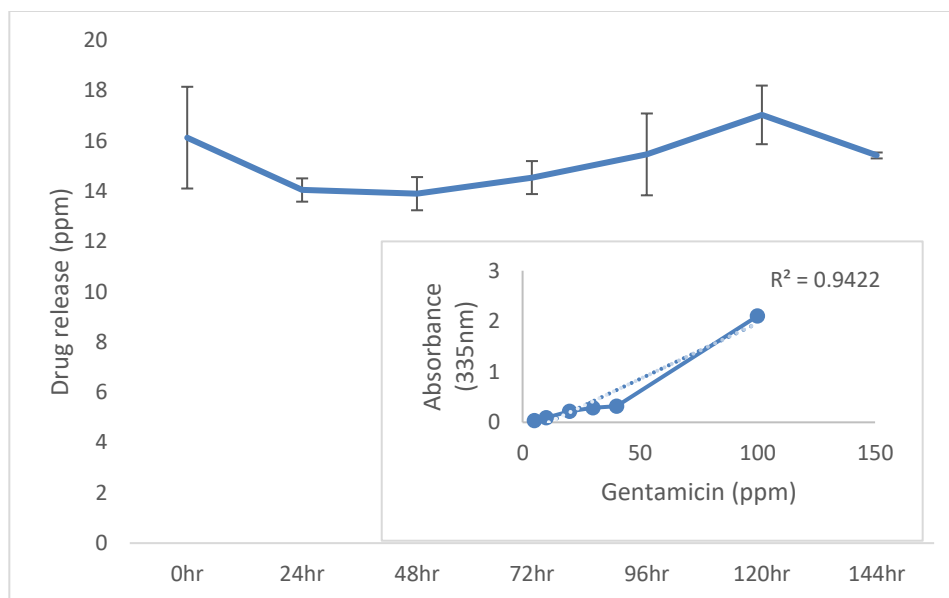


Figure 6-12: Gentamicin release from CS-ZnHNTs-GS coatings (ppm). A continuous burst of drug release was observed, which could be due to drug adsorbed on mHNTs outer surface and chitosan coating. (Inset – gentamicin standard XRF curve), (n=5).

Figure 6-13 shows cell viability analysis, the addition of ZnHNTs led to increased cellular viability which could be due to the release of Zn^{+} ions and their cellular uptake where they participate as cofactors and precursors of different enzymes.

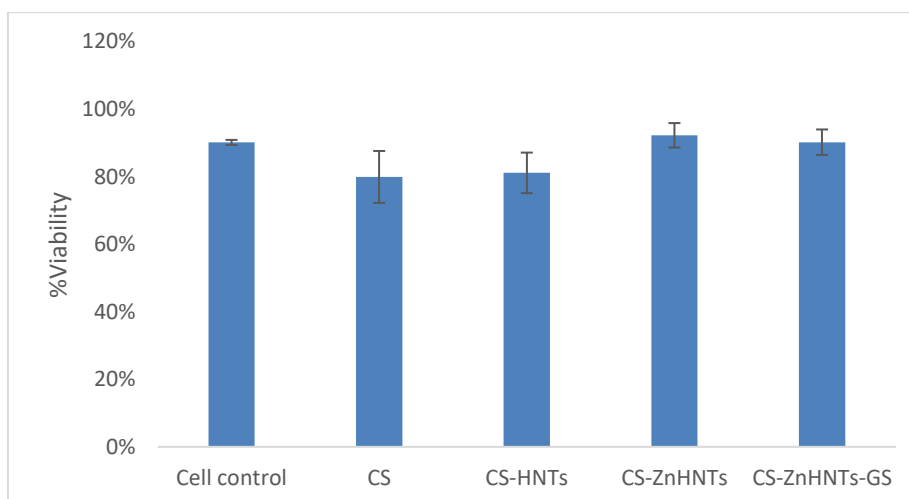


Figure 6-13: Cell viability assay for electrodeposited Ti.

Figure 6-14 shows the cell live/dead assay, the addition of ZnHNTs led to lesser number of dead cells when compared to the other samples, **Figure 6-15** shows the proliferation assay. Similar findings have been reported previously in the literature, where the addition of Zn led to an increased bone marrow stem cell proliferation (Hu *et al.*, 2012), a similar study showed that Zn led to increased antimicrobial and osteogenic activity (Jin *et al.*, 2014), and another study found similar results with incorporation Zn with magnesium ions (Yu *et al.*, 2017).

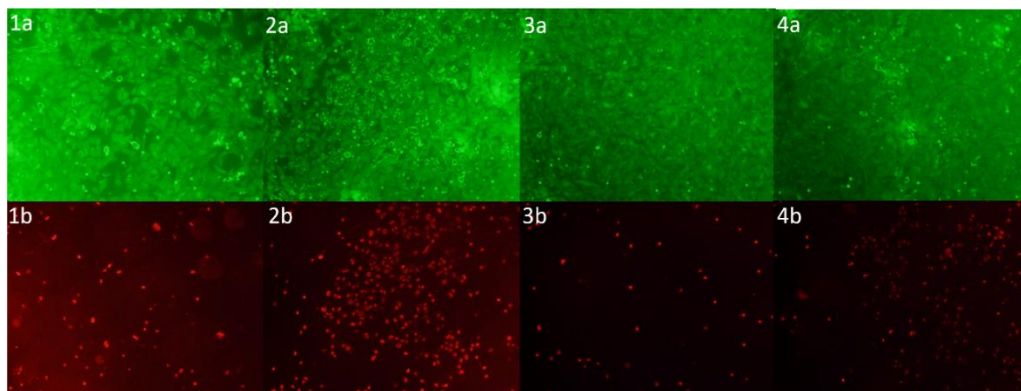


Figure 6-14: Live/Dead assay, preosteoblast cells were cultured in the presence of Ti implants (1a, 1b) CS, (2a, 2b) HNTs-CS, (3a, 3b) ZnHNTs-CS, and (4a, 4b) GS-ZnHNTs-CS. Live cells (green) and dead cells (red).

The data shows that the CS-ZnHNTs-GS coatings possess significant anti-biofouling activity which can be attributed to the gentamicin antibiotic, additionally the release of zinc ions, as well as the positively charged chitosan surface, might have led to increased interactions with negatively charged bacterial membrane and resulted in supplementary enhancement of the anti-biofouling effect, further, increased cellular proliferation and viability were observed with the incorporation of ZnHNTs.

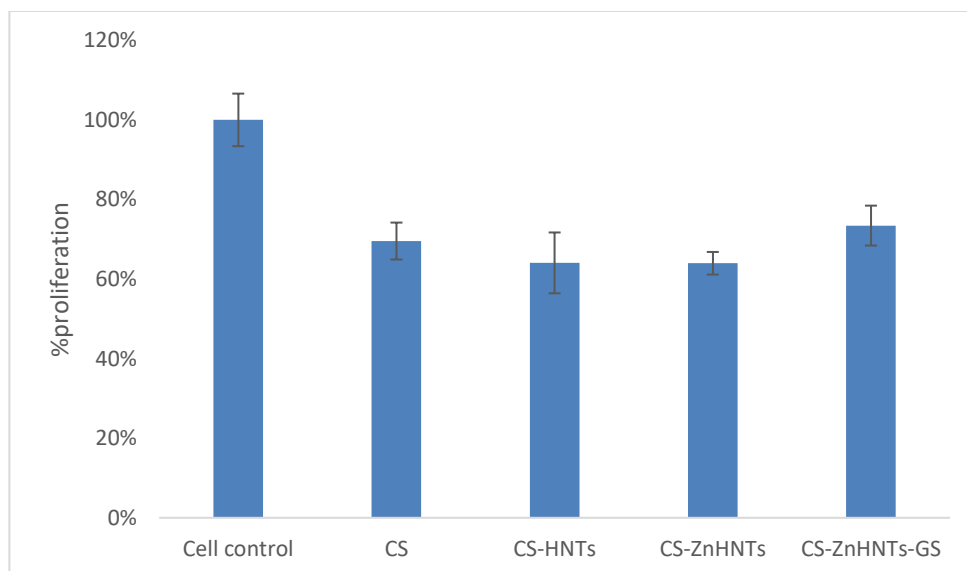


Figure 6-15: Proliferation assay for the Ti implants, CS-ZnHNTs-GS were found to be the most viable for cell proliferation.

Figure 6-16 shows the hydroxyapatite formation on the samples when dipped in SBF; hydroxyapatite formation is indicative of the bone integration potential of a material.

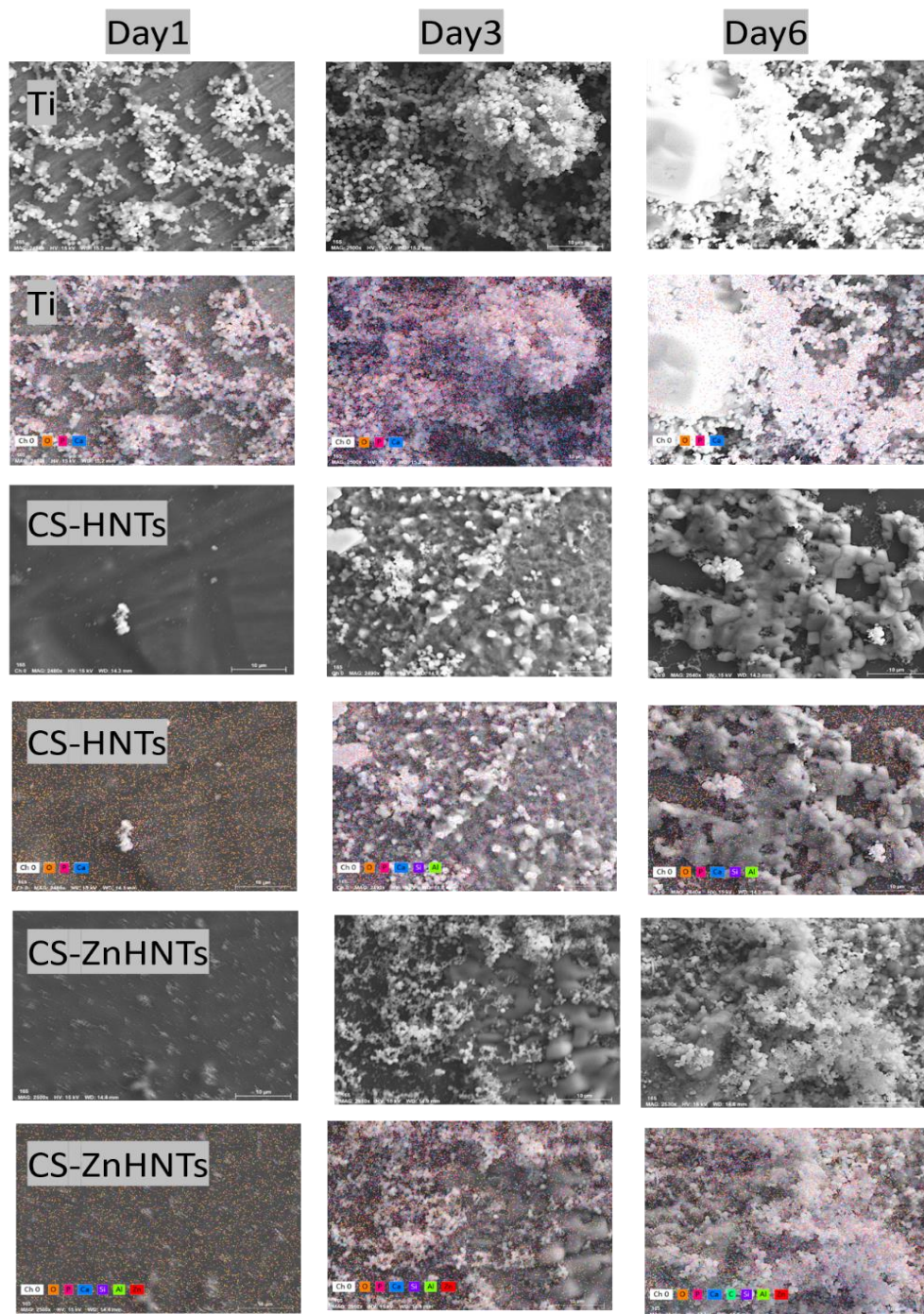


Figure 6-16: SEM-EDS map of the samples soaked in SBF.

6.4 Conclusion

EPD technique was used to deposit CS-ZnHNTs-GS coatings on titanium. Morphological surface characterization using SEM-EDS and EDS mapping confirmed the presence of tubular ZnHNTs structure embedded in the coatings and FTIR analysis confirmed the presence of CS-ZnHNTs-GS in the coatings. The antibacterial evaluation confirmed the anti-biofouling potential of the coatings. Thus, we demonstrate the successful development and evaluation of an anti-biofouling coating for titanium implants.

CHAPTER 7

GENTAMICIN LOADED ZNHNTS-CHITOSAN ANTIMICROBIAL COATINGS FOR MEDICAL DEVICES

7.1 Introduction

Biofilm is a collection of bacteria attached to a surface as opposed to the unattached planktonic form, biofouling, the result of a biofilm formation is the collection of the bacterial organic waste material, it has adverse effects in clinical settings resulting in failure of implants, medical surfaces, and its elimination is a vital research focus as its matrix helps in promoting rapid bacterial growth, resists antibiotics, dehydration and other stresses and provides an optimal growth environment for the prokaryotes (Lyon *et al.*, 2008; Ribeiro, Monteiro and Ferraz, 2012).

It is estimated that biofouling of meshes can lead to up to 1-2% infection incidences (Engelsman *et al.*, 2007), postoperative antibiotic administration is a common strategy; however, it can be limited due to low efficiency and cost. Thus, it is vital in biomedical research to develop preoperative processes and materials that can prevent the growth of bacteria. It is a common strategy to integrate anti-biofouling compounds into medical devices, however, once bacteria have attached to the surface and died, the dead bacterial cell layer function as an attachment layer for the next layer of bacteria, thus acting as a shield barrier and diminishing the effect of the antimicrobials, an alternate

strategy would be to develop an anti-biofouling coating having a controlled release of antimicrobial substances that can be sprayed on medical devices.

Chitosan, a naturally occurring biopolymer is extracted by the diacylation of the chitin (a significant component of the insect exoskeleton), biocompatible, biodegradable, non-toxic and antibacterial thus, making it of significance in various biomedical applications (Anitha *et al.*, 2015).

Halloysites nanotubes (HNTs) is an aluminosilicate composite comprising of rolled-up sheets of silica and alumina leading to opposite charge between outer and inner core, and it has significant potential as a drug carrier as its hollow core can be loaded with a material of choice which can be released sustainably over time (M. Massaro *et al.*, 2017). Potentially biocompatible composites with sustained drug release capability can be created by blending chitosan with drug loaded HNTs.

Previous studies have explored antimicrobial films composed of HNTs with superhydrophobic polysiloxane (Feng *et al.*, 2018), HNTs loaded with carvacrol for food packaging (Tas *et al.*, 2019), and surface salinization for extensive hydrophobicity (Dong and Zhang, 2018).

Here, we report a method for preparing antimicrobial coatings made of CS-ZnHNTs-GS having sustained antimicrobial activity that can be readily air sprayed on different surfaces. Different concentrations of the ZnHNTs-GS in chitosan were studied, surface coatings were characterized using SEM-EDS, EDS-map, ED-XRF, and FTIR. The antimicrobial potential was studied using disc diffusion and biofilm assay, respectively.

7.2 Materials and Methods

7.2.1 Materials

Chitosan (CS, Mw = 200,000) with a deacetylation degree of 85%, HNTs, ethanol, phosphate-buffered saline (PBS), gentamicin sulfate (GS), zinc sulphate heptahydrate ($ZnSO_4 \cdot 7H_2O$), Mueller-Hinton agar, petri dish, Whatman filter paper no 1 were purchased from Sigma-Aldrich (St. Louis, MO), F2C TC-802K airbrush kit was purchased from Amazon (Seattle, WA).

7.2.2 Methods

mHNTs were prepared using a modified protocol based on an electrolytic method previously described by Mills et al. (Mills and Boyer, 2018); An electrolysis setup was assembled consisting of two platinized titanium mesh held parallel at a 2 inch distance and connected to a DC power source (VWR Accupower 500 electrophoresis power supply). Ultrasonicated 100 mL aqueous solution of metal salts (2.5 mM) and 50 mg HNTs were dispersed in glass beaker, and 20 V was maintained at 80° C with polarity reversal at every 5 min (Khaydarov *et al.*, 2009) under constant stirring to reduce electrophoretic buildup at the working electrode and thus increase ion density in the solution, afterward the supernatant was decanted thrice, and the solution was centrifuged at 5000 rpm for 5 min with water to separate mHNTs from un-adsorbed metal particles and dried at 30° C.

Vacuum loading techniques were employed to load gentamicin sulfate (GS) drug into the ZnHNTs lumen, briefly 25 mg of GS was dispersed in 5 mL PBS, mixed with 100 mg ZnHNTs and placed under vacuum (28 pounds/square inch) overnight, the

resulting product was decanted and washed, this process was repeated thrice to ensure removal of any unloaded gentamicin.

Chitosan 0.1 g in 50 mL ethanol was prepared by adding 0.05 mL of acetic acid in order to reduce the pH of the solution necessary for the protonation of chitosan and 1, 2.5, and 5 w/v% ZnHNTs-GS were added, and the solution was magnetically stirred for 30 min.

CS-ZnHNTs-GS suspended in ethanolic solution with ZnHNTs-GS at 1, 2.5, and 5 w/v% were air sprayed on 6 mm discs (Whatman filter paper no 1) using air spray operating at 1.0 mm nozzle diameter and 0.29 MPa spraying air pressure at a flow rate of 3 mL/s and 15 cm spray distance for 5 s. The resulting surfaces were air-dried and stored until usage.

Drug release was estimated by a method described previously (Ismail *et al.*, 2016), briefly, thus prepared antimicrobial discs were immersed in 1 mL PBS, placed in shaker and 1mL of sample was collected at regular time intervals and new 1 mL PBS was replaced each time, 1 mL of collected PBS was mixed with OPTA reagent (1 mL) and isopropyl alcohol (1 mL) and allowed to react for 30 min at room temperature and absorbance was measured at 335 nm. OPTA reagent was prepared by mixing 2.5 g o-phthaldialdehyde, 3 mL β -mercaptopethanol, 62.5 mL isopropanol, and 560 mL of 0.04 g sodium borate. PBS was used as the blank, and measured quantities of gentamicin were used to draw standard graphs (Weisman *et al.*, 2017).

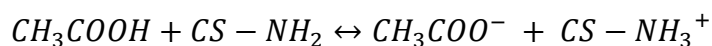
7.2.3 Characterization

The resulting CS-ZnHNTs-GS coatings were characterized using scanning electron microscope and elemental analysis by energy-dispersive X-ray spectroscopy

(SEM-EDS, HITACHI S-4800), X-ray fluorescence (XRF, ARL™ Quant'X, Thermo Scientific), UV-Vis absorbance (NanoDrop 2000c spectrophotometer, Thermo scientific), Fourier-transform infrared spectroscopy (FTIR, Nicolet 6700, Thermo Scientific) and confocal microscopy (VK-X200, Keyence).

7.3 Results and Discussion

GS adsorbs to the outer surface of the ZnHNTs consisting of Si-O-Si negatively charged bonds, whereas application of vacuum creates a negative pressure inside the ZnHNTs lumen and leads to loading of the drug. Chitosan is necessary because it stabilizes the suspension and helps in facilitating adherence to a different surface. Chitosan dissolves by a protonation by acetic acid resulting in pH reduction and increased conductivity and adsorbs ZnHNTs.



CS-NH₃⁺ adsorbs the ZnHNTs-GS and functions as a support suspension.

SEM micrograph is shown in **Figure 7-1**, a uniform layer of chitosan is observed for all the samples, ZnHNTs exhibit cylindrical structures on the surface indicative of the presence of the nanotubes, elemental mapping results confirm uniformly interspersed ZnHNTs on the coatings.

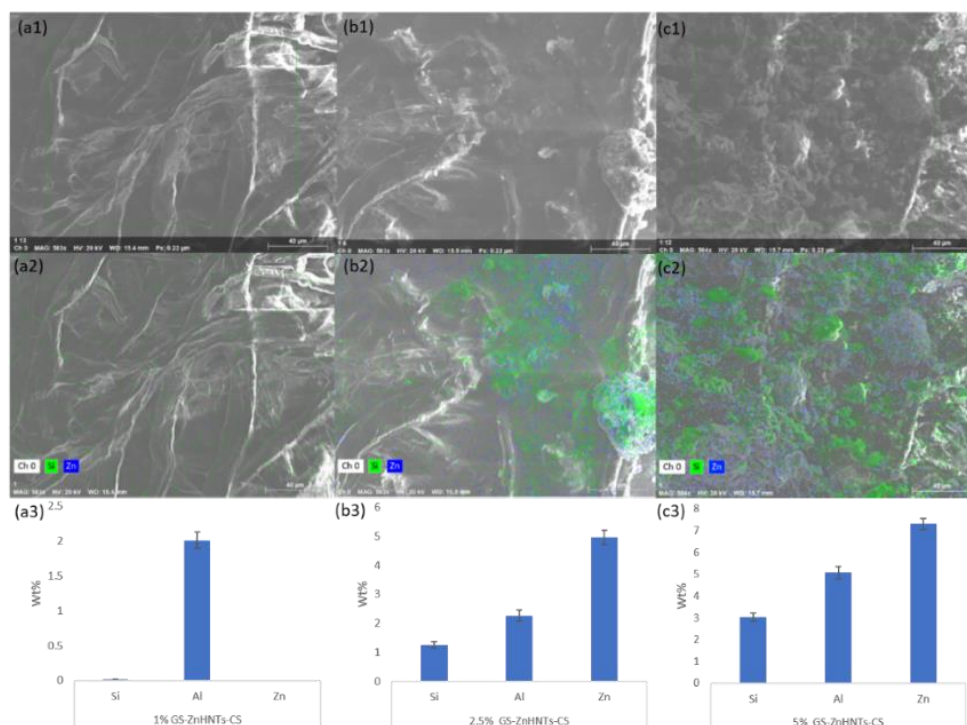


Figure 7-1: SEM, EDS map, and EDS of (a1, a2, a3) CS-1% ZnHNTs-GS, (b1, b2, b3) CS-2.5% ZnHNTs-GS, and (c1, c2, c3) CS-5% ZnHNTs-GS respectively.

FTIR was used for chemical analysis and characteristic bands for chitosan at 3300 for O-H and 2940 cm^{-1} for C-H stretch respectively, and peaks for the secondary amide group bending were observed at 1570 and 1123 cm^{-1} respectively, on addition of ZnHNTs more pronounced peaks at 1025 and 1085 cm^{-1} corresponding to in-plane Si-O stretching and perpendicular Si-O stretching respectively of HNTs were observed, peaks at 1267 and 1358 cm^{-1} can be ascribed to the C-N stretching vibrations and numerous stretching vibrations of the C-O in gentamicin drug (Rapacz-Kmita *et al.*, 2015) (**Figure 7-2**).

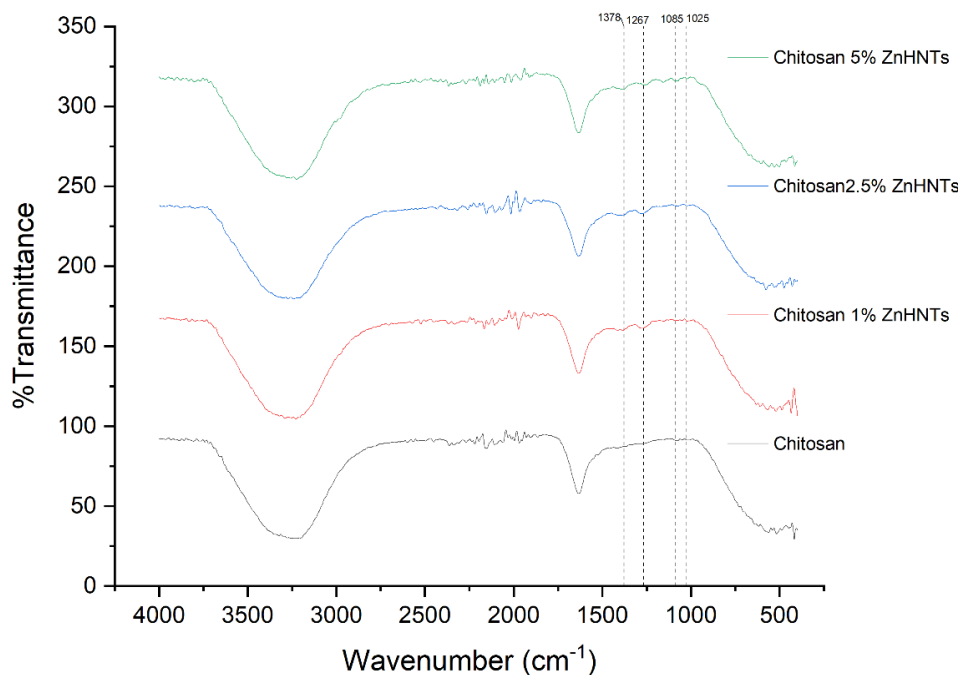


Figure 7-2: FTIR spectra of CS, CS-1, 2.5, and 5% ZnHNTs-GS films.

Biofouling of medical devices is a constant threat, and the leading cause of infections, the present study was aimed at developing an antimicrobial coating possessing the anti-biofouling capability that can be air sprayed on surfaces. Antibacterial potential of the samples was evaluated against gram-positive *S. aureus* bacteria which is the most common bacteria in clinical biofouling using agar diffusion method and the coatings exhibited substantial inhibition zones which can be attributed to the drug release as well as zinc ion release. It can be observed that the coatings possess significant antimicrobial effect which increased with the amount of ZnHNTs-GS in the coatings and average inhibition zones of 0.75, 0.83, 0.86, and 1.53 cm were observed for CS, 1, 2.5, and 5 w/v% ZnHNTs-GS coatings respectively (**Figure 7-3**), similar pattern was obtained using microtiter broth assay.

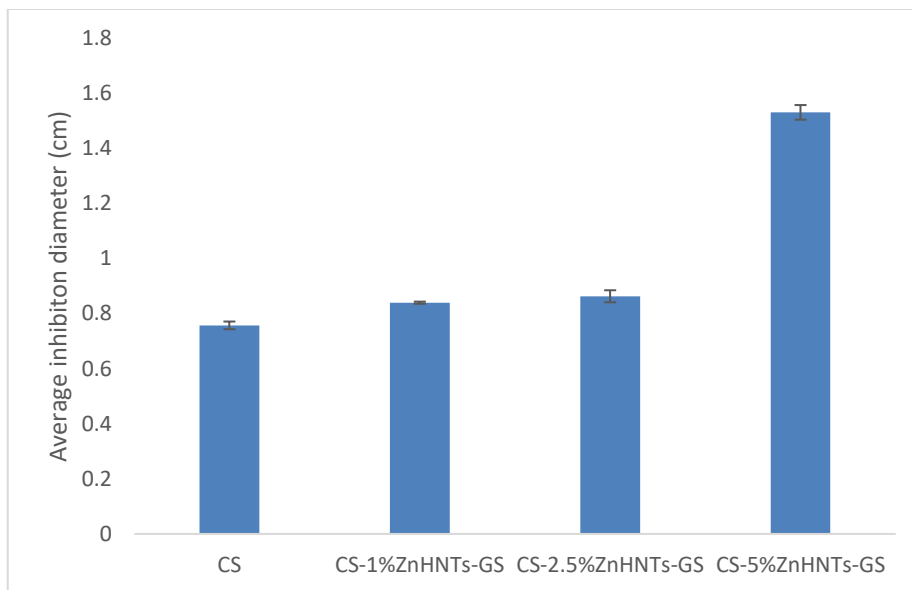


Figure 7-3: Average inhibition zones using the disk diffusion assay, increasing antibacterial activity was observed with a corresponding increase in ZnHNTs-GS wt.% in the coatings. Inset – a. CS, b. CS-1% ZnHNTs-GS, c. CS-2.5% ZnHNTs-GS, and d. CS-5% ZnHNTs-GS, respectively).

Increasing concentrations of the ZnHNTs-GS led to a decrease in bacterial growth, hence less turbidity (**Figure 7-4**).

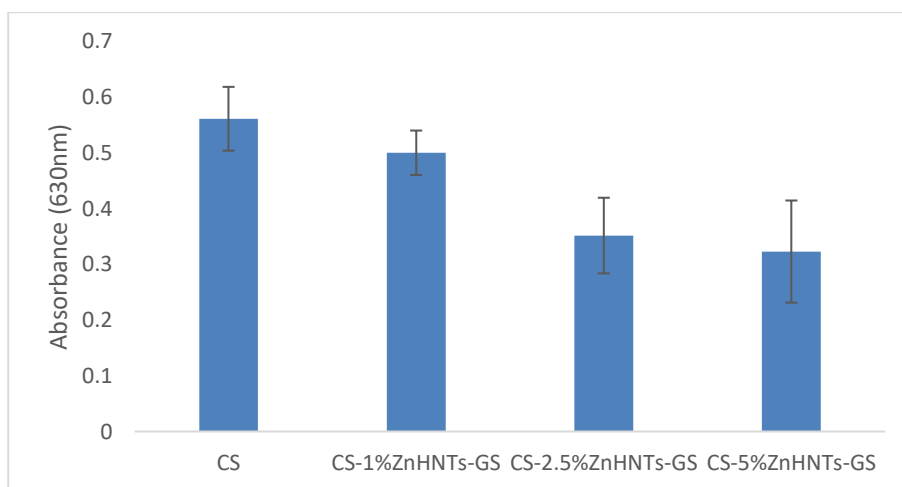


Figure 7-4: Microtiter broth assay - effect of antimicrobial coatings on the absorbance of *S. aureus*.

Similarly, less biofilm formation was observed using the crystal violet assay (**Figure 7-5**).

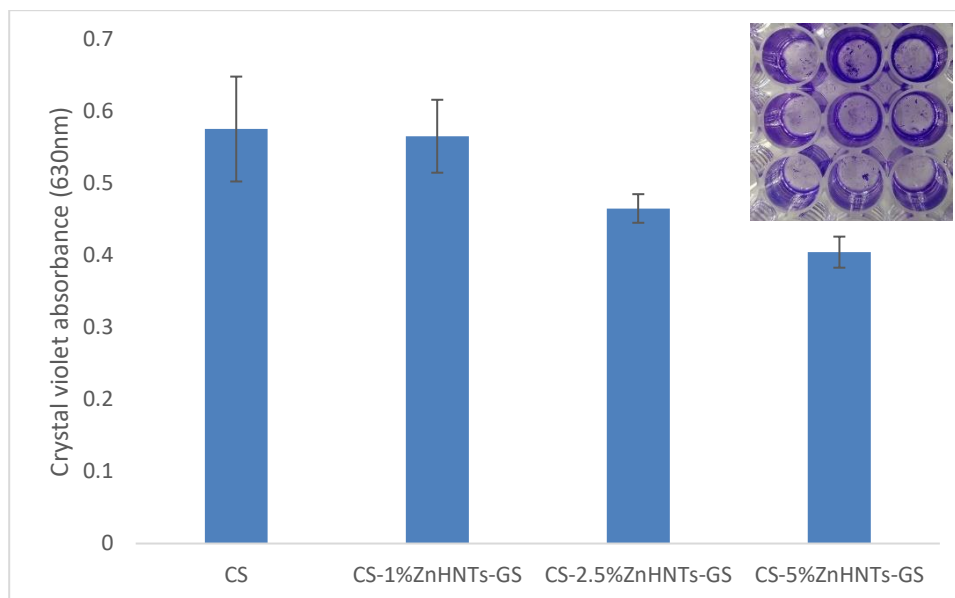


Figure 7-5: Crystal violet biofilm assay. Inset – biofilm formed on treatment with CS-1, 2.5, and 5% ZnHNTs-GS - top to bottom, respectively.

The antimicrobial effect can be attributed to gentamicin drug release from the HNTs (**Figure 7-6**) as well as the ion release (**Figure 7-7**), a gradual burst of drug release is observed at 24 hr with a reduced sustained release over time, a similar pattern of drug release has been observed in other studies (Zhang *et al.*, 2015).

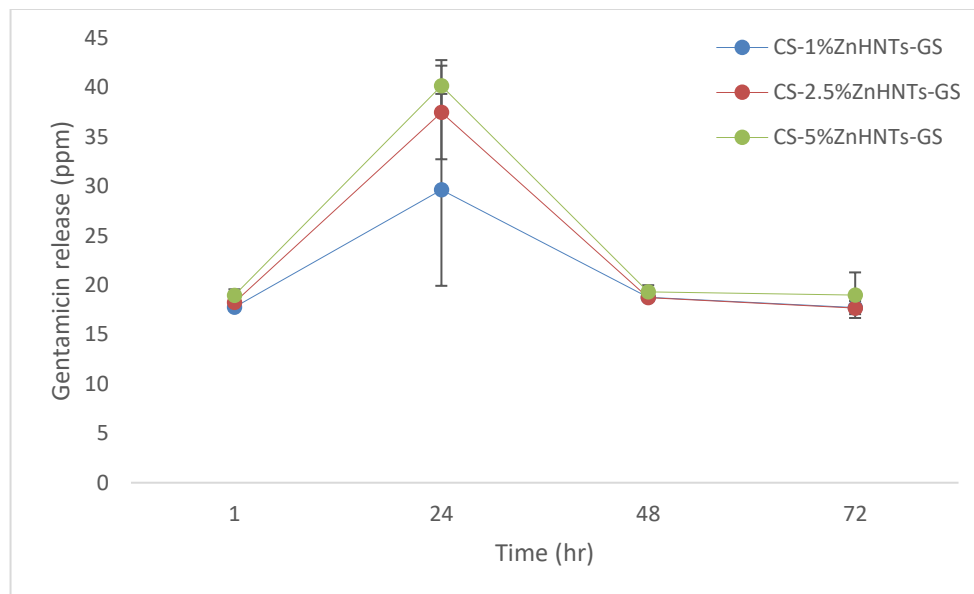


Figure 7-6: Gentamicin release from the coatings, an initial outburst of drug release is observed which could be due to the adsorbed drug on the ZnHNTs surface and in the chitosan coatings, (n=5).

Figure 7-7 shows the ion release profile, a rapid burst of ions was observed which diminished over time.

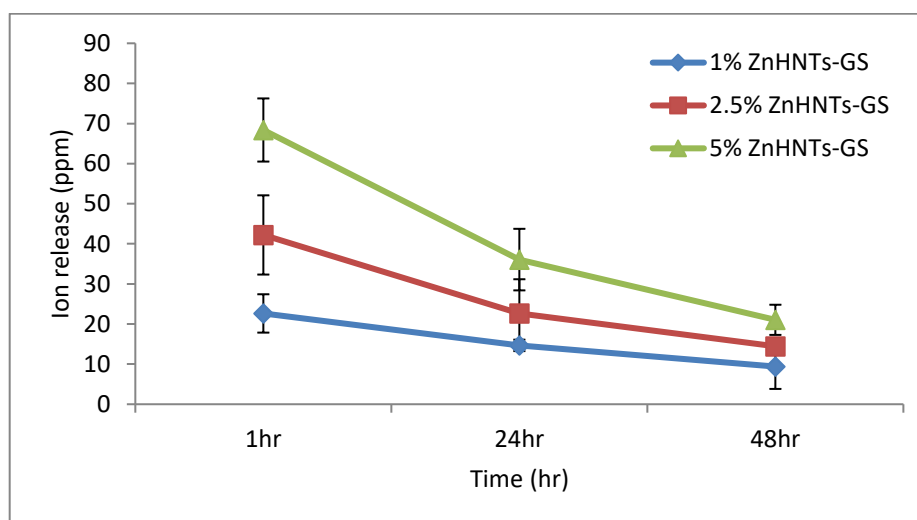


Figure 7-7: Ion release from the coatings, an outburst of ion release is observed, which diminished over time, ($p > 0.05$).

The data shows that the CS-ZnHNTs-GS coatings possess anti-biofouling activity, which can be attributed mainly to the gentamicin antibiotic. Additionally, the release of zinc ions, as well as the positively charged chitosan surface, leads to increased interaction with negatively charged bacterial membranes and might lead to a further enhancement of the anti-biofouling effect.

7.4 Conclusion

Morphological surface characterization using SEM-EDS and EDS mapping confirmed the presence of tubular ZnHNTs structure embedded in the coatings and FTIR analysis confirmed the presence of CS-ZnHNTs-GS in the coatings. Antibacterial evaluation using the agar diffusion method confirmed the anti-biofouling potential of the coatings. Thus, we demonstrate the successful development and evaluation of an anti-biofouling coating for medical devices.

CHAPTER 8

3D PRINTED PLA CONSTRUCTS FUNCTIONALIZED WITH CHITOSAN OLIGOSACCHARIDE LACTATE- ZNHNTS-AG HAVING ANTIMICROBIAL ACTIVITY

8.1 Introduction

3-dimensional printing (3D printing) is a rapidly emerging area of research, gaining increased popularity with each year. It is a rapid prototyping technique that offers tremendous flexibility and optimization potential through adjusting different 3D printing parameters along with the application of different post-3D printing modifications, thus vastly expanding the scope of potential application. It has applications in tissue engineering (Yeh *et al.*, 2015), prosthesis (Zuniga *et al.*, 2015; Gretsche *et al.*, 2016), and medicine (Weisman *et al.*, 2015, 2017, 2019; Tappa *et al.*, 2017). It involves the translation of a digital design file into a three-dimensional model by layer-by-layer deposition of melted polymers, ink droplets, selective laser heating of powder, and selective curing of photosensitive resin (Cheng and Gupta, 2017). An increasing number of non-toxic, biocompatible, and bioresorbable materials such as polylactic acid (PLA) and polycaprolactone (PCL) are being used, resulting in a further increment of applications (Mills, 2015). Though, 3D printing material is a technology holding vast potential by itself, however an immense hurdle impeding the development of 3D printing lies in the fact that the 3D printability of materials used directs their potential utility, thus,

3D printing of artifacts with bioactive properties is a challenge because the majority of bioactive materials are unstable at high temperatures, this issue is exacerbated by the fact that majority mainstream polymers can be extremely stable and hence the materials enclosed within the matrix of the 3D printed artifact might remain embedded in the polymer matrix for extended periods of time till the structure is degraded and the true bioactivity might be diminished, hence, it is vital to integrate appropriate pre/post printing modification strategies to counter the same.

A variety of post 3D printing modifications procedures have been developed for surface activation including the use of polydopamine for increased cell adhesion (Kao *et al.*, 2015), immobilizing herbal medicine (Yeh *et al.*, 2015), rhBMP2 (Lee *et al.*, 2016), chitosan for increased response to macrophages (Almeida *et al.*, 2014), argon and oxygen treatment for increased cell attachment and proliferation (Farina *et al.*, 2017).

Chitosan oligosaccharide lactate (COS) is a shorter derivative of chitosan having excellent water solubility, low molecular weight and shorter chain lengths leading to higher suitability for medical applications; it is biocompatible, biodegradable, non-toxic and suitable for various biomedical applications (Mourya, Inamdar and Choudhari, 2011).

Halloysite nanotubes (HNTs) is an aluminosilicate composite comprising of rolled-up sheets of silica and alumina leading to the opposite charge between outer and inner core; it has significant potential as a drug carrier as its hollow core can be loaded with the material of choice which can be released sustainably over time (M. Massaro *et al.*, 2017). Thus, biocompatible composites can be created by blending chitosan with HNTs.

The objective of this study was to functionalize 3D printed PLA constructs with COS-ZnHNTs-Ag having varying concentrations of Ag (5, 10, and 20 wt.% respectively). Briefly, PLA constructs were printed, dipped in 4 N sodium hydroxide (NaOH) for 10 s and dipped in an antimicrobial suspension consisting of chitosan oligosaccharide lactate-zinc halloysite-silver nitrate (COS-ZnHNTs-Ag). Thus, functionalized 3D printed PLA constructs were characterized using SEM-EDS, EDS mapping, and FTIR. Antimicrobial effects were studied using the disc diffusion and biofilm assay, respectively.

8.2 Materials and Methods

8.2.1 Materials

Chitosan oligosaccharide lactate (COS, Mw = 5,000) with a deacetylation degree of 90%, HNTs, sodium hydroxide (NaOH), silver nitrate (AgNO_3), zinc sulfate heptahydrate ($\text{ZnSO}_4 \cdot 7\text{H}_2\text{O}$), Mueller-Hinton agar, petri dish were purchased from Sigma-Aldrich (St. Louis, MO), 1.75 mm PLA filament and MakerBot Replicator Mini 3D printer from MakerBot (Brooklyn, NY).

8.2.2 Experimental

ZnHNTs were prepared using a modified protocol based on an electrolytic method previously described by Mills et al. (Mills and Boyer, 2018); briefly, an electrolysis setup was assembled consisting of two platinized titanium mesh held parallel at 2-inch distance and connected to a DC power source (VWR Accupower 500 electrophoresis power supply). Ultrasonicated 100 mL aqueous solution of metal salts (2.5 mM) and 50 mg HNTs were dispersed in glass beaker and 20 V was maintained at 80° C with polarity reversal at every 5 min (Khaydarov *et al.*, 2009) under constant

stirring to reduce electrophoretic buildup at the working electrode and thus increase ion density in the solution, afterward the supernatant was decanted thrice, and the solution was centrifuged at 5000 rpm for 5 min with water to separate mHNTs from unabsorbed metal particles and dried at 30° C.

1.75 mm PLA filaments were used for 3D printing using MakerBot replicator mini operating at default print settings (215° C nozzle temperature, 40 mm/s printer head speed, 18 mm/s filament feed rate). Square constructs having 20 x 20x 0.5 mm dimensions were printed. The constructs were dipped in 4 N NaOH for 10 s for increasing hydrophilicity and subsequently functionalized by dip-coating into aqueous ZnHNTs (10 wt.%)–Ag (5, 10, and 20 wt.% respectively)–COS suspension (0.1 g/20 mL) which was previously prepared by overnight magnetic stirring (**Figure 8-1**).

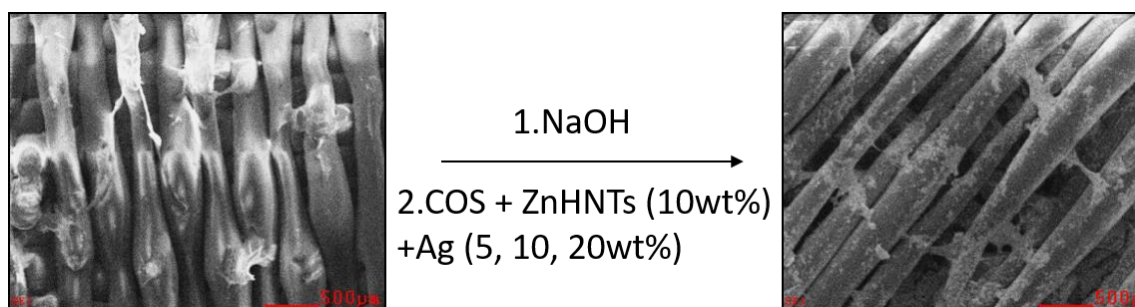


Figure 8-1: Schematic diagram for functionalization of 3D printed PLA scaffolds.

8.2.3 Characterization

The resulting COS-ZnHNTs-Ag coated PLA constructs were characterized using scanning electron microscope and elemental analysis by energy-dispersive X-ray spectroscopy (SEM-EDS, HITACHI S-4800), X-ray fluorescence (XRF, ARLQuant'X, Thermo Fisher Scientific), Fourier-transform infrared spectroscopy (FTIR, Nicolet 6700, Thermo Fisher Scientific) and confocal microscopy (VK-X200, Keyence).

8.3 Results and Discussion

ZnHNTs and Ag^+ ions adsorb to COS which helps in stabilizing the suspension, which was magnetically stirred in order to prevent settling down of the suspension.

PLA constructs (**Figure 8-2**) were unreactive, and no attachment of suspensions due to lack of surface charges was observed, surface activation, hydrophilicity was enhanced by alkaline treatment.

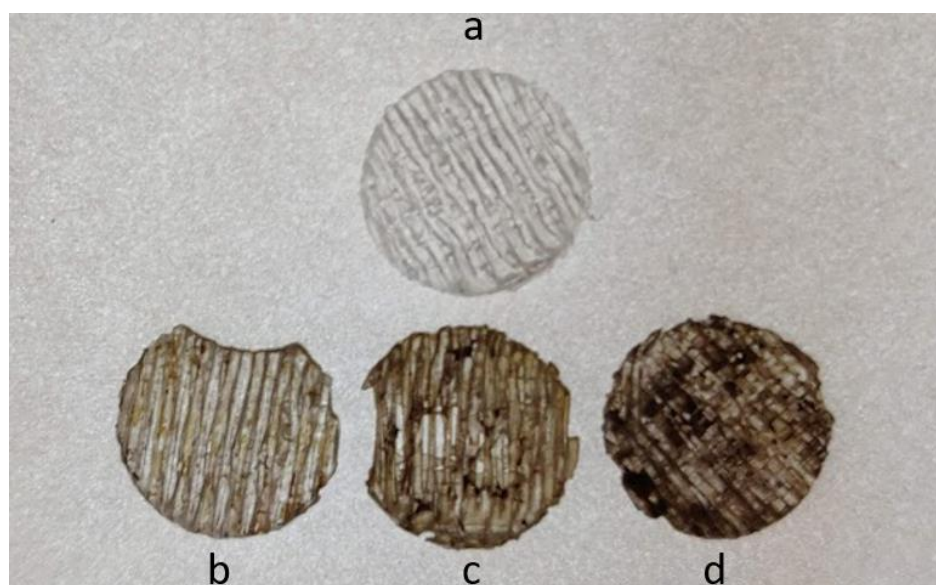


Figure 8-2: 3D printed a. PLA, functionalized with b. COS-ZnHNTs-5%Ag, c. COS-ZnHNTs-10%Ag, and d. COS-ZnHNTs-20%Ag.

Alkaline treatment led to cleavage of the ester bond of PLA and resulted in the formation of a carboxyl and hydroxyl end groups respectively (**Figure 8-3**) which can thus bind dispersed COS with Ag and ZnHNTs.

EDS analysis of the functionalized PLA constructs showed that an increase in the Ag concentration in the COS-ZnHNTs-Ag suspensions led to higher Ag deposits in the functionalization process (**Figure 8-5**).

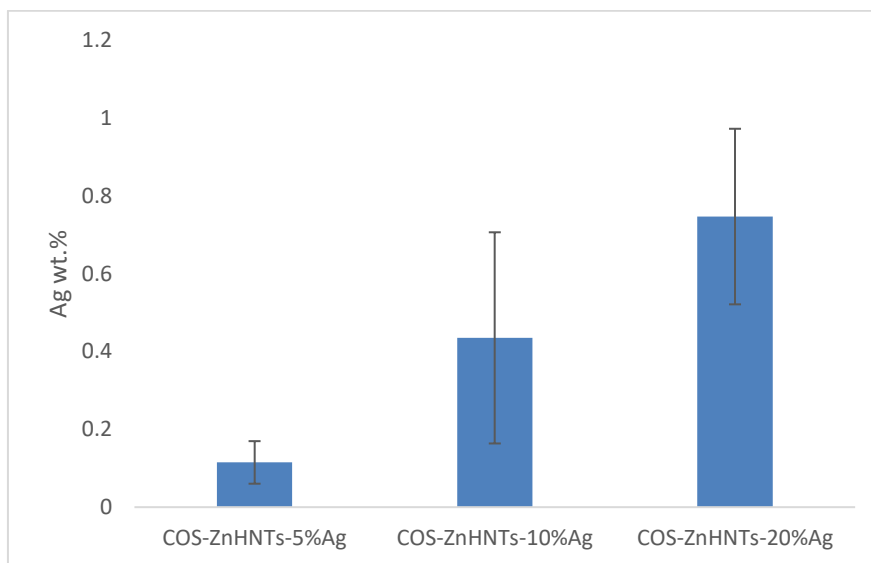


Figure 8-5: EDS analysis of Ag content in the coatings, increasing Ag wt.% in functionalized PLA was observed with a corresponding increase in Ag content in the COS-ZnHNTs-Ag suspension, (n=5).

FTIR was used for chemical analysis and characteristic bands for COS at 3307 for O-H and 2840 cm^{-1} for C-H stretch respectively, peaks for the secondary amide group bending were observed at 1508 and 1027 cm^{-1} respectively, on addition of ZnHNTs more pronounced peaks were observed at 1009 and 913 cm^{-1} respectively corresponding to in-plane Si-O stretching, and O-H deformation of inner surface hydroxyl groups (**Figure 8-6**), further the band at 1025.9 cm^{-1} corresponding to C-O stretching displayed a prominent shift at lower frequency 1008 cm^{-1} indicating the formation of hydrogen bonds with ZnHNTs.

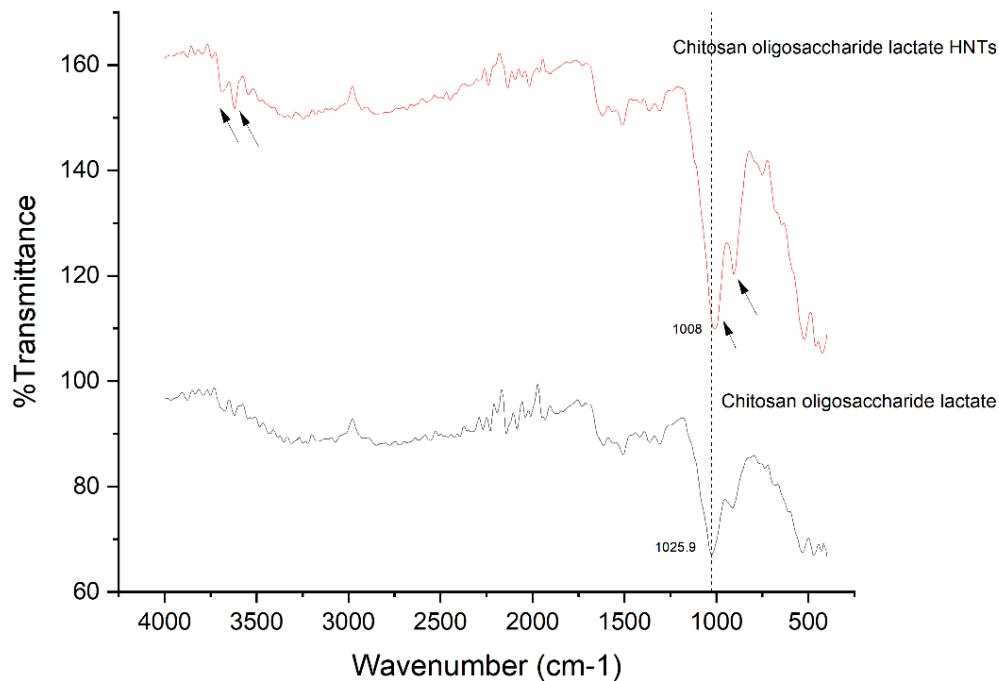


Figure 8-6: FTIR spectra of COS and COS-ZnHNTs-Ag.

Biofouling of medical devices is a constant threat, and the leading cause of infections and the present study was aimed at developing an antimicrobial coating possessing the anti-biofouling capability that can be used for functionalizing 3D printed constructs. Antibacterial potential of the samples was evaluated against gram-positive *S. aureus* bacteria which is the most common bacteria in clinical biofouling using agar diffusion method and the coatings exhibited substantial inhibition zones which can be attributed to release of silver and zinc nanoparticles.

Figure 8-7 shows the average inhibition zone diameter, and the antimicrobial activity was found proportional to the Ag content in the constructs. In a similar study, 3D printed polyetheretherketone functionalized with dopamine showed antimicrobial effects only when Ag was deposited (Deng, Deng and Xie, 2017).

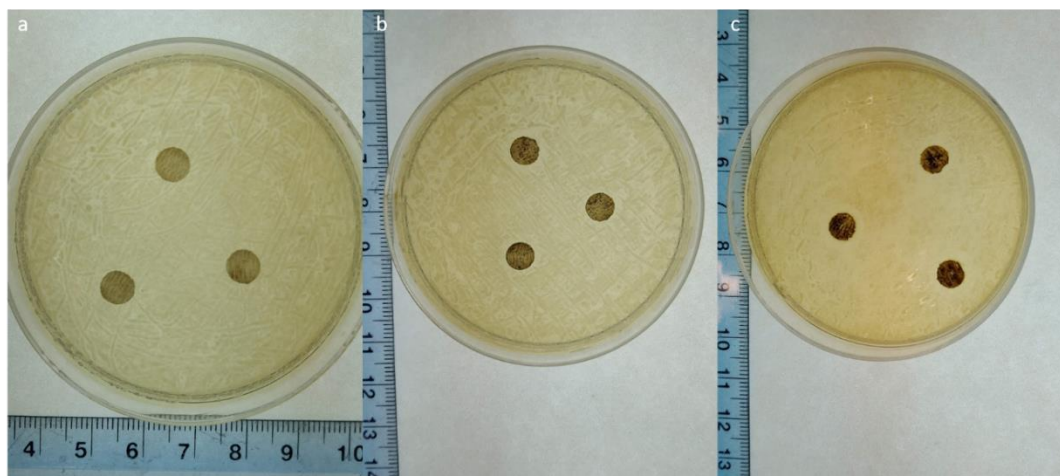


Figure 8-7: Average inhibition diameter against *S. aureus*, a. COS-ZnHNTs-5% Ag (none), b. COS-ZnHNTs-10% Ag ($0.76 \text{ mm} \pm 0.004$), and c. COS-ZnHNTs-20% Ag ($0.80 \text{ mm} \pm 0.01$).

Figure 8-8 shows the crystal violet biofilm assay for the functionalized constructs, increasing silver content had an inhibitory effect on the biofilm formation, silver is a well-known antimicrobial agent that has significant anti-biofilm properties well documented in numerous studies (Martinez-Gutierrez *et al.*, 2013; Palanisamy *et al.*, 2014).

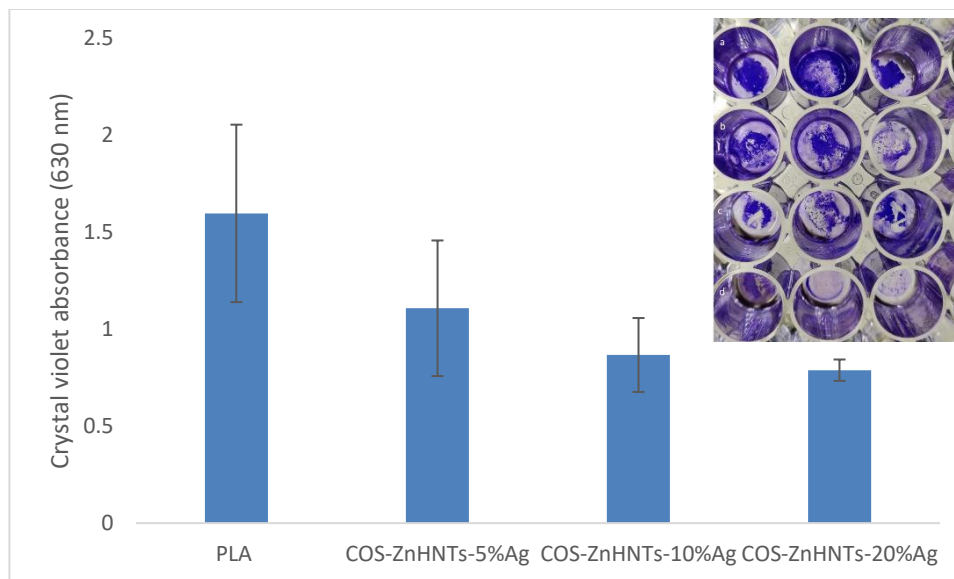


Figure 8-8: Crystal violet biofilm assay, increasing Ag content in the coatings had an inhibitory effect on the *S. aureus* biofilm formation. Inset – a. control (b, c, d) COS-ZnHNTs- 5, 10, and 20% Ag respectively.

The data shows that COS-ZnHNTs-Ag functionalized coatings possessed anti-biofouling activity that can be attributed mainly to Ag and Zn ion release; furthermore, the positively charged COS surface interacts strongly with the bacterial membrane thus, supplementing the anti-biofouling effect.

8.4 Conclusion

Using commercial 3D printing technique PLA constructs were made which were chemically surface activated to increase hydrophilicity, and suspensions of COS-ZnHNTs-Ag were adsorbed on the constructs.

Morphological surface characterization using SEM-EDS confirmed the presence of the suspension coatings on the constructs, FTIR analysis confirmed the presence of COS-ZnHNTs-Ag in the coatings. Antibacterial evaluation using the agar diffusion

method confirmed the anti-biofouling potential of the PLA constructs (which was a function of the Ag content in the material).

Thus, we demonstrate successful development and evaluation of a functionalization coating having antimicrobial activity for 3D printed constructs.

CHAPTER 9

TWO-STAGE ELECTROLYTIC SYNTHESIS OF DOUBLE METAL COATED MHNTS

9.1 Introduction

Halloysite nanotubes (HNTs, $[\text{Al}_2\text{Si}_2\text{O}_5(\text{OH})_4 \cdot 2\text{H}_2\text{O}]$), an aluminosilicate of the kaolin group consists of positively charged octahedral $\text{Al}(\text{OH})_3$ and negatively charged tetrahedral SiO_4 sheets, it is characterized by resistance to moisture, high sorption capacity to various molecules because of charge separation across its lumen and outer surface it can adsorb cationic as well as anionic species, using different mechanisms, and due to the presence of hydroxyl groups it can be easily modified using different chemicals (Kurczewska *et al.*, 2015).

In recent years, there has been significant progress in the development of new materials based on HNTs; nanostructured aluminosilicates are investigated due to their well-defined structure, ease of modification, biofriendly properties (Vergaro *et al.*, 2010), and high accessibility. HNTs have been used as adsorbents (Xie *et al.*, 2011), catalyst supports (Carrillo and Carriazo, 2015), antimicrobial agents (Shu *et al.*, 2017), drug carrier (Abdullayev and Lvov, 2013). Due to high surface area to volume ratio HNTs can adsorb significantly more significant amount of substances, different materials including covalently attached catalysts on the HNTs surface can be utilized and recovered post-use (Yi Zhang *et al.*, 2013), hollow lumen can function as a container for loading materials of

choice which can be systematically released in a controlled manner over prolonged periods of time (Zhang *et al.*, 2015), drug loaded HNTs are increasingly finding more applications in cancer research due to their non-toxicity (Zhang, Ouyang and Yang, 2014).

However, raw untreated HNTs are significantly unreactive and have to be modified with regards to the application of interest before they can be used, different compounds can be adsorbed directly on HNTs outer surface (M Massaro *et al.*, 2017).

Herein, we describe a novel two-step electrolytic mechanism to metallize the outer surface of HNTs with two different metals -silver (Ag) and zinc (Zn).

Resulting mHNTs were characterized using SEM-EDS, XRD, FTIR, and XRF.

9.2 Materials and Methods

9.2.1 Materials

Silver Nitrate (AgNO_3), HNTs, zinc sulfate heptahydrate (ZnSO_4) were purchased from Sigma-Aldrich (St. Louis, MO). Platinized titanium mesh electrodes (2"x3"), VWR Accupower 500 electrophoresis power supply, TekPower TP9605BT USB multimeter, and silicon carbide abrasive sandpaper were purchased from Amazon.com LLC (Seattle, WA).

9.2.2 Methods

In the first step, the mHNTs were prepared using a modified protocol based on an electrolytic method previously described by Mills *et al.* (Mills and Boyer, 2018); briefly; an electrolysis setup was assembled consisting of two platinized titanium mesh held parallel at 2 inch distance and connected to a DC power source (VWR Accupower 500 electrophoresis power supply). First, ultrasonicated 100 mL aqueous solution of AgNO_3

(2.5 mM) and 50 mg HNTs were dispersed in glass beaker and 20 V was maintained at 80° C with polarity reversal at every 5 min (Khaydarov *et al.*, 2009) under constant stirring to reduce electrophoretic buildup at the working electrode and thus increase ion density in the solution, afterward the supernatant was decanted thrice, and the solution was centrifuged at 5000 rpm for 5 min with water to separate mHNTs from un-adsorbed metal particles and dried at 30° C.

The second step consisted of re-dispersing the mHNTs previously prepared (50 mg) in a similar composition electrolytic medium but with different metal salt (ZnSO₄, 2.5 mM) and the experiment was carried following same parameters as described above.

9.2.3 Characterization

The resulting silver-zinc-Halloysite nanotubes (AgZnHNTs) were characterized using scanning electron microscope (SEM), energy-dispersive spectroscopy (EDS), Fourier-transform infrared spectroscopy (FTIR), X-ray fluorescence (XRF) and X-ray powder diffraction (XRD).

9.3 Results and Discussion

The feasibility of the electrolytic method for depositing two metals in a two-stage method on HNTs was explored. AgNO₃, when dissolved in water, splits into ions producing Ag⁺ and NO₃⁻ ions respectively, on the application of voltage the silver metal ions were reduced on cathode to Ag NPs which on polarity reversal were released from the former cathode into the system where they were adsorbed by HNTs, the system was continuously magnetically stirred in order to ensure even distribution of the free un-adsorbed components with HNTs.

The AgHNTs produced were collected and were reused in the second step consisting of different metal salt ZnSO_4 , and the same procedure was repeated. The results are in agreement with previous studies, Shu et al. deposited Ag and ZnO mixed at different ratios using chemical reduction (Shu *et al.*, 2017), and iron oxide (Fe_3O_4) and Ag were similarly deposited on HNTs for antimicrobial activity (Fu *et al.*, 2016).

Figure 9-1 shows the EDS map of AgZnHNTs, where a cylindrical structure can be observed and almost evenly distributed Ag with patches of Zn clusters on the outer surface of HNTs, similar results were obtained using XRF elemental analysis (**Figure 9-2**).

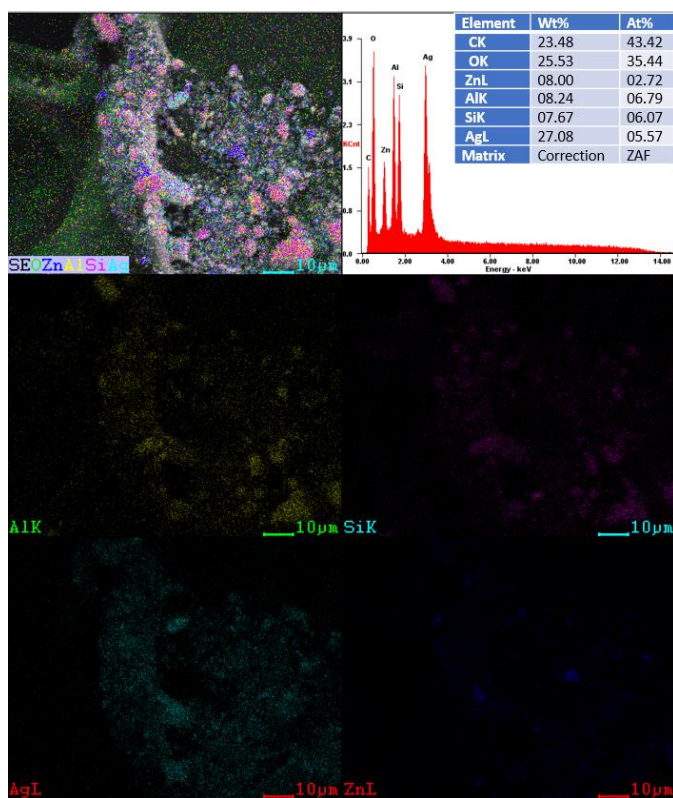


Figure 9-1: SEM-EDS map of AgZnHNTs. Ag can be observed almost evenly distributed throughout the HNTs surface with interspersed patches of Zn.

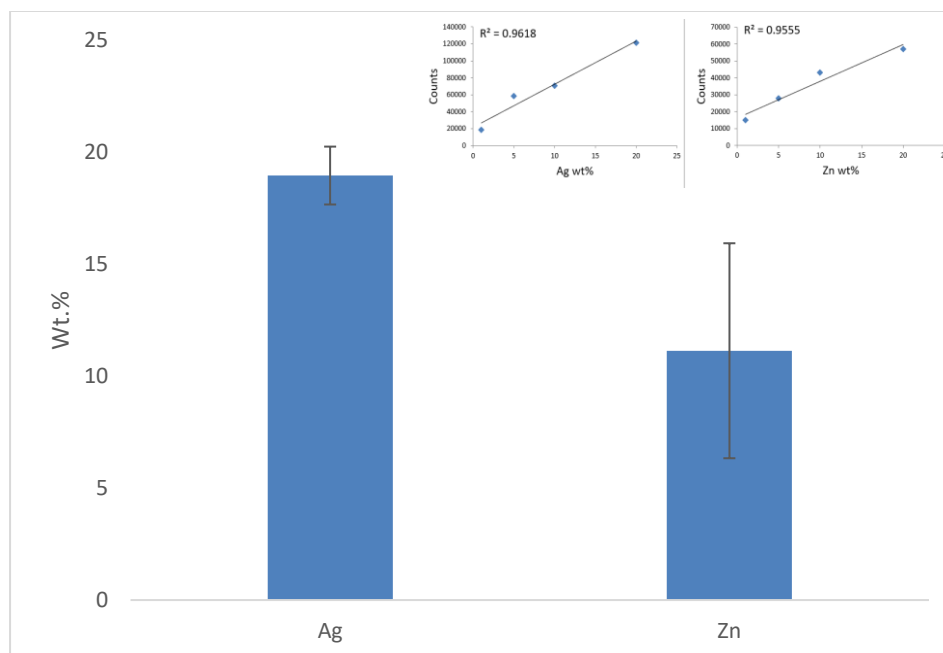


Figure 9-2: XRF quantitative elemental analysis of AgZnHNTs showing the presence of silver and zinc on mHNTs. Inset XRF calibration curve for Ag and Zn, respectively, n=5.

Chemical analysis of pristine HNTs was performed using FTIR which revealed the presence of characteristic absorption bands for HNTs at 3690, 3620, 1031.9, 903, and 748 cm^{-1} respectively corresponding to O-H stretching of inner surface hydroxyl groups, O-H stretching of inner hydroxyl groups, in-plane Si-O stretching, O-H deformation of inner hydroxyl groups, and perpendicular Si-O stretching respectively (**Figure 9-3**).

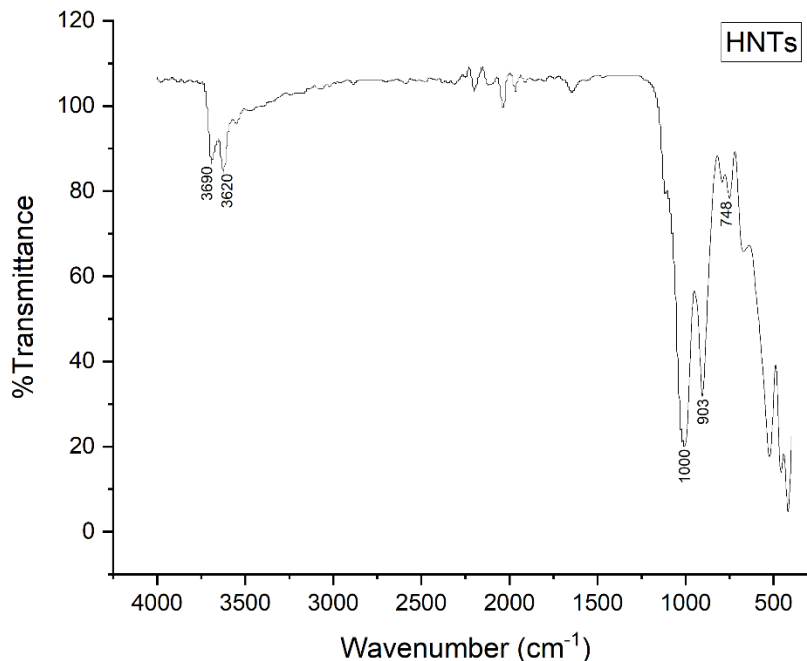


Figure 9-3: FTIR pattern of as received HNTs displaying the characteristic FTIR pattern. The characteristic peaks around 3690, 3620, 1000, and 903 cm^{-1} respectively corresponding to O-H stretching of the inner surface hydroxyl groups, O-H stretching of inner hydroxyl groups, Si-O stretching vibrations, and Al-OH vibrations were recorded.

Figure 9-4 shows the XRD pattern of the samples, HNTs exhibit the characteristic pattern at $2\theta = 12, 20, 25^\circ$ which correspond to the (001), (020), and (002) crystal planes of the raw HNTs, metallization of the HNTs results in decrement of the surface area exposed to the incident X-ray resulting into weakening of the HNTs signal due to which the HNTs characteristic peaks are observed extremely weak in the AgZnHNTs composite XRD pattern.

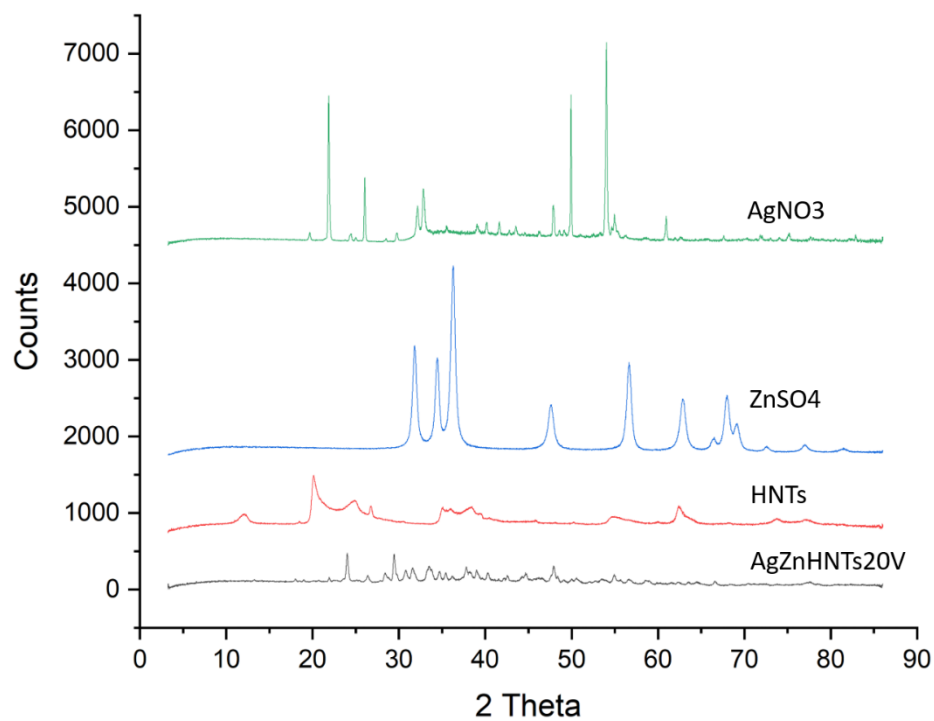


Figure 9-4: XRD of AgZnHNTs, HNTs, AgNO₃, and ZnSO₄.

Figure 9-5 shows the current flow in the electrolytic system, a higher current flow is detected in the second stage which could be due to the addition of the second metal salt as well as the first metal adsorbed on the HNTs previously.

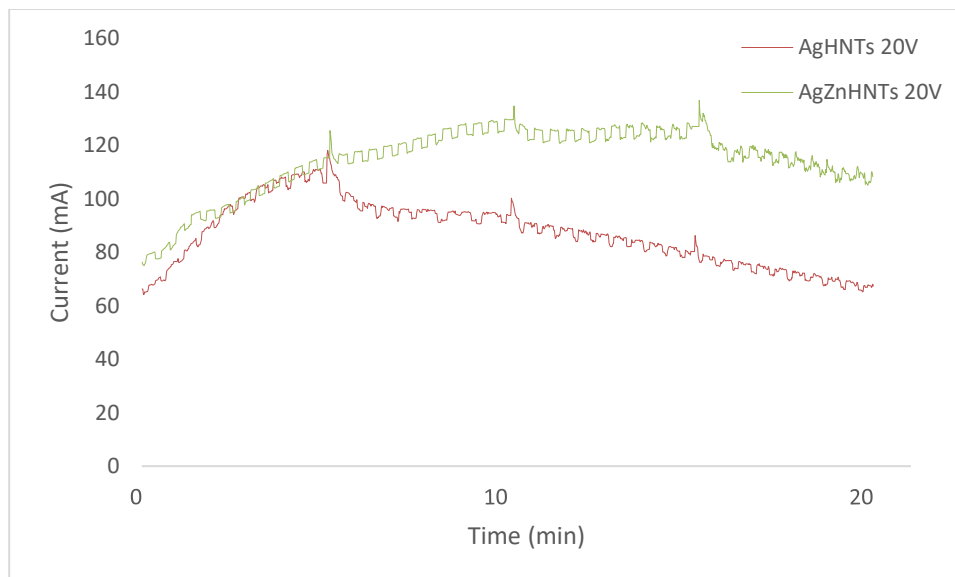
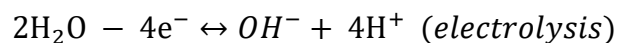
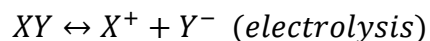


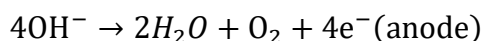
Figure 9-5: Current flow in the first and second steps.

The process can be chemically explained in the following steps-

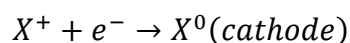


The first stage comprises of the following chemical reactions, on the application of voltage metal salt (XY) splits into X^+ and Y^- , and water splits into OH^- and H^+ ions respectively.

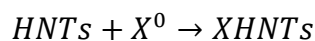
At the anode Y^- and OH^- compete, OH^- ions having greater oxidation potential get liberated forming water and oxygen.



Simultaneously, X^+ ions move towards the cathode where H^+ and X^+ compete, X^+ having higher reduction potential gets reduced and hence get deposited more readily as compared to the H^+ ion.

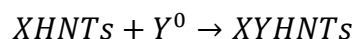


X^0 nanoparticles grow via nucleation and van der Waals forces and get separated from the cathode due to stirring and polarity change and get adsorbed to the dispersed HNTs and form XHNTs (mHNTs).



On increasing the applied voltage, the reversible electrolysis reaction is further shifted to the right, and more X^+ ions are available in the system that can interact with the HNTs. On reversing the voltage, more X^0 is released, leading to increased X^0 ionic concentration resulting in higher deposition on HNTs.

The second stage involves the addition of a different salt (Y), which similarly gets reduced as described above and adsorbs on the available surface on X HNTs.



9.4 Conclusion

Herein, we described a novel electrolytic method for metallizing the external surface of HNTs without the use of any toxic reagents. SEM-EDS, FTIR, and XRD were used for characterization, and two different metals were sequentially deposited on the outer surface of the HNTs. In the future, we aim to explore the antimicrobial and other properties of such nanocomposites.

We believe our process can be extended to the metallization of other adsorbent materials as well.

CHAPTER 10

CONCLUSIONS AND FUTURE WORK

10.1 Conclusions

Feasibility of the electrolytic method for regulated metallization of HNTs was explored, and differential effects of HNTs extent of metallization on antimicrobial properties and cytotoxicity were successfully demonstrated. Imaging and EDAX analysis confirmed the presence of metal coating and XRF confirmed the metal quantity, using disc diffusion assay when inoculated with *S. aureus* clear zone of inhibition were observed for the mHNTs, and the addition of mHNTs led to augmented antibacterial properties, and ZnHNTs and CuHNTs were found to be cytocompatible.

mHNTs were integrated into various biomedical applications such as titanium implants, 3D printing, and antibacterial coatings, and positive results were observed for the antimicrobial activity.

In titanium implants and antimicrobial coatings, mHNTs served as a controlled drug release container. Cytological assays demonstrated the cytocompatibility of the mHNTs. Furthermore, mHNTs were integrated into the functionalization of 3D printed PLA, and lastly, an electrolytic two-step protocol was developed for depositing two metals on the HNTs surface.

10.2 Future Work

Future work will be focused on testing different metals combinations on HNTs, and their combinations against more extensive ranges of bacteria will be explored, metallization methods besides electrolysis will be explored as a means of more accurately controlling the extent of metallization.

APPENDIX A

IMAGEJ ANALYSIS OF LIVE/DEAD ASSAYS

Live/Dead assays are of qualitative as well as quantitative nature, here we attempted to use it as both. In order to count the number of cells following steps were followed in ImageJ (1.52a)-

- Convert to 8-bit greyscale (Image>Type>8-bit).
- Threshold, default, and B&W settings (Image>Adjust>Threshold).
- Watershed creates an outline between closely placed objects.
(Process>Binary>Watershed).
- Particles (cells) were analyzed at 50-200in², circularity 0-1
(Analyze>Analyze Particles).
- In order to prevent operator bias, the process was also automated for comparison using a customized macro written in JavaScript –

```
1 run("8-bit");
2 setAutoThreshold("Default");
3 //run("Threshold...");
4 //setThreshold(0, 32);
5 setOption("BlackBackground", true);
6 run("Convert to Mask");
7 run("Close");
8 run("Analyze Particles...", "display exclude clear summarize in_situ");
9 saveAs("Results", "E:/1/Results.csv");
```

Figure A-1: JavaScript macro for automated cell counting.

BIBLIOGRAPHY

Abdelgawad, A. M., Hudson, S. M. and Rojas, O. J. (2014) 'Antimicrobial wound dressing nanofiber mats from multicomponent (chitosan/silver-NPs/polyvinyl alcohol) systems', *Carbohydrate polymers*. Elsevier, 100, pp. 166–178.

Abdulkareem, E. H. *et al.* (2015) 'Anti-biofilm activity of zinc oxide and hydroxyapatite nanoparticles as dental implant coating materials', *Journal of dentistry*. Elsevier, 43(12), pp. 1462–1469.

Abdullayev, E. *et al.* (2011) 'Natural tubule clay template synthesis of silver nanorods for antibacterial composite coating', *ACS applied materials & interfaces*. ACS Publications, 3(10), pp. 4040–4046.

Abdullayev, E. and Lvov, Y. (2013) 'Halloysite clay nanotubes as a ceramic "skeleton" for functional biopolymer composites with sustained drug release', *Journal of materials chemistry B*. Royal Society of Chemistry, 1(23), pp. 2894–2903.

Adell, R. *et al.* (1981) 'A 15-year study of osseointegrated implants in the treatment of the edentulous jaw', *International journal of oral surgery*. Elsevier, 10(6), pp. 387–416.

Alexander, J. W. (2009) 'History of the medical use of silver', *Surgical infections*. Mary Ann Liebert, Inc. 140 Huguenot Street, 3rd Floor New Rochelle, NY 10801 USA, 10(3), pp. 289–292.

Almeida, C. R. *et al.* (2014) 'Impact of 3-D printed PLA-and chitosan-based scaffolds on human monocyte/macrophage responses: unraveling the effect of 3-D structures on inflammation', *Acta biomaterialia*. Elsevier, 10(2), pp. 613–622.

Anitha, A. *et al.* (no date) 'Chitin and chitosan in selected biomedical applications', *Elsevier*. Available at:
<https://www.sciencedirect.com/science/article/pii/S0079670014000288> (Accessed: 12 June 2019).

Augello, C. and Liu, H. (2015) 'Surface modification of magnesium by functional polymer coatings for neural applications', *Surface Modification of Magnesium and its Alloys for Biomedical Applications*. Woodhead Publishing, pp. 335–353. doi: 10.1016/B978-1-78242-078-1.00012-8.

- Barrere, F. v *et al.* (2002) 'Nucleation of biomimetic Ca–P coatings on Ti6Al4V from a SBF× 5 solution: influence of magnesium', *Biomaterials*. Elsevier, 23(10), pp. 2211–2220.
- Boyer, C. J. (2016) 'Clay nanotube composites for antibacterial nanostructured coatings'. Louisiana Tech University.
- Boyer, C. J. *et al.* (2018) 'Antibacterial and antibiofouling clay nanotube–silicone composite', *Medical devices (Auckland, NZ)*. Dove Press, 11, p. 123.
- Boyer, C. J. *et al.* (2019) '3D printing for bio-synthetic biliary stents', *Bioengineering*. Multidisciplinary Digital Publishing Institute, 6(1), p. 16.
- Busscher, H. J. *et al.* (2012) 'Biomaterial-associated infection: locating the finish line in the race for the surface', *Science translational medicine*. American Association for the Advancement of Science, 4(153), pp. 153rv10-153rv10.
- Carrillo, A. M. and Carriazo, J. G. (2015) 'Cu and Co oxides supported on halloysite for the total oxidation of toluene', *Applied Catalysis B: Environmental*. Elsevier, 164, pp. 443–452.
- Chen, Q. *et al.* (2012) 'Fabrication and evaluation of Bis-GMA/TEGDMA dental resins/composites containing halloysite nanotubes', *Dental Materials*. Elsevier, 28(10), pp. 1071–1079.
- Cheng, C. and Gupta, M. (2017) 'Surface functionalization of 3D-printed plastics via initiated chemical vapor deposition', *Beilstein journal of nanotechnology*. Beilstein-Institut, 8(1), pp. 1629–1636.
- Chozhanathmisra, M. *et al.* (2016) 'Development of zinc-halloysite nanotube/minerals substituted hydroxyapatite bilayer coatings on titanium alloy for orthopedic applications', *Colloids and Surfaces A: Physicochemical and Engineering Aspects*. Elsevier, 511, pp. 357–365. doi: 10.1016/J.COLSURFA.2016.10.018.
- Cox, S. C. *et al.* (2016) 'Adding functionality with additive manufacturing: Fabrication of titanium-based antibiotic eluting implants', *Materials Science and Engineering: C*. Elsevier, 64, pp. 407–415.
- Darouiche, R. O. (2004) 'Treatment of infections associated with surgical implants', *New England Journal of Medicine*. Mass Medical Soc, 350(14), pp. 1422–1429.
- Das, S. and Jana, S. (2015) 'A facile approach to fabricate halloysite/metal nanocomposites with preformed and in situ synthesized metal nanoparticles: a comparative study of their enhanced catalytic activity', *Dalton Transactions*. Royal Society of Chemistry, 44(19), pp. 8906–8916.

Deng, L., Deng, Y. and Xie, K. (2017) 'AgNPs-decorated 3D printed PEEK implant for infection control and bone repair', *Colloids and Surfaces B: Biointerfaces*. Elsevier, 160, pp. 483–492.

Dikici, B. *et al.* (2016) 'preparation and characterization of chitosan/hydroxyapatite sol-gel coating on Ti-6Al-4V', in *International Conference on Advanced Materials and Systems (ICAMS)*. The National Research & Development Institute for Textiles and Leather-INCDTP, pp. 263–267.

Dong, J. and Zhang, J. (2018) 'Biomimetic super anti-wetting coatings from natural materials: superamphiphobic coatings based on nanoclays', *Scientific reports*. Nature Publishing Group, 8(1), p. 12062.

Donlan, R. M. (2001) 'Biofilm formation: a clinically relevant microbiological process', *Clinical Infectious Diseases*. The University of Chicago Press, 33(8), pp. 1387–1392.

Du, M., Guo, B. and Jia, D. (2010) 'Newly emerging applications of halloysite nanotubes: a review', *Polymer International*. Wiley Online Library, 59(5), pp. 574–582.

Egger, S. *et al.* (2009) 'Antimicrobial properties of a novel silver-silica nanocomposite material', *Applied and environmental microbiology*. Am Soc Microbiol, 75(9), pp. 2973–2976.

Elias, C. N. *et al.* (2008) 'Biomedical applications of titanium and its alloys', *Jom*. Springer, 60(3), pp. 46–49.

Elshikh, M. *et al.* (2016) 'Resazurin-based 96-well plate microdilution method for the determination of minimum inhibitory concentration of biosurfactants', *Biotechnology letters*. Springer, 38(6), pp. 1015–1019.

Engelsman, A. F. *et al.* (2007) 'The phenomenon of infection with abdominal wall reconstruction', *Biomaterials*. Elsevier, 28(14), pp. 2314–2327.

Farina, M. *et al.* (2017) '3D printed vascularized device for subcutaneous transplantation of human islets', *Biotechnology journal*. Wiley Online Library, 12(9), p. 1700169.

Farrokhi-Rad, M., Fateh, A. and Shahrabi, T. (2018) 'Electrophoretic deposition of vancomycin loaded halloysite nanotubes-chitosan nanocomposite coatings', *Surface and Coatings Technology*. Elsevier, 349, pp. 144–156. doi: 10.1016/J.SURFCOAT.2018.05.070.

Farrokhi-Rad, M. and Ghorbani, M. (2011) 'Electrophoretic Deposition of Titania Nanoparticles in Different Alcohols: Kinetics of Deposition', *Journal of the American Ceramic Society*. John Wiley & Sons, Ltd (10.1111), 94(8), pp. 2354–2361. doi: 10.1111/j.1551-2916.2011.04401.x.

Feng, K. *et al.* (2018) 'Fabrication of high performance superhydrophobic coatings by spray-coating of polysiloxane modified halloysite nanotubes', *Chemical Engineering Journal*. Elsevier, 331, pp. 744–754.

Fu, H. *et al.* (2016) 'Preparation and characterization of novel modified halloysite-Fe₃O₄-Ag/polyurea nanocomposites with antibacterial property', *International Journal of Polymeric Materials and Polymeric Biomaterials*. Taylor & Francis, 65(17), pp. 863–871.

Fu, Y. and Zhang, L. (2005) 'Deposition feature of Ni nanoparticles on halloysite template and magnetic properties of the composite', *Journal of nanoscience and nanotechnology*. American Scientific Publishers, 5(7), pp. 1113–1119.

Gbejuade, H. O., Lovering, A. M. and Webb, J. C. (2015) 'The role of microbial biofilms in prosthetic joint infections: a review', *Acta orthopaedica*. Taylor & Francis, 86(2), pp. 147–158.

Grass, G., Rensing, C. and Solioz, M. (2011) 'Metallic copper as an antimicrobial surface', *Applied and environmental microbiology*. Am Soc Microbiol, 77(5), pp. 1541–1547.

Gretsch, K. F. *et al.* (2016) 'Development of novel 3D-printed robotic prosthetic for transradial amputees', *Prosthetics and orthotics international*. SAGE Publications Sage UK: London, England, 40(3), pp. 400–403.

Grimes, W. R. *et al.* (2018) 'Bi-Functionalized Clay Nanotubes for Anti-Cancer Therapy', *Applied Sciences*. Multidisciplinary Digital Publishing Institute, 8(2), p. 281.

Gunpath, U. F. *et al.* (2018) 'Anodised TiO₂ nanotubes as a scaffold for antibacterial silver nanoparticles on titanium implants', *Materials Science and Engineering: C*. Elsevier, 91, pp. 638–644.

Hajipour, M. J. *et al.* (2012) 'Antibacterial properties of nanoparticles', *Trends in biotechnology*. Elsevier, 30(10), pp. 499–511.

Harrison, J. J. *et al.* (2004) 'Biofilm susceptibility to metal toxicity', *Environmental Microbiology*. Wiley Online Library, 6(12), pp. 1220–1227.

Harrison, J. J. *et al.* (2008) 'Copper and quaternary ammonium cations exert synergistic bactericidal and antibiofilm activity against *Pseudomonas aeruginosa*', *Antimicrobial agents and chemotherapy*. Am Soc Microbiol, 52(8), pp. 2870–2881.

van Hengel, I. A. J. *et al.* (2017) 'Selective laser melting porous metallic implants with immobilized silver nanoparticles kill and prevent biofilm formation by methicillin-resistant *Staphylococcus aureus*', *Biomaterials*. Elsevier, 140, pp. 1–15.

- Hermawan, A. A. *et al.* (2018) 'Halloysite nanotubes as a fine grained material for heavy metal ions removal in tropical biofiltration systems', *Applied Clay Science*. Elsevier, 160, pp. 106–115.
- Høiby, N. *et al.* (2011) 'The clinical impact of bacterial biofilms', *International journal of oral science*. Nature Publishing Group, 3(2), p. 55.
- Holmberg, K. V *et al.* (2013) 'Bio-inspired stable antimicrobial peptide coatings for dental applications', *Acta biomaterialia*. Elsevier, 9(9), pp. 8224–8231.
- Hoyle, B. D., Wong, C. K. W. and Costerton, J. W. (1992) 'Disparate efficacy of tobramycin on Ca²⁺-, Mg²⁺-, and HEPES-treated *Pseudomonas aeruginosa* biofilms', *Canadian journal of microbiology*. NRC Research Press, 38(11), pp. 1214–1218.
- Hu, H. *et al.* (2012) 'Antibacterial activity and increased bone marrow stem cell functions of Zn-incorporated TiO₂ coatings on titanium', *Acta biomaterialia*. Elsevier, 8(2), pp. 904–915.
- Inoue, D. *et al.* (2019) 'Iodine-supported titanium implants have good antimicrobial attachment effects', *Journal of Orthopaedic Science*. Elsevier, 24(3), pp. 548–551.
- Ismail, A. F. H. *et al.* (2016) 'Spectrophotometric determination of gentamicin loaded PLGA microparticles and method validation via ninhydrin-gentamicin complex as a rapid quantification approach', *Journal of Applied Pharmaceutical Science*, 6(01), pp. 7–14.
- Jammalamadaka, U., Tappa, K. and Mills, D. K. (2018) 'Calcium phosphate/clay nanotube bone cement with enhanced mechanical properties and sustained drug release', in *Current Topics in the Utilization of Clay in Industrial and Medical Applications*. IntechOpen.
- Jana, S. *et al.* (2017) 'Halloysite nanotubes with immobilized silver nanoparticles for anti-bacterial application', *Colloids and Surfaces B: Biointerfaces*. Elsevier, 151, pp. 249–254.
- Jayakrishnan, D. S. (2012) 'Electrodeposition: the versatile technique for nanomaterials', in *Corrosion Protection and Control Using Nanomaterials*. Elsevier, pp. 86–125.
- Jin, G. *et al.* (2014) 'Osteogenic activity and antibacterial effect of zinc ion implanted titanium', *Colloids and Surfaces B: Biointerfaces*. Elsevier, 117, pp. 158–165.
- Joussein, E. *et al.* (2005) 'Halloysite clay minerals—a review'. De Gruyter.
- Kaneko, Y. *et al.* (2007) 'The transition metal gallium disrupts *Pseudomonas aeruginosa* iron metabolism and has antimicrobial and antibiofilm activity', *The Journal of clinical investigation*. Am Soc Clin Investig, 117(4), pp. 877–888.

- Kao, C.-T. *et al.* (2015) 'Poly (dopamine) coating of 3D printed poly (lactic acid) scaffolds for bone tissue engineering', *Materials Science and Engineering: C*. Elsevier, 56, pp. 165–173.
- Khaydarov, R. A. *et al.* (2009) 'Electrochemical method for the synthesis of silver nanoparticles', *Journal of Nanoparticle Research*. Springer, 11(5), pp. 1193–1200.
- Kiani, G. (2014) 'High removal capacity of silver ions from aqueous solution onto halloysite nanotubes', *Applied Clay Science*. Elsevier, 90, pp. 159–164.
- Kokubo, T. and Takadama, H. (2006) 'How useful is SBF in predicting in vivo bone bioactivity?', *Biomaterials*. Elsevier, 27(15), pp. 2907–2915.
- Kramer, J. and Kirshbaum, A. (1961) 'Effect of paper on the performance assay in the control of antibiotic sensitivity discs', *Appl. Environ. Microbiol.* Am Soc Microbiol, 9(4), pp. 334–336.
- Kurczewska, J. *et al.* (2015) 'High decrease in soil metal bioavailability by metal immobilization with halloysite clay', *Environmental chemistry letters*. Springer, 13(3), pp. 319–325.
- Kvitek, L. *et al.* (2008) 'Effect of surfactants and polymers on stability and antibacterial activity of silver nanoparticles (NPs)', *The Journal of Physical Chemistry C*. ACS Publications, 112(15), pp. 5825–5834.
- Lee, S. J. *et al.* (2016) 'Surface modification of 3D-printed porous scaffolds via mussel-inspired polydopamine and effective immobilization of rhBMP-2 to promote osteogenic differentiation for bone tissue engineering', *Acta biomaterialia*. Elsevier, 40, pp. 182–191.
- Lemire, J. A., Harrison, J. J. and Turner, R. J. (2013) 'Antimicrobial activity of metals: mechanisms, molecular targets and applications', *Nature Reviews Microbiology*. Nature Publishing Group, 11(6), p. 371.
- Levy, S. B. (1998) 'The challenge of antibiotic resistance', *Scientific American*. JSTOR, 278(3), pp. 46–53.
- Li, L.-H. *et al.* (2010) 'Preparation, characterization and antimicrobial activities of chitosan/Ag/ZnO blend films', *Chemical Engineering Journal*. Elsevier, 160(1), pp. 378–382.
- Lima, E. M. C. X. *et al.* (2008) 'Adsorption of salivary and serum proteins, and bacterial adherence on titanium and zirconia ceramic surfaces', *Clinical oral implants research*. Wiley Online Library, 19(8), pp. 780–785.

- Liu, M. *et al.* (2014) 'Recent advance in research on halloysite nanotubes-polymer nanocomposite', *Progress in polymer science*. Elsevier, 39(8), pp. 1498–1525.
- Liu, P. and Zhao, M. (2009) 'Silver nanoparticle supported on halloysite nanotubes catalyzed reduction of 4-nitrophenol (4-NP)', *Applied Surface Science*. Elsevier, 255(7), pp. 3989–3993.
- Lvov, Y. M. *et al.* (2008) 'Halloysite clay nanotubes for controlled release of protective agents', *ACS nano*. ACS Publications, 2(5), pp. 814–820.
- Lyon, D. Y. *et al.* (2008) 'Assessing the antibiofouling potential of a fullerene-coated surface', *International Biodeterioration & Biodegradation*. Elsevier, 62(4), pp. 475–478.
- Martinez-Gutierrez, F. *et al.* (2013) 'Anti-biofilm activity of silver nanoparticles against different microorganisms', *Biofouling*. Taylor & Francis, 29(6), pp. 651–660.
- Massaro, M. *et al.* (2017) 'Covalently modified halloysite clay nanotubes: synthesis, properties, biological and medical applications', *Journal of Materials Chemistry B*. The Royal Society of Chemistry, 5(16), pp. 2867–2882. doi: 10.1039/C7TB00316A.
- Massaro, M *et al.* (2017) 'Halloysite nanotubes as support for metal-based catalysts', *Journal of Materials Chemistry A*. Royal Society of Chemistry, 5(26), pp. 13276–13293.
- McLean, R. J. C., Lam, J. S. and Graham, L. L. (2012) 'Training the biofilm generation—a tribute to JW Costerton', *Journal of bacteriology*. Am Soc Microbiol, 194(24), pp. 6706–6711.
- Mills, D. and Boyer, C. (2018) 'Method for metalizing nanotubes through electrolysis'. Google Patents.
- Mills, D. K. (2015) 'Future Medicine: The Impact of 3D Printing', *J. Nanomater. Mol. Nanotechnol*, 4, pp. 1–3.
- Mourya, V. K., Inamdar, N. N. and Choudhari, Y. M. (2011) 'Chitooligosaccharides: Synthesis, characterization and applications', *Polymer Science Series A*. Springer, 53(7), pp. 583–612.
- Nablo, B. J. and Schoenfisch, M. H. (2003) 'Antibacterial properties of nitric oxide-releasing sol-gels', *Journal of Biomedical Materials Research Part A: An Official Journal of The Society for Biomaterials, The Japanese Society for Biomaterials, and The Australian Society for Biomaterials and the Korean Society for Biomaterials*. Wiley Online Library, 67(4), pp. 1276–1283.
- Nicholson, J. C. *et al.* (2016) 'Dry sintered metal coating of halloysite nanotubes', *Applied Sciences*. Multidisciplinary Digital Publishing Institute, 6(9), p. 265.

- Norris, P. *et al.* (2005) 'Ultrasonically controlled release of ciprofloxacin from self-assembled coatings on poly (2-hydroxyethyl methacrylate) hydrogels for *Pseudomonas aeruginosa* biofilm prevention', *Antimicrobial agents and chemotherapy*. Am Soc Microbiol, 49(10), pp. 4272–4279.
- Nowatzki, P. J. *et al.* (2012) 'Salicylic acid-releasing polyurethane acrylate polymers as anti-biofilm urological catheter coatings', *Acta biomaterialia*. Elsevier, 8(5), pp. 1869–1880.
- O'toole, G. A. (2002) 'Microbiology: a resistance switch', *Nature*. Nature Publishing Group, 416(6882), p. 695.
- O'Toole, G. A. (2011) 'Microtiter dish biofilm formation assay', *JoVE (Journal of Visualized Experiments)*, (47), p. e2437.
- Palanisamy, N. K. *et al.* (2014) 'Antibiofilm properties of chemically synthesized silver nanoparticles found against *Pseudomonas aeruginosa*', *Journal of nanobiotechnology*. BioMed Central, 12(1), p. 2.
- Pang, X. and Zhitomirsky, I. (2007) 'Electrophoretic deposition of composite hydroxyapatite-chitosan coatings', *Materials Characterization*. Elsevier, 58(4), pp. 339–348. doi: 10.1016/J.MATCHAR.2006.05.011.
- Paschalis, E. I. *et al.* (2013) 'In vitro and in vivo assessment of titanium surface modification for coloring the backplate of the Boston keratoprosthesis', *Investigative ophthalmology & visual science*. The Association for Research in Vision and Ophthalmology, 54(6), pp. 3863–3873.
- Patel, S. *et al.* (2016) 'Sustained release of antibacterial agents from doped halloysite nanotubes', *Bioengineering*. Multidisciplinary Digital Publishing Institute, 3(1), p. 1.
- Pierchala, M. K. *et al.* (2018) 'Nanotubes in nanofibers: Antibacterial multilayered polylactic acid/halloysite/gentamicin membranes for bone regeneration application', *Applied Clay Science*. Elsevier, 160, pp. 95–105.
- Pishbin, F. *et al.* (2013) 'Single-step electrochemical deposition of antimicrobial orthopaedic coatings based on a bioactive glass/chitosan/nano-silver composite system', *Acta biomaterialia*. Elsevier, 9(7), pp. 7469–7479.
- Prabhu, S. and Poulouse, E. K. (2012) 'Silver nanoparticles: mechanism of antimicrobial action, synthesis, medical applications, and toxicity effects', *International nano letters*. Springer, 2(1), p. 32.
- Prasad, K. *et al.* (2017) 'Metallic Biomaterials: Current Challenges and Opportunities', *Materials*. Multidisciplinary Digital Publishing Institute, 10(8), p. 884. doi: 10.3390/ma10080884.

- Radda'a, N. S. *et al.* (2017) 'Electrophoretic deposition of tetracycline hydrochloride loaded halloysite nanotubes chitosan/bioactive glass composite coatings for orthopedic implants'. doi: 10.1016/j.surfcoat.2017.07.048.
- Rapacz-Kmita, A. *et al.* (2015) 'Instrumental characterization of the smectite clay-gentamicin hybrids', *Bulletin of Materials Science*. Springer, 38(4), pp. 1069–1078.
- Ray, P. C., Yu, H. and Fu, P. P. (2009) 'Toxicity and environmental risks of nanomaterials: challenges and future needs', *Journal of Environmental Science and Health Part C*. Taylor & Francis, 27(1), pp. 1–35.
- Reichardt, C. and Welton, T. (2011) *Solvents and solvent effects in organic chemistry*. John Wiley & Sons.
- Ren, L. *et al.* (2014) 'Antibacterial properties of Ti-6Al-4V-xCu alloys', *Journal of Materials Science & Technology*. Elsevier, 30(7), pp. 699–705.
- Ribeiro, M., Monteiro, F. J. and Ferraz, M. P. (2012) 'Infection of orthopedic implants with emphasis on bacterial adhesion process and techniques used in studying bacterial-material interactions', *Biomatter*. Taylor & Francis, 2(4), pp. 176–194.
- Rochford, E. T. J., Richards, R. G. and Moriarty, T. F. (2012) 'Influence of material on the development of device-associated infections', *Clinical Microbiology and Infection*. Elsevier, 18(12), pp. 1162–1167.
- Rodriguez-Sanchez, L., Blanco, M. C. and Lopez-Quintela, M. A. (2000) 'Electrochemical synthesis of silver nanoparticles', *The Journal of Physical Chemistry B*. ACS Publications, 104(41), pp. 9683–9688.
- Salwiczek, M. *et al.* (2014) 'Emerging rules for effective antimicrobial coatings', *Trends in Biotechnology*. Elsevier, 32(2), pp. 82–90.
- Sambhy, V. *et al.* (2006) 'Silver bromide nanoparticle/polymer composites: dual action tunable antimicrobial materials', *Journal of the American Chemical Society*. ACS Publications, 128(30), pp. 9798–9808.
- Sanpo, N. *et al.* (2009) 'Antibacterial property of cold sprayed chitosan-Cu/Al coating', *Journal of thermal spray technology*. Springer, 18(4), p. 600.
- Sarkar, P. and Nicholson, P. S. (1996) 'Electrophoretic deposition (EPD): mechanisms, kinetics, and application to ceramics', *Journal of the American Ceramic Society*. Wiley Online Library, 79(8), pp. 1987–2002.
- Schneider, C. A., Rasband, W. S. and Eliceiri, K. W. (2012) 'NIH Image to ImageJ: 25 years of image analysis', *Nature methods*. Nature Publishing Group, 9(7), p. 671.

Schummer, J. and Baird, D. (2006) *Nanotechnology challenges : implications for philosophy, ethics, and society*. World Scientific. (Accessed: 7 June 2019).

Scott, R. D. (2009) 'The direct medical costs of healthcare-associated infections in US hospitals and the benefits of prevention'.

Secinti, K. D. *et al.* (2011) 'Nanoparticle silver ion coatings inhibit biofilm formation on titanium implants', *Journal of Clinical Neuroscience*. Elsevier, 18(3), pp. 391–395.

Seil, J. T. and Webster, T. J. (2012) 'Antimicrobial applications of nanotechnology: methods and literature', *International journal of nanomedicine*. Dove Press, 7, p. 2767.

Shu, Z. *et al.* (2017) 'Halloysite nanotubes supported Ag and ZnO nanoparticles with synergistically enhanced antibacterial activity', *Nanoscale research letters*. Springer, 12(1), p. 135.

Sidambe, A. (2014) 'Biocompatibility of advanced manufactured titanium implants—A review', *Materials*. Multidisciplinary Digital Publishing Institute, 7(12), pp. 8168–8188.

De Silva, R. T. *et al.* (2015) 'ZnO deposited/encapsulated halloysite–poly (lactic acid)(PLA) nanocomposites for high performance packaging films with improved mechanical and antimicrobial properties', *Applied clay science*. Elsevier, 111, pp. 10–20.

Silva, S. *et al.* (2009) 'Biofilms of non-Candida albicans Candida species: quantification, structure and matrix composition', *Sabouraudia*. International Society for Human and Animal Mycology, 47(7), pp. 681–689.

Sowa-Söhle, E. N. *et al.* (2013) 'Antimicrobial efficacy, cytotoxicity, and ion release of mixed metal (Ag, Cu, Zn, Mg) nanoparticle polymer composite implant material', *BioNanoMaterials*. De Gruyter, 14(3–4), pp. 217–227.

Tappa, K. *et al.* (2017) 'Medication eluting devices for the field of OBGYN (MEDOBGYN): 3D printed biodegradable hormone eluting constructs, a proof of concept study', *PloS one*. Public Library of Science, 12(8), p. e0182929.

Tappa, K. *et al.* (2019) '3D printing custom bioactive and absorbable surgical screws, pins, and bone plates for localized drug delivery', *Journal of functional biomaterials*. Multidisciplinary Digital Publishing Institute, 10(2), p. 17.

Tas, B. A. *et al.* (2019) 'Carvacrol loaded halloysite coatings for antimicrobial food packaging applications', *Food Packaging and Shelf Life*. Elsevier, 20, p. 100300.

Tham, C. Y. *et al.* (2014) *Surface engineered poly (lactic acid)(PLA) microspheres by chemical treatment for drug delivery system*. Trans Tech Publ.

- Tonetti, M. S. and Schmid, J. (1994) 'Pathogenesis of implant failures', *Periodontology 2000*. Wiley Online Library, 4(1), pp. 127–138.
- Tripathi, S., Mehrotra, G. K. and Dutta, P. K. (2011) 'Chitosan–silver oxide nanocomposite film: Preparation and antimicrobial activity', *Bulletin of Materials Science*. Springer, 34(1), pp. 29–35.
- Turner, R. J. (2017) 'Metal-based antimicrobial strategies', *Microbial biotechnology*. Wiley Online Library, 10(5), pp. 1062–1065.
- Vergaro, V. *et al.* (2010) 'Cytocompatibility and uptake of halloysite clay nanotubes', *Biomacromolecules*. ACS Publications, 11(3), pp. 820–826.
- Vinokurov, V. A. *et al.* (2017) 'Formation of metal clusters in halloysite clay nanotubes', *Science and Technology of advanced MaTerialS*. Taylor & Francis, 18(1), pp. 147–151.
- Wang, Z., Xing, M. and Ojo, O. (2014) 'Mussel-inspired ultrathin film on oxidized Ti–6Al–4V surface for enhanced BMSC activities and antibacterial capability', *RSC Advances*. Royal Society of Chemistry, 4(99), pp. 55790–55799.
- Wani, A. L. *et al.* (2017) 'Zinc: An element of extensive medical importance', *Current Medicine Research and Practice*. Elsevier, 7(3), pp. 90–98.
- Wei, W. *et al.* (2012) 'Clay nanotube/poly (methyl methacrylate) bone cement composites with sustained antibiotic release', *Macromolecular materials and engineering*. Wiley Online Library, 297(7), pp. 645–653.
- Wei, W. *et al.* (2013) 'Antibiotic-loaded clay nanotubes for long acting controlled release antimicrobial preparations', in *abstracts of papers of the american chemical society*. amer chemical soc 1155 16TH ST, NW, WASHINGTON, DC 20036 USA.
- Wei, W. *et al.* (2014) 'Enhanced efficiency of antiseptics with sustained release from clay nanotubes', *RSC Advances*. Royal Society of Chemistry, 4(1), pp. 488–494.
- Weisman, J. A. *et al.* (2015) 'Antibiotic and chemotherapeutic enhanced three-dimensional printer filaments and constructs for biomedical applications', *International journal of nanomedicine*. Dove Press, 10, p. 357.
- Weisman, J. A. *et al.* (2017) 'Doped halloysite nanotubes for use in the 3D printing of medical devices', *Bioengineering*. Multidisciplinary Digital Publishing Institute, 4(4), p. 96.
- Weisman, J. A. *et al.* (2019) '3D printed antibiotic and chemotherapeutic eluting catheters for potential use in interventional radiology: in vitro proof of concept study', *Academic radiology*. Elsevier, 26(2), pp. 270–274.

- Wu, F. *et al.* (2019) 'Halloysite nanotubes coated 3D printed PLA pattern for guiding human mesenchymal stem cells (hMSCs) orientation', *Chemical Engineering Journal*. Elsevier, 359, pp. 672–683.
- Xie, Y. *et al.* (2011) 'Magnetic halloysite nanotubes/iron oxide composites for the adsorption of dyes', *Chemical Engineering Journal*. Elsevier, 168(2), pp. 959–963.
- Yeh, C.-H. *et al.* (2015) 'Poly (dopamine)-assisted immobilization of Xu Duan on 3D printed poly (lactic acid) scaffolds to up-regulate osteogenic and angiogenic markers of bone marrow stem cells', *Materials*. Multidisciplinary Digital Publishing Institute, 8(7), pp. 4299–4315.
- Yu, L. *et al.* (2014) 'Enhanced antibacterial activity of silver nanoparticles/halloysite nanotubes/graphene nanocomposites with sandwich-like structure', *Scientific reports*. Nature Publishing Group, 4, p. 4551.
- Yu, Y. *et al.* (2017) 'Multifunctions of dual Zn/Mg ion co-implanted titanium on osteogenesis, angiogenesis and bacteria inhibition for dental implants', *Acta biomaterialia*. Elsevier, 49, pp. 590–603.
- Zhang, J. *et al.* (2012) 'Preparation and characterization of novel polyethersulfone hybrid ultrafiltration membranes bending with modified halloysite nanotubes loaded with silver nanoparticles', *Industrial & engineering chemistry research*. ACS Publications, 51(7), pp. 3081–3090.
- Zhang, X. *et al.* (2015) 'Poly (l-lactide)/halloysite nanotube electrospun mats as dual-drug delivery systems and their therapeutic efficacy in infected full-thickness burns', *Journal of biomaterials applications*. SAGE Publications Sage UK: London, England, 30(5), pp. 512–525.
- Zhang, Yi *et al.* (2013) 'Palladium nanoparticles deposited on silanized halloysite nanotubes: synthesis, characterization and enhanced catalytic property', *Scientific reports*. Nature Publishing Group, 3, p. 2948.
- Zhang, Yatao *et al.* (2013) 'Potent antibacterial activity of a novel silver nanoparticle-halloysite nanotube nanocomposite powder', *Journal of inorganic biochemistry*. Elsevier, 118, pp. 59–64.
- Zhang, Y. *et al.* (2016) 'Applications and interfaces of halloysite nanocomposites', *Applied Clay Science*. Elsevier, 119, pp. 8–17.
- Zhang, Y., Ouyang, J. and Yang, H. (2014) 'Metal oxide nanoparticles deposited onto carbon-coated halloysite nanotubes', *Applied Clay Science*. Elsevier, 95, pp. 252–259.
- Zhang, Y. and Yang, H. (2012) 'Co₃O₄ nanoparticles on the surface of halloysite nanotubes', *Physics and chemistry of minerals*. Springer, 39(10), pp. 789–795.

Zhao, M. and Liu, P. (2008) 'Adsorption behavior of methylene blue on halloysite nanotubes', *Microporous and Mesoporous Materials*. Elsevier, 112(1–3), pp. 419–424.

Zhitomirsky, I. and GAL-OR, L. (1997) 'Electrophoretic deposition of hydroxyapatite', *Journal of Materials Science Materials in Medicine*. Kluwer Academic Publishers, 8(4), pp. 213–219. doi: 10.1023/A:1018587623231.

Zuniga, J. *et al.* (2015) 'Cyborg beast: a low-cost 3d-printed prosthetic hand for children with upper-limb differences', *BMC research notes*. BioMed Central, 8(1), p. 10.